Quantitative imaging in cardiovascular CT angiography

Tuncay, Volkan

DOI:
10.33612/diss.131061767

Quantitative Imaging in Cardiovascular CT Angiography

Volkan Tuncay

2020

The research described in this thesis was performed at the University of Groningen.

Cover Design: ProefschriftMaken || www.proefschriftmaken.nl
Layout: Volkan Tuncay
Printing: ProefschriftMaken || www.proefschriftmaken.nl

ISBN: 978-94-6380-888-0

university of groningen

Quantitative Imaging in Cardiovascular CT Angiography

PhD thesis

to obtain the degree of PhD at the
University of Groningen
on the authority of the
Rector Magnificus Prof. C. Wijmenga
and in accordance with
the decision by the College of Deans.

This thesis will be defended in public on

Monday 7 September 2020 at 18.00 hours

by

Volkan Tuncay

born on 5 October 1982
in Ankara, Turkey

Supervisors

Prof. M. Oudkerk
Prof. P.M.A. van Ooijen

Assessment Committee

Prof. G.J. Verkerke
Prof. I. Isgum
Prof. H.J. Lamb

Table of Contents

Chapter 1 Introduction to Quantification of Cardiovascular Computed Tomography

Cardiovascular imaging has long played an important role in the clinical diagnosis and prediction of prognosis in patients with suspected or known cardiovascular disease and was traditionally performed using plain film X-ray, cardiac catheterization, nuclear imaging and cardiac ultrasound. [1] In the past decades, cardiovascular computed tomography (CT) has emerged as non-invasive modality to evaluate cardiovascular disease at anatomical as well as functional level.

Rapid technological advances have rendered CT coronary angiography an accurate and reliable imaging modality to assess coronary anatomy, coronary artery disease (CAD) and evaluation of bypass grafts [2]. Multi-detector CT (MDCT) has also shown its ability to provide left ventricular (LV) functional parameters with retrospective ECG-gating because of increased temporal resolution. In addition, CT techniques to assess myocardial perfusion and valve function are also gaining ground.

As a result of these fast developments in scanners and scanning techniques, the amount of data acquired using CT is high and still increasing. Therefore, to allow adequate evaluation of these datasets, post-processing using advanced visualization tools is required. These tools range from different types of visualization to semi-automatic and automatic segmentation of structures of interest. However, there is a wide variety in tools available and it can therefore be difficult to determine the right post-processing tools for the task at hand. Furthermore, the interpretation of the results of post-processing, especially when using (semi-)automatic tools, should be handled with care. In short, different post-processing procedures should be used for the different clinical questions that are the indication for cardiac examination using CT.

Common visualization techniques are orthogonal review, curved Multi Planar Reformation (MPR), sliding-thin-slice Maximum Intensity Projection (sts-MIP), and Volume Rendering (VR) which are mostly used in various combinations and are supplemented by advanced tools for (semi-) automatic segmentation and measurement.

A cardiac dataset consists of multiple, successive axial slices, which together form a volume. MPRs can be reconstructed from this dataset and can show the scanned structures in a different plane, other than the acquired axial plane, like coronal, sagittal or oblique planes. For example, most dedicated cardiac CT software packages display a cardiac CT dataset automatically in axial, sagittal and coronal view,

often complemented by a three-dimensional (3D) view. By turning the projection lines manually, an oblique or double oblique MPR can be obtained.

MIP is a specific type of visualization in which only the voxels with the highest intensities are projected into a 2D image [3]. In case of the sts-MIP a small slab is extracted from the datasets, in most cases based on a plane defined using MPR, to apply the MIP algorithm to.

The volume rendering technique transforms the acquired volume data into 3D projection images [3]. Volume rendering provides 'real' depth cues and allows the user to assign properties such as color, transparency, reflection, etc. to each possible voxel value. Although 3D volume rendering was quite time-consuming in earlier years, nowadays software tools provide automatic 3D images when a complete cardiac CT dataset is loaded within seconds. Moreover, most software packages are capable of automatically segmenting the heart from the surrounding structures.

Volume rendering has been the most commonly used 3D reconstruction technique in the clinical practice. However recently a novel rendering 3D rendering technique called Cinematic Rendering has been introduced [4]. This technique follows the same steps to determine the color and opacity as volume rendering does. The difference is that instead of ray-casting that volume rendering is based on cinematic rendering is based on path-tracing methods and the global illumination model. The algorithm simulates different paths of photons coming from different directions through a volumetric dataset and their interaction with the volume to create one pixel. The technique models real life like propagation of the light to create realistic 3D images based on the medical image data [5-6].

Thanks to the developments in 3D reconstruction and the segmentation techniques, CT becomes an important imaging modality in the diagnosis and treatment of the cardiovascular diseases. CAD and valvular diseases are two of the major cardiovascular disease groups that benefit from these developments. In the scope of this thesis, original researches and the literature reviews related to diagnosis and treatment of these cardiovascular disease groups are presented. In the following paragraphs, you will find further information of using CT in the therapeutic management of coronary artery disease and aortic stenosis, the most common valvular disease.

Use of Cardiovascular Computed Tomography in Therapeutic management of Coronary Artery Disease

Worldwide, coronary artery disease is the leading cause of death, with yearly over 17 million deaths [1,7]. Currently, the evaluation of CAD is mainly the field of CT. To evaluate coronary artery disease, two approaches can be followed. The first approach is the evaluation of the coronary lumen, for stenosis measurement. The second approach is the evaluation of the coronary wall, for either coronary calcification quantification or plaque morphology analysis. These two different approaches have their own requirements on the post-processing used.

Coronary Stenosis Measurement

Currently, the automatic segmentation of the coronary artery tree resulting in a display composed of curved multiplanar reformations along the centerline of the coronary arteries and orthogonal cross-sections is commonplace [8] and clinical implementation of advanced visualization is included in current guidelines [9]. Reporting high sensitivity (89%) and specificity (100%), Busch et al [10] concluded that software supported CT-QCA enables automatic quantitative analysis of significant coronary artery stenoses with area stenosis greater than 75%. In many cases, the software will also identify the correct annotation of the coronary artery tree and will label the RCA, LCA and LCX branches automatically provided that the patient has a normal configuration of the coronary artery tree. Maurer et al [11] showed in a survey that the vast majority of hospitals performing cardiac imaging using CT use these automatically generated curved MPRs for their interpretation.

However, reliability of the results of these automatically generated curved MPRs heavily depends on the algorithm used to extract the centerline of the artery and the amount of user interaction required for the segmentation [12]. Furthermore, Dikkers et al [13] showed in a phantom study that manual stenosis measurements are significantly more accurate than automatic measurements, indicating that manual adjustments are still essential for the non-invasive assessment of coronary artery stenosis. A more general approach promoted by other authors is to use axial MDCT images in combination with the (automatic generated) multiplanar reconstructions [14]. Ferencik et al [15] tested various image processing methods to determine hemodynamically significant stenoses of the coronary arteries and found various accuracy levels ranging from 73% to 91%. Based on their results, they stated that the evaluation of multidetector CT coronary angiography with interactive image display methods, especially

interactive oblique MPRs, permits higher diagnostic accuracy than evaluation of pre-rendered images (curved MPR, curved MIP, or VRT images).

The use of multiple techniques in addition to the axial slices in an interactive fashion is supported by the majority of reported studies. The evaluation of multidetector CT coronary angiograms for the detection of coronary stenosis is frequently reported to be performed interactively on off-line workstations, by using a combination of transverse, MPR, MIP, and 3D VRT images [14,16-23]. Some authors evaluated multidetector CT data sets initially by using MIP images or a pre-rendered slab of MPR images, and the findings were then confirmed by using MPR, curved MPR, or 3D VRT images [24-26].

Regardless of the visualization technique used, careful steps must be taken to avoid the effect of motion artifacts, as they can lead to false stenoses [27] (Figure 1). By retrospectively checking any plane parallel to the z-axis motion artifacts can be detected.

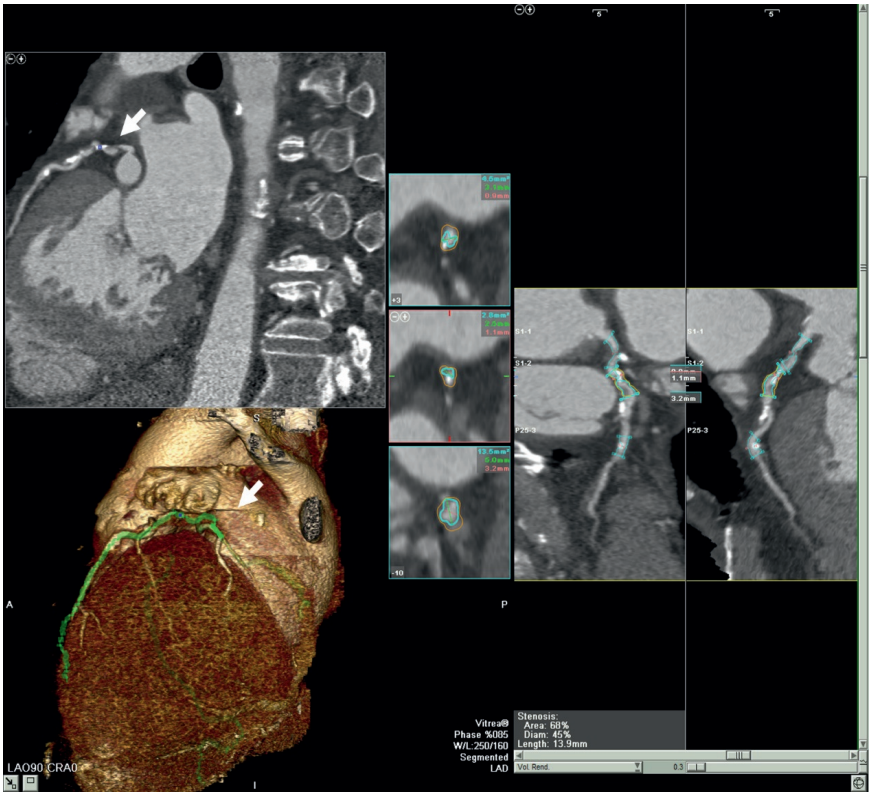

Figure 1: Example where a (significant) stenosis occured at the same z-location as motion artefacts (white arrows). Careful steps must be taken in interpreting the validity of the finding.

Coronary Calcification

The amount of coronary calcification is considered to be a strong predictor of coronary events. [28]. European guidelines consider CT based coronary artery calcium score as class 2b "may be considered" level of evidence. The calcium score is considered as an indicator of the CAD [29].

Assessment of coronary calcification is performed on non-contrast-enhanced CT scans usually with a relatively large slice thickness of 3mm. From the standard axial views of the heart, with high density structures which exceed certain threshold already marked by the software, coronary calcification can be manually selected and assigned to a vessel. The most commonly used threshold for the determination of coronary calcification is 130 Hounsfield Unit (HU) [30].

Subsequently, the selected calcifications are automatically quantified based on the generally accepted scoring methods (Agatston, Volume or MASS).

However, the practical use of calcium scoring in serial studies for tracking the progression of disease is still hampered by the limited reproducibility of the calcium scores currently in use both because of technical [31] and software issues [32]. A study by Groen et al, proposed a way to reduce the susceptibility of calcium scoring to cardiac motion by adjusting the calcification threshold according to its maximum HU value, promoting an increase of accuracy of at least 10%. [33].

Analysis of Plaque Morphology.

It is reported that, to analyze plaque morphology, multiplanar reconstructions orthogonal to the centerline of the (automatically segmented) coronary artery can be obtained resulting in a large number of cross-sections of the coronary artery for evaluation of stenotic and nonstenotic coronary atherosclerotic lesions [34]. The conventional way of analyzing plaque morphology is by manual visual evaluation. To assess maximum luminal narrowing, the optimal image display setting can be chosen on an individual basis, in general at a window between 600 and 900 HU and at a level between 40 and 250 HU. Structures with densities above the adjacent vessel lumen are usually defined as calcified, and structures with densities below the vessel contrast as non-calcified plaques [35-36]. Manual segmentation of outer vessel wall can also be done for assessment of vessel re-modeling, as this parameter plays important role in determining plaque vulnerability [37]. The plaque composition can be determined by the mean HU value of manually placed regions of interest (ROI) at different areas inside

the vessel wall. Of these ROIs, the mean HU value and standard deviation are then used to determine the plaque composition.

Currently, many software packages also provide an automatic determination of lumen and vessel borders in combination with color coding of certain ranges of HU values (Figure 2). These ranges should then indicate the different types of plaque and result in an automatic determination of the volumetric measurement of each plaque type. Therefore, using this automated tool, a complete volumetric analysis of the plaque compositions and of the percentage vessel re-modeling (remodeling index) can be obtained.

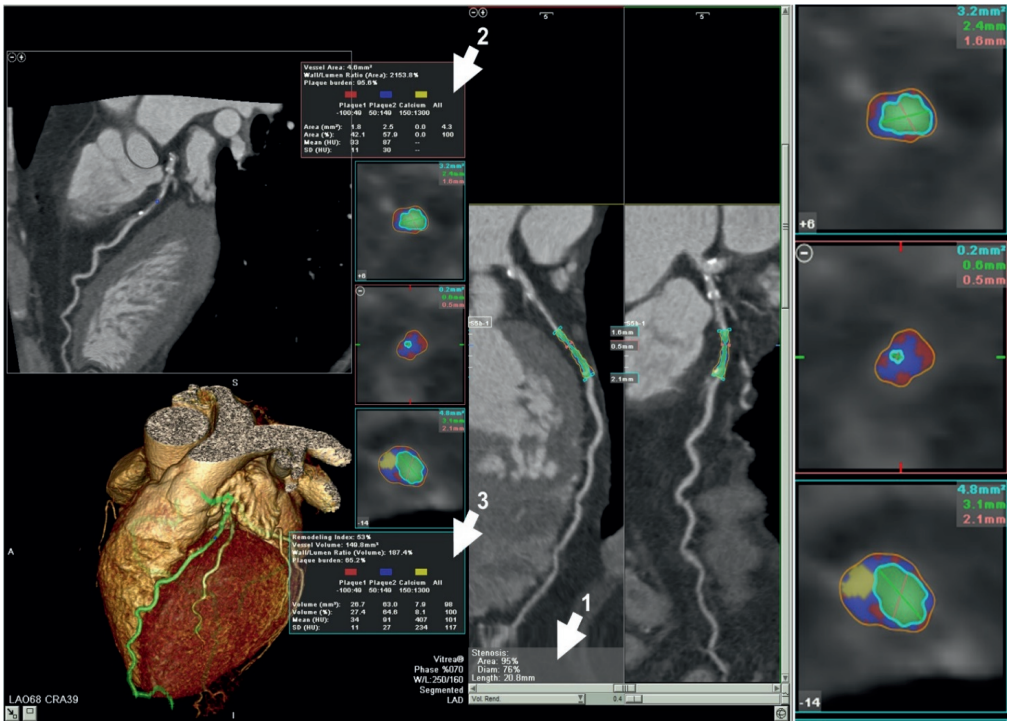

Figure 2: Automatic plaque morphology assessment. Box pointed by arrow 1 show the area and diameter stenosis grade at the most stenotic site, while boxes pointed by arrow 2 and 3 show plaque morphology at the most stenotic plaque cross-section and for the whole plaque volume, respectively.

However, careful selection of the HU ranges should be made as various claims are made by different authors about the HU values that correspond to certain types of plaques using intravascular ultrasound as

the gold standard [36,38-39]. For example, Leber et al [39] reported MDCT-derived density measurements within coronary lesions of 49HU+/-22 for hypoechoic, 91 HU+/-22 for hyperechoic and 391 HU+/-156 for calcified plaques, while Carrascosa et al [40] reported 71.5HU+/-32.1 for soft and 116.3HU+/-35.7 for fibrous, and 383.63HU+/-186.1 for calcified plaques. They both reported these values to be significantly different.

Based on current reports, classification of coronary plaque into calcified and non-calcified plaque could be feasible, either by qualitative visual assessment, using a common threshold for calcification, or even using automatic vessel segmentation tools [41-42]. However, sub classification between the different non-calcified plaque types, such as lipid and fibrous plaque, seems difficult because of the variety in reported cut-off values and the overlap in HU ranges. Furthermore, various factors, such as the reconstruction kernel and the attenuation level of the contrast enhanced blood in the arteries, have been reported to significantly influence the HU value of plaques used for the determination of plaque composition [43-44].

Use of Cardiovascular Computed Tomography in Therapeutic management of Aortic Stenosis

Cardiac diseases are the most common cause of death in developed countries, and Aortic valve stenosis (AS) is the most common valvular heart disease in the population older than 65 years [45]. In AS the aortic valve becomes narrower which affects the blood flow from the heart into the aorta. Visualization of the aortic valvular area (AVA) is required to obtain preoperative knowledge.

Various non-invasive imaging modalities are available to assess function and morphology of the cardiac valves [46] of which echocardiography is widely used due to low costs and wide availability.

However, due to fast technical developments of CT and Magnetic Resonance Imaging (MRI), these imaging modalities are gaining ground in the evaluation of the cardiac valves [47]. Studies show that the planimetric measurements of AVA by Dual-Source CT (DSCT) are very well correlated with the measurements done by Transthoracic Echocardiography (TTE). Besides DSCT has higher reproducibility compared with TEE [48]. However, CT requires comparatively high radiation dose because a dedicated scan has to be made with retrospective gating and optimal image quality throughout the cardiac cycle. Advantages of MRI compared to CT are lack of radiation exposure and superior temporal resolution. In addition, with MRI no intravenous contrast administration is required because of the excellent contrast between the blood pool and low-signal-intensity myocardial wall and valves. MRI

also provides the ability for quantitative measurements and the possibility to add valvular velocity flow mapping measurements [49]. Valvular function is assessed with SSFP cine MRI [46]. In case of a valve insufficiency or stenosis, a void (jet) can be visually observed due to turbulent flow.

Manghat et al. [49] provide a manual protocol for the optimal CT imaging planes of the heart valves and chambers using MPR and multiphasic cine movie loops based on the standard echocardiographic imaging planes. With contrast enhanced MDCT, the number of leaflets, opening and closing of the leaflets and presence of calcification can be visualized (Figure 3) [46]. Unenhanced MDCT is preferred over contrast-enhanced images for the quantification of valvular calcification [46, 50].

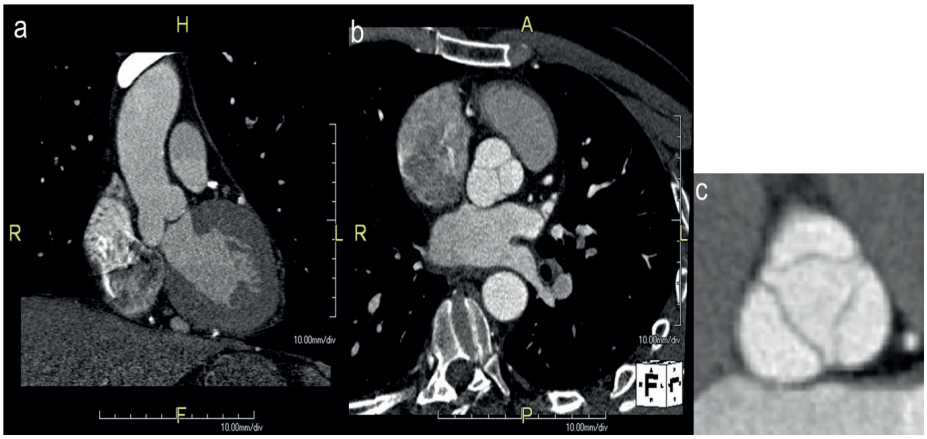

Figure 3: Oblique view of the left ventricle and ascending aorta (a) the aortic valve is completely closed. Three aortic leaflets are visible with normal closure (b).Aortic valvular area (AVA) is determined at maximum opening (c).

Chen et al [51] used ECG-gated CT angiography for the functional assessment of the valves. They visualized both healthy valves and also the valve conditions such as aortic stenosis, mitral stenosis, pulmonary stenosis, and tricuspid stenosis. They concluded that the valve thickness, opening, closing and the calcification can be observed very well by the CT angiography. Thus, CT angiography can provide useful information for the surgery planning.[51]

By construction of intravascular views of CT datasets, three-dimensional volume rendering can also be used for demonstration of the motion of the cardiac valves (Figure 4).

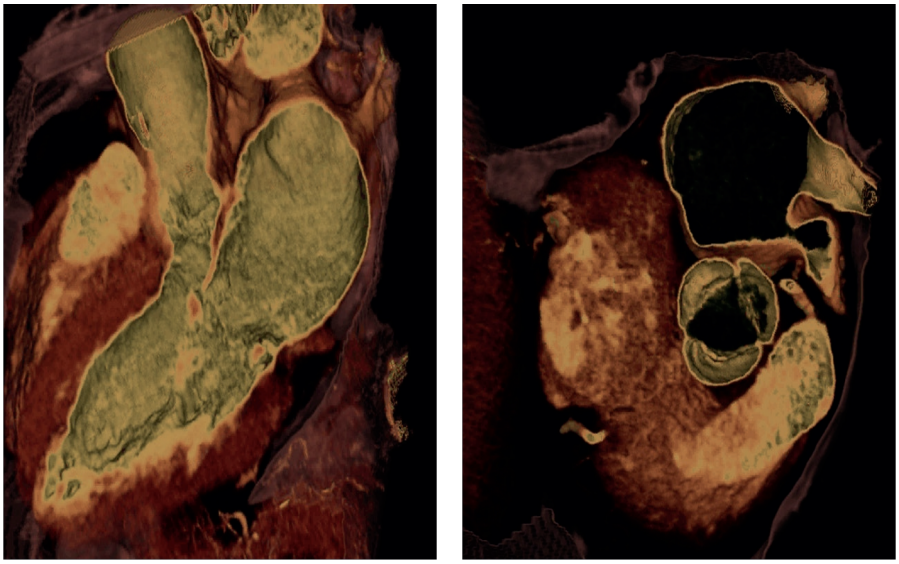

Figure 4: Two frames of four-dimensional movies showing an intra-vascular view of the cardiac valves.

Surgical aortic valve replacement is the traditional way of treating severe aortic stenosis. However, this type of open-heart surgery is too risky for some patients. Minimally invasive Transcatheter Aortic Valve Implantation (TAVI) has become an option for these patients. CT plays a major role in TAVI planning by providing information about the aortic annulus dimensions to determine the correct prosthesis size [52]. Choosing the appropriate size of prosthesis for the intervention is one of the most crucial part of the surgical planning of TAVI as annulus - prosthesis mismatch may lead to serious injury or death [53].

Conclusion

In conclusion, cardiovascular diseases are the leading cause of death. CAD and the structural heart diseases are the two major cardiovascular disease groups. 3D reconstructions of CT images proved themselves useful in supplying crucial spatial information to medical professionals. Biomarkers such as CT based calcium scoring and treatment techniques such as TAVI makes CT the main imaging modality that can provide solutions both in diagnosis and surgical planning of cardiovascular diseases.

References

1. Hurlock GS, Higashino H, Mochizuki T. History of cardiac computed tomography: single to 320-detector row multislice computed tomography. Int J Cardiovasc Imaging 2009;25:31-42.

2. Leschka S, Stolzman P, Alkadhi H. Recent developments in coronary computed tomography imaging. Imaging Med 2009;1(1):103-114

3. Fishman EK, Ney DR, Heath DG et al. Volume rendering versus maximum intensity projection in CT angiography: what works best, when and why. Radiographics 2006;26:905-922 ** Good introduction on volume rendering and maximum intensity projection

4. Eid M, De Cecco CN, Nance JW, Jr. et al (2017) Cinematic Rendering in CT: A Novel, Lifelike 3D Visualization Technique. AJR Am J Roentgenol 209:370-379

5. Dappa E, Higashigaito K, Fornaro J, Leschka S, Wildermuth S, Alkadhi H (2016) Cinematic rendering - an alternative to volume rendering for 3D computed tomography imaging. Insights Imaging 7:849-856

6. Ebert LC, Schweitzer W, Gascho D et al (2017) Forensic 3D Visualization of CT Data Using Cinematic Volume Rendering: A Preliminary Study. AJR Am J Roentgenol 208:233-240

7. Mackay J, Mensah G. Atlas of heart disease and stroke. WHO press, Geneva 2004.

8. Dewey M, Schnapauff D, Laule M, Lembcke A, Borges AC, Rutsch W, Hamm B, Rogalla P. Multislice CT Coronary Angiography: Evaluation of an Automatic Vessel Detection Tool. Fortschr Rontgenstr 2004;176:478-483. ** Evaluation paper on the performance of automatic segmentation.

9. Mark DB, Berman DS, Budoff MJ, Carr JJ, Gerber TC, Hecht HS, Hlatky MA, Hodgson JMcB, Lauer MS, Miller JM, Morin RL, Mukherjee D, Poon M, Rubin GD, Schwartz RS. ACCF/ACR/AHA/NASCI/SAIP/SCAI/SCCT 2010 Expert Consensus Document on Coronary Computed Tomography Angiography: A Report of the American College of Cardiology Foundation Task Force on Expert Consensus Documents. Circulation 2010;121:2509-2543.

10. Busch S, Johnson TRC, Nikolaou K, von Ziegler F, Knez A, Reiser MF, Becker CR. Visual and Automatic Grading of Coronary Artery Stenoses with 64-slice CT Angiography in Reference to Invasive Angiography. Eur Radiol 2007;17:1445-1451.

11. Maurer MH, Hamm B, Dewey M. Survey regarding the Clinical Practice of Cardiac CT in Germany: Indications, Scanning Technique and Reporting. Fortschr Röntgenstr 2009;181:1135-1143.

12. Schaap M, Metz CT, van Walsum R, van der Giessen AG, Weustink AC, Mollet NR, Bauer C, Bogunovic H, Castro C, Deng X, Dikici E, O'Donnell T, Frenay M, Friman O, Hernandez Hoyos M, Kitslaar PH, Krissian K, Kuhnel C, Luengo-Oroz MA, Orkisz M, Smedby O, Styner M, Szymczak A, Tek H, Wang C, Warfield SK, Zambal S, Zhang Y, Krestin GP, Niessen WJ. Standardized evaluation methodology and reference database for evaluating coronary artery centerline extraction algorithms. Medical Image Analysis 2009;13:701-714. ** Extensive work on the systematic evaluation of algorithms used for coronary artery segmentation in comparison with manual expert segmentations.

13. Dikkers R, Willems TP, de Jonge GJ, Marquering HA, Greuter MJW, van Ooijen PMA, JAnsen van der Weide MC, Oudkerk M. Accuracy of Noninvasive Coronary Stenosis Quantification of Different Commercially Available Dedicated Software Packages. J Comput Assist Tomogr 2009;33:505-512. ** Important paper on the evaluation of commercial software for coronary stenosis quantification.

14. Ropers D, Baum U, Pohle K, Anders K, Ulzheimer S, Ohnesorge B, Schlundt C, Bautz W, Daniel WG, Achenbach S. Detection of Coronary Artery Stenosis with Thin-Slice Multi-Detector Row Spiral Computed Tomography and Multiplanar Reconstruction. Circulation 2003;107:664-666.

15. Ferencik M, Ropers D, Abbara S, Cury RC, Hoffmann U, Nieman K, Brady TJ, Moselewski F, Daniel WG, Achenbach S. Diagnostic Accuracy of Image Postprocessing Methods for the Detection of Coronary Artery Stenoses by Using Multidetector CT. Radiology 2007;243(3):696-702 ** Evaluation paper on the performance of visualization and postprocessing techniques

16. Nieman K, Cademartiri F, Lemos PA, Raaijmakers R, Pattynama PM, de Feyter PJ. Reliable noninvasive coronary angiography with fast submillimeter multislice spiral computed tomography. Circulation 2002;106:2051–2054

17. Hoffmann U, Moselewski F, Cury RC, et al. Predictive value of 16-section multidetector spiral computed tomography to detect significant obstructive coronary artery disease in patients at high risk for coronary artery disease: patient- versus segment-based analysis. Circulation 2004;110:2638–2643

18. Martuscelli E, Romagnoli A, D'Eliseo A, et al. Accuracy of thin-section computed tomography in the detection of coronary stenoses. Eur Heart J 2004;25:1043–1048

19. Kuettner A, Beck T, Drosch T, et al. Diagnostic accuracy of noninvasive coronary imaging using 16-detector slice spiral computed tomography with 188 ms temporal resolution. J Am Coll Cardiol 2005;45:123–127

20. Leschka S, Alkadhi H, Plass A, et al. Accuracy of MSCT coronary angiography with 64-section technology: first experience. Eur Heart J 2005;26:1482–1487.

21. Leber AW, Knez A, von Ziegler F, et al. Quantification of obstructive and nonobstructive coronary lesions by 64-section computed tomography: a comparative study with quantitative coronary angiography and intravascular ultrasound.J Am Coll Cardiol 2005;46:147–154

22. Raff GL, Gallagher MJ, O'Neill WW, Goldsten JA. Diagnostic accuracy of noninvasive coronary angiography using 64-section spiral computed tomography. J Am Coll Cardiol 2005;46:552–557.

23. Dewey M, Laule M, Krug L, et al. Multisegment and halfscan reconstruction of 16-section computed tomography for detection of coronary artery stenoses. Invest Radiol 2004;39:223–229.

24 Mollet NR, Cademartiri F, Krestin GP, et al. Improved diagnostic accuracy with 16-row multi-section computed tomography coronary angiography. J Am Coll Cardiol 2005;45:128–132.

25. Hoffmann MH, Shi H, Schmitz BL, et al. Noninvasive coronary angiography with multislice computed tomography. JAMA 2005;293:2471–2478.

26. Kefer J, Coche E, Legros G, et al. Head-tohead comparison of three-dimensional navigator-gated magnetic resonance imaging and 16-section computed tomography to detect coronary artery stenosis in patients. J Am Coll Cardiol 2005;46:92–100.

27. Kristanto W, van Ooijen PM, Dikkers R, Greuter MJ, Zijlstra F, Oudkerk M. Quantitative image analysis for the detection of motion artefacts in coronary artery computed tomography. Int J Cardiovasc Imaging 2010; 26:77-87.

28. Arad Y, Goodman KJ, Roth M, Newstein D, Guerci AD. Coronary calcification, coronary disease risk factors, C-reactive protein, and atherosclerotic cardiovascular disease events the St. Francis Heart Study. Journal of the American College of Cardiology 2005;46(1):158-65.

29. Piepoli MF, Hoes AW, Agewall S et al (2016) 2016 European Guidelines on cardiovascular disease prevention in clinical practice: The Sixth Joint Task Force of the European Society of Cardiology and Other Societies on Cardiovascular Disease Prevention in Clinical Practice (constituted by representatives of 10 societies and by invited experts)Developed with the special contribution of the European Association for Cardiovascular Prevention & Rehabilitation (EACPR). Eur Heart J 37:2315-2381

30. Agatston AS, Janowitz WR, Hildner FJ, Zusmer NR, Viamonte M, Jr., Detrano R. Quantification of coronary artery calcium using ultrafast computed tomography. J.Am.Coll.Cardiol. 1990 Mar 15;15(4):827-32.

31. Naghavi M, Falk E, Hecht HS, et al. From vulnerable plaque to vulnerable patient-Part III: executive summary of the Screening for Heart Attack Prevention and Education (SHAPE) Task Force Report. Am J Cardiol 2006;98:2–15

32. van Ooijen PM, Vliegenthart R, Witteman JC, Oudkerk M. Influence of Scoring Parameter Settings on Agatston and Volume Scores for Coronary Calcification. Eur Radiol 2005;15(1):102-110.

33. Groen JM, Dijkstra H, Greuter MJW, Oudkerk M. Threshold adjusted calcium scoring using CT is less susceptible to cardiac motion and more accurate. Med Phys 2009;36(2):438-446.

34. Achenbach S, Ropers D, Hoffmann U, MacNeill B, Baum U, Pohle K, et al. Assessment of coronary remodeling in stenotic and nonstenotic coronary atherosclerotic lesions by multidetector spiral computed tomography. J Am Coll Cardiol 2004; 43:842–847.

35. Leber AW, Knez A, White CW, et al. Composition of coronary atherosclerotic plaques in patients with acute myocardial infarction and stable angina pectoris determined by contrast-enhanced multislice computed tomography. Am J Cardiol 2003;91:714–8.

36. Schroeder S, Kopp AF, Baumbach A, Meisner C, Kuettner A, Georg C, et al. Noninvasive detection and evaluation of atherosclerotic coronary plaques with multislice computed tomography. J Am Coll Cardiol 2001;37:1430–1435.

37. Schoenhagen P, Ziada KM, Kapadia SR, Crowe TD, Nissen SE, Tuzcu EM. Extent and Direction of Arterial Remodeling in Stable Versus Unstable Coronary Syndromes: An Intravascular Ultrasound Study. Circulation 2000; 101; 598-603.

38. Cademartiri F, La Grutta L, Palumbo A, Malagutti P, Pugliese F, Meijboom WB, Baks T, Mollet NR, Bruining N, Hamers R, de Feyter PJ. Non-invasive visualization of coronary atherosclerosis: state-of-the-art. Journal of Cardiovascular Medicine 2007;8:129-137.

39. Leber AW, Knez A, Becker A, Becker C, von Ziegler F, Nikolaou K, et al. Accuracy of multidetector spiral computed tomography in identifying and differentiating the composition of coronary atherosclerotic plaques: a comparative study with intracoronary ultrasound. J Am Coll Cardiol 2004; 43:1241–1247.

40. Carrascosa PM, Capu±ay CM, Garcia-Merletti P, Carrascosa J, Garcia MJ (2006) Characterization of coronary atherosclerotic plaques by multidetector computed tomography. The American Journal of Cardiology 97:598-602.

41. Achenbach S, Moselewski F, Ropers D, Ferencik M, Hoffmann U, MacNeill B, Pohle K, Baum U, Anders K, Jang I, Daniel WG, Brady TJ. Detection of Calcified and Noncalcified Coronary Atherosclerotic Plaque by Contrast-Enhanced, Submillimeter Multidetector Spiral Computed Tomography: A Segment-Based Comparison With Intravascular Ultrasound. Circulation 2004; 109; 14-17.

42. Clouse ME, Sabir A, Yam C, Yoshimura N, Lin S, Welty F, Martinez-Clark P, Raptopoulos V. Measuring Noncalcified Coronary Atherosclerotic Plaque Using Voxel Analysis with MDCT Angiography: A Pilot Clinical Study. Am J Radiol 2008; 190:1553-1560.

43. Cademartiri F, La Grutta L, Runza G, Palumbo A, Maffei E, Mollet NRA, Bartolotta TV, Somers P, Knaapen M, Verheye S. Influence of convolution filtering on coronary plaque attenuation values: observations in an ex vivo model of multislice computed tomography coronary angiography. Eur Radiol 2007; 17:1842-1849.

44. Cademartiri F, Mollet NR, Runza G, Bruining N, Hamers R, Somers P, et al. Influence of intracoronary attenuation on coronary plaque measurements using multislice computed tomography: observations in an ex vivo model of coronary computed tomography angiography. Eur Radiol 2005; 15:1426–1431** Critical paper on the effect of lumen enhancement on the measurement of coronary plaque based on HU cutoff values.

45. Rosamond W, Flegal K, Furie K, et al. Heart disease and stroke statistics: 2008 update—a report from the American Heart Association Statistics Committeeand Stroke Statistics Subcommittee. Circulation 2008;117:e25–e146.

46. Vogel-Claussen J, Pannu H, Spevak PJ et al. Cardiac valve assessment with MR imaging and 64-section multi-detector row CT. Radiographics 2006;26:1769-1784.

47. Feuchtner GM, The utility of computed tomography in the context of aortic valve disease, The International Journal of Cardiovascular Imaging 2009;25(6):611 -614

48. Li X, Tang L, Zhou L, Duan Y, Yanhui S, Yang R, Wu Y, Kong X (2009) Aortic valves stenosis and regurgitation:assessment with dual source computed tomography. International Journal of Cardiovascular Imaging 2009;25(6):591-600.

49. Manghat NE, Rachapalli V, van Lingen R, Veitch AM, Roobottom CA, Morgan-Hughes GJ. Imaging the heart valves using ECG-gated 64-detector row cardiac CT. The Britisch Journal of Radiology 2008;81:275-290.

50. Muhlenbruch G, Wildberger JE, Koos R et al. Calcium scoring of aortic valve stenosis with a multislice computed tomography scanner: non-enhanced versus contrast-enhanced studies. Acta Radiol 2005;46:561-566

51. Chen JJ, Manning MA ,Frazier AA, Judy J, White CS, CT Angiography of the Cardiac Valves: Normal, Diseased, and Postoperative Appearances, Radiographics 2009;29(5):1393.

52. Kasel, A.M., et al., Standardized imaging for aortic annular sizing: implications for transcatheter valve selection. JACC Cardiovasc Imaging, 2013. 6(2): p. 249-62.

53. Carminati, M., et al., Role of imaging in interventions on structural heart disease. Expert Rev Cardiovasc Ther, 2013. 11(12): p. 1659-76.

Scope of the Thesis

This thesis aimed to explore the role of Computed Tomography in the field of cardiovascular research mainly on coronary artery disease and valvular diseases. The thesis is composed of two parts namely 1) Coronary Morphology and Plaque, 2) Aortic Valve Measurement

Part 1 Coronary Morphology and Plaque

Chapter 2 investigated the association between the coronary artery geometry with presence and extent of coronary artery disease using non-invasive coronary computed tomography angiography. Curvature and tortuosity were measured based on the centerlines of the coronary arteries as the metrics of the coronary artery geometry. Association of these metrics with significant coronary artery stenosis (as >70% luminal narrowing) and presence of plaque assessed in order to investigate this relationship.

Chapter 3 investigated two question. First question is whether the geometry of coronary artery geometry changes between end-systolic and end-diastolic phases. Second question is whether the dynamic change of coronary artery geometry is related with the coronary artery disease. In this study in addition to curvature and tortuosity, inflection points were counted as one of the metrics of coronary artery geometry.

Chapter 4 introduced a technique to correct the influence of lumen contrast enhancement on non-calcified atherosclerotic plaque Hounsfield-Unit values in CT images in order to obtain the correct HU values for the characterization and quantification of non-calcified plaques. This technique is based on a

previously determined exponential decline pattern of HU on the lumen wall caused by the contrast agent.

Part 2 Aortic Valve Measurement

Chapter 5 is a systematic review aimed to review the literature on application of 3D printing to valvular diseases. In this regard, constraints and the possibilities of 3D printing in this field are discussed based on the published literature. Data preparation, time requirements, printer possibilities, and material properties are discussed as the main technical issues. Furthermore, the clinical applications of the 3D printed models of heart valves are investigated in this systematic review.

Chapter 6 is describing the design and validation of a pulsatile pump and a mock circulatory system. The aim of this study is to create a phantom set up that mimics the circulatory system with variable frequency and stroke volume. This phantom setup is planned to be used in validation tests and other development purposes such as image processing and medical device testing.

Chapter 7 presents a semi-automatic segmentation technique to quantify the aortic valve area. The aim of this study is to develop a fast and reliable quantification technique. The developed algorithm is validated with the gold standard echocardiography. Furthermore intra- and inter- reader variabilities, and measurement durations of manual and presented semi-automatic segmentation techniques were compared.

Chapter 8 is the second systematic review presented in this thesis. This systematic review has its question on its title “Does the Aortic Annulus undergo dynamic conformational changes during the cardiac cycle?”. The answer of this question has utmost importance in the surgical planning of the transcatheter aortic valve implantation as the prosthesis selection of these procedures are based on the aortic annulus measurements and mis-sizing can lead to aortic regurgitation or rupture of the aortic root causing potentially death.

Part 1

Coronary Morphology and Plaque

Chapter 2 Non-invasive assessment of coronary artery geometry using coronary CTA

Publication: Non-invasive assessment of coronary artery geometry using coronary CTA

Tuncay V, Vliegenthart R, den Dekker MAM, de Jonge GJ, van Zandwijk JK,van der Harst P, Oudkerk M, van Ooijen PMA.

Journal of Cardiovascular Computed Tomography 2018;12(3):257-260

Conference paper: Tortuosity and Curvature of the Coronary Arteries in Relation with Coronary Artery Disease

V. Tuncay, P. M. Van Ooijen, M. Oudkerk, M. A. den Dekker, R. Vliegenthart, E. R. van den Heuvel.

ECR 2014, http://dx.doi.org/10.1594/ecr2014/C-0288

Introduction

Atherosclerotic plaques evolve over time and can cause narrowing of coronary arteries with subsequently reduced downstream blood flow. Development and progression of plaque is complex and not yet fully understood. One of the mechanical factors affecting the plaque process is shear wall stress [1-3]. In-vivo studies have shown that predominant low shear stress is predominantly present in the inner curvature of the vessel. Atherosclerotic plaque distribution is reported to be associated with the vessel curvature, as well as with vessel bifurcations [1, 4]. The methods used to obtain these data were invasive techniques that can only be applied in symptomatic patients with clinical indication for invasive coronary angiography, resulting in biased samples. However, gaining insight in the relationship between three-dimensional vessel geometry and plaque development could be of great importance to allow early detection of individuals at increased future risk of developing CAD. We investigated the relationship between coronary curvature and tortuosity with presence and extent of CAD using non-invasive coronary computed tomography angiography (cCTA).

Methods

Patients and Cardiac CT protocol

Current study is a sub-study of the GROUND-2 study, which evaluated the presence of silent CAD in cardiac asymptomatic patients with known extra-cardiac arterial disease [5]. The medical ethical committee waived the need for additional approval for this retrospective analysis. From GROUND-2 participants with cCTA data (n=75), only those with reconstructions at end-diastolic phase were included (n=73, 97.3%), to enable comparison of curvature and tortuosity based on the same phase in the cardiac cycle.

CT scans were performed on a dual-source CT scanner (SOMATOM Definition, Siemens, Erlangen, Germany). cCTA was performed in spiral mode, using retrospective electrocardiographic gating, the common approach for cCTA acquisition at time of inclusion.

During the GROUND-2 study, attending radiologists with (cCTA experience from 5 to >10 years) evaluated the cCTA data for presence and severity of CAD [5]. Presence of plaque and stenosis were assessed per segment, according to the 15-segment modified American Heart Association classification [6]. >70% luminal narrowing was interpreted as significant stenosis. Detailed information on the

inclusion, the CT scan / evaluation protocol and the population characteristics can be found in the previous publication [5].

Assessment of Coronary Artery Geometry

Geometry assessment was performed using dedicated software (Aquarius iNtuition Ver.4.4.11, Terarecon, San Mateo, USA). Following automatic ribcage removal, related cardiac workflow steps were selected for detailed inspection of the main coronary arteries (right coronary artery (RCA) (segment 1-3), left main (LM) (5), left anterior descending artery (LAD) (6-9), and left circumflex artery (LCX) (11,13)). The coronary arteries could be selected on the transverse slices or on the volume-rendered reconstruction, resulting in a curved multi-planar reformat reconstruction (cMPR) of the selected vessel with automatic centerline extraction. Curvature and tortuosity measurements were performed based on the centerline of the coronary artery selected in the three-dimensional view (Figure 1). Selected arteries were stretched in the cMPR for determination of the start and end points of the segments (Figure 2). Each segment was marked manually (Figure 2) followed by curvature and tortuosity measurements of the marked region based on the three-dimensional course of the centerline. If needed, centerlines were manually corrected. Measurements were performed for each segment (Figure 2a), and for the entire vessel (Figure 2b). Segments with an average diameter of less than 1.5 mm were excluded, to ensure reproducibility. Initially segments 1-3, 5-9, 11, and 13 were assessed (730 segments). Due to the high exclusion rate (71.2%), segment 9 was excluded.

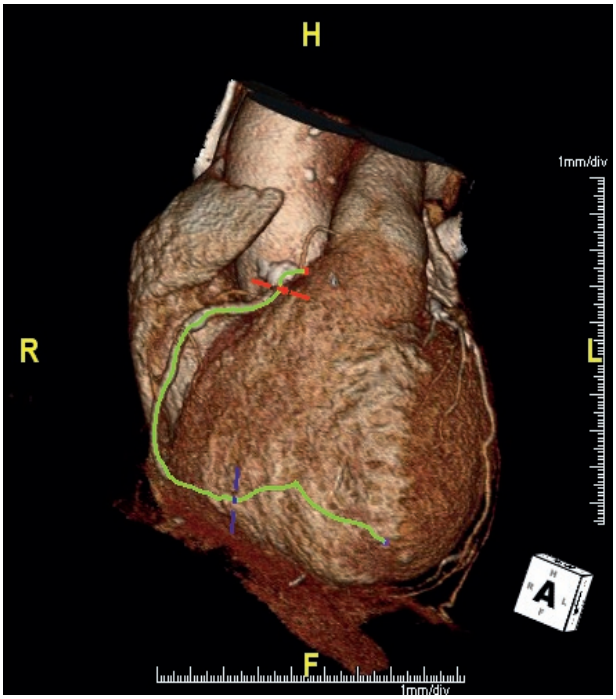

Figure 1: Volume rendered computed tomography image of a segmented right coronary artery.

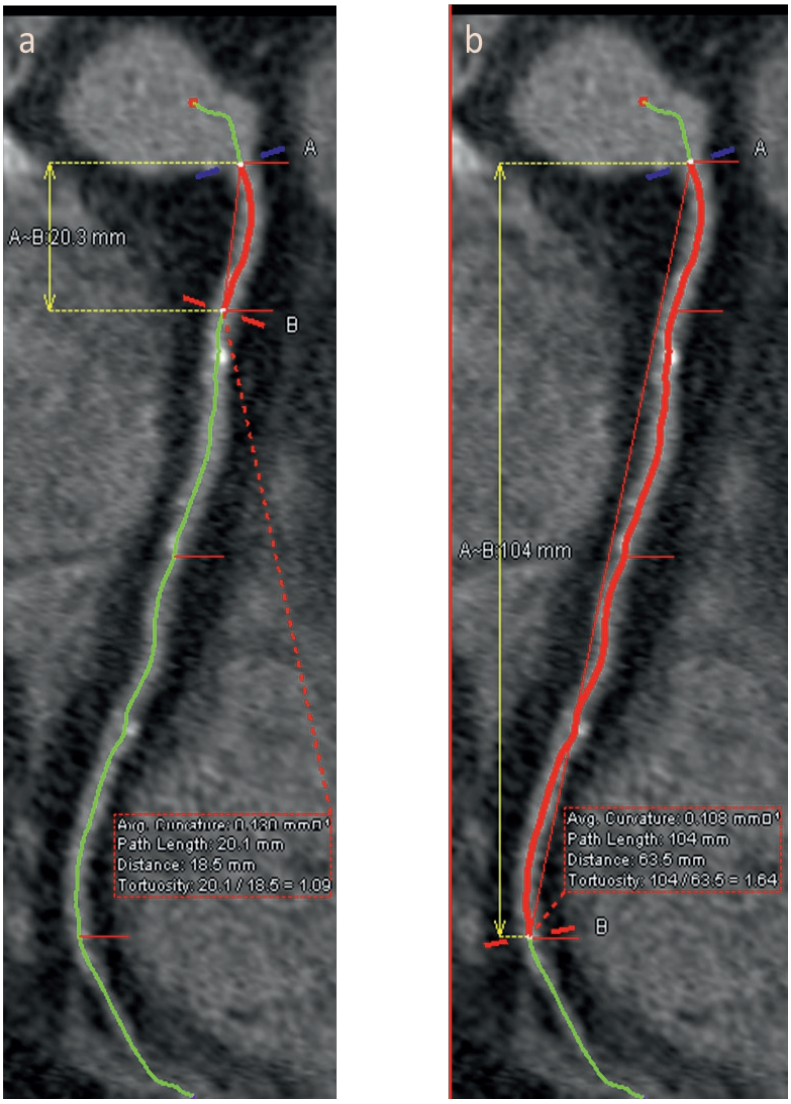

Figure 2: Example of the right coronary artery in curved multiplanar reformat reconstructions. Segments are separated by the red markers. Curvature and tortuosity are measured for (a) segment 1, and (b) whole vessel.

Local curvature was calculated between a selected point, a point 5 mm before and a point 5 mm beyond on the centerline, at every 5 mm using Menger's curvature[7]. The scale of the interval was decided after testing intervals from 1 mm to 20 mm with 1 mm increment, as it is known that smaller scales lead to fluctuation, whereas larger scales become less sensitive to sharp local bends.. Average of the local curvatures on the selected range was given in mm-1 as the result of the curvature measurement.

Tortuosity was defined as the total length of the centerline divided by the straight distance between begin and endpoint of the indicated range on the centerline[8, 9]. Intra-reader agreement for geometry measures was assessed for all scans by having one experienced reader perform all measurements twice at a three-week interval. To assess inter-reader agreement, a second reader independently evaluated 20 randomly selected scans.

Statistical Analysis

Intra-class correlation coefficients (ICC) were calculated to assess the reproducibility [10]. Systematic intra- and inter-reader differences were assessed by Bland-Altman analysis.

To investigate the association between a significant stenosis and curvature or tortuosity, a linear mixed model was applied for curvature and tortuosity separately. The analyses were performed at the segment level and at the artery level (RCA, LM, LAD, and LCX). Association and interaction analyses were corrected for age, sex and hypertension. All statistical tests were two-sided. Statistical analyses were performed using SAS version 9.3 (SAS Institute Inc., Cary, NC, USA) and IBM SPSS Statistics version 20.0.0.1 (SPSS Inc., Chicago, IL, USA).

Results

Study Characteristics

Seventy-three participants (76.3% males, mean age 64.8 ± 8.1 years) with a cCTA dataset reconstructed at end-diastolic phase could be included in this sub-study. Characteristics of the participants are shown in Table 1. The prevalence of cardiovascular risk factors was high. For the total population of the GROUND-2 study the prevalence of significant CAD was 56.8%. Median curvature and tortuosity were respectively 0.094 [0.071; 0.120] and 1.080 [1.040; 1.120] on segment level, and 0.096 [0.078; 0.118] and 1.175 [1.090; 1.420] on artery level.

Table 1: Clinical characteristics of the study population.

	All patients (*N*=73)
Age (years)	64.8 ± 8.1
Male gender (%)	76.7
Body mass index (kg/m^2)	26.2 ± 3.8
Systolic blood pressure (mmHg)	140 ± 24
Diastolic blood pressure (mmHg)	79 ± 9
Hypertension (%)	82.2
Cholesterol (mmol/L)	4.7 ± 1.2
Triglyceride (mmol/L)	2.02 ± 1.8
HDL cholesterol (mmol/L)	1.2 ± 0.4
LDL cholesterol (mmol/L)	2.9 ± 0.9
Dyslipidemia (%)	93.2
Glucose (mmol/L)	5.8 ±1.1
Diabetes mellitus (%)	9.6
Smoking (%)	32.9
Significant stenosis prevalence (%)	46.6
Plaque prevalence (%)	82.2

Continuous variables are expressed as mean ± standard deviation or median (25^{th}, 75^{th} percentile), dichotomous variables are expressed as percentages. HDL: high density lipoprotein; LDL: low density lipoprotein

Reproducibility and Reader Agreement

The overall ICC showed excellent intra-reader agreement (ICC>0.80) for tortuosity and curvature measurements. Inter-reader agreement was found to be good for curvature (ICC=0.73) and excellent for tortuosity (ICC=0.92).

Bland-Altman analysis showed a mean intra-reader difference for curvature and tortuosity of -0.0013 (95% CI:-0.0398, 0.0425) mm-1 and 0.0011 (95 % CI:-0.1755,0.1734), respectively. Mean inter-reader difference for curvature and tortuosity were 0.0036 (95% CI: -0.0513, 0.0585) mm-1 and 0.0236 (95% CI:-0.1606, 0.2078), respectively. Association between Vessel Geometry and Stenosis.

Association between Vessel Geometry and Stenosis

A significant association was observed between curvature and significant stenosis both at segment level ($p<0.001$) and artery level ($p=0.002$) (Table 2). Patients with a significant stenosis had 16.7% and 13.8% higher curvature at segment and artery level, respectively, than patients without stenosis.

Table 2: Association of curvature and tortuosity with significant stenosis, corrected for age, sex, and hypertension.

Measure	Analysis on segment level			Analysis on artery level		
	Estimate	P-value		Estimate	P-value	
		Association	Interaction		Association	Interaction
Curvature	1.167 [1.088;1.251]	<0.001	0.421	1.138 [1.049;1.235]	0.002	0.106
Tortuosity	1.279 [1.097;1.491]	0.002	0.041	1.105 [0.964;1.267]	0.149	0.056

There was an association between tortuosity and significant stenosis at segment level ($p=0.002$). There was interaction for tortuosity at segment level ($p=0.041$), indicating that the relationship between tortuosity and significant stenosis is not the same across segments.

Association between Vessel Geometry and Presence of Plaque

A significant association was observed between curvature and plaque presence at both segment ($p<0.001$) and artery level ($p<0.001$) (Table 3). For instance, segments with a plaque had 17.6% higher curvature than segments without coronary plaque. There was also an association between tortuosity and plaque presence at segment level ($p<0.001$). On average, segments with plaque were 30.8% more tortuous. The interaction of tortuosity and plaque presence indicated the association was not the same across segments ($p=0.013$).

Table 3: Association presence of plaque with curvature and tortuosity corrected for age, sex, and hypertension

Measure	Analysis on segment level			Analysis on artery level		
	Estimate	P-value		Estimate	P-value	
		Association	Interaction		Association	Interaction
Curvature	1.176 [1.106;1.251]	<0.001	0.066	1.161 [1.078;1.250]	<0.001	0.136
Tortuosity	1.308 [1.142;1.498]	<0.001	0.013	1.096 [0.969;1.241]	0.145	0.237

Conclusion

Measures of coronary artery curvature and tortuosity can be derived reproducibly based on semi-automatic analysis of cCTA. Curvature of the coronary arteries was more related to the presence of significant stenosis and plaque than tortuosity. Our findings provide a preliminary indication that higher curvature of the vessels may indicate sites that are prone to plaque development, which should be studied in follow-up studies. In conclusion, coronary artery geometry measures are potential imaging biomarkers for future risk assessment of CAD, based on common cCTA examinations.

Acknowledgements

Prof. E.R. van den Heuvel kindly provided statistical advice for this manuscript.

References

1. Wahle A, Lopez JJ, Olszewski ME, et al. Plaque development, vessel curvature, and wall shear stress in coronary arteries assessed by X-ray angiography and intravascular ultrasound. Medical image analysis. 2006;10:615-631.

2. Gijsen FJ, Wentzel JJ, Thury A, et al. A new imaging technique to study 3-D plaque and shear stress distribution in human coronary artery bifurcations in vivo. Journal of biomechanics. 2007;40:2349-2357.

3. Gibson CM, Diaz L, Kandarpa K, et al. Relation of vessel wall shear stress to atherosclerosis progression in human coronary arteries. Arteriosclerosis and thrombosis : a journal of vascular biology / American Heart Association. 1993;13:310-315.

4. Iwami T, Fujii T, Miura T, et al. Importance of left anterior descending coronary artery curvature in determining cross-sectional plaque distribution assessed by intravascular ultrasound. The American journal of cardiology. 1998;82:381-384.

5. den Dekker MA, van den Dungen JJ, Tielliu IF, et al. Prevalence of severe subclinical coronary artery disease on cardiac CT and MRI in patients with extra-cardiac arterial disease. European journal of vascular and endovascular surgery : the official journal of the European Society for Vascular Surgery. 2013;46:680-689.

6. Austen WG, Edwards JE, Frye RL, et al. A reporting system on patients evaluated for coronary artery disease. Report of the Ad Hoc Committee for Grading of Coronary Artery Disease, Council on Cardiovascular Surgery, American Heart Association. Circulation. 1975;51:5-40.

7. Leger JC. Menger curvature and rectifiability. Annals of Mathematics. 1999;149:831-869.

8. Chaikof EL, Fillinger MF, Matsumura JS, et al. Identifying and grading factors that modify the outcome of endovascular aortic aneurysm repair. Journal of vascular surgery. 2002;35:1061-1066.

9. Rubin GD, Paik DS, Johnston PC, Napel S. Measurement of the aorta and its branches with helical CT. Radiology. 1998;206:823-829.

10. Landis JR, Koch GG. The measurement of observer agreement for categorical data. Biometrics. 1977;33:159-174.

Chapter 3 Assessment of Dynamic Change of Coronary Artery Geometry and its Relationship to Coronary Artery Disease, based on Coronary CT Angiography

Publication: Geometric Differences of the Coronary Arteries during the Cardiac Cycle.
van Zandwijk JK, Tuncay V, Slump CH, Oudkerk M, Vliegenthart R, van Ooijen PMA.
Journal of Digital Imaging 2019 (Online ahead of print)

Introduction

Coronary artery disease (CAD) is the most common type of heart disease and the leading cause of death worldwide [1]. Hemodynamics and geometry of the coronary artery have been suggested to play a role in the development of atherosclerotic plaque, but these relationships are complex and still matter of debate [2]. Previous hemodynamic studies using flow simulations in static vessel models suggest an association between low wall shear stress and coronary plaque development. Thus, there may be preferred sites for plaque development depending on mechanical factors [2–6]. In studies on coronary hemodynamics in simulations incorporating cardiac motion, the importance of considering physiologically realistic flow and vessel motion was stressed [7–11]. This implies the need for in vivo, patient studies.

So far, the only evidence regarding dynamic changes of the coronary geometry originates from invasive coronary angiography (ICA). ICA is still considered the reference standard for the diagnosis of CAD, but is limited by its invasiveness and its lack of information about plaque characteristics [12]. There are scarce data from ICA studies about coronary geometry and the relation with CAD related events. Zhu et al. classified human coronary geometry in a single, diastolic phase [13]. O'Loughlin et al. found that the ratio of segment length between systolic and diastolic phase can predict the location of future culprit lesions causing myocardial infarction [14]. Coronary computed tomography angiography (cCTA) is a non-invasive imaging technique that is nowadays an accepted alternative in coronary artery evaluation [15]. cCTA is safer and cheaper than ICA, and associated with less discomfort to the patient. Three-dimensional change in coronary artery geometry during the cardiac cycle and its relationship to CAD can be investigated using cCTA with electrocardiographically synchronized data acquisition during systolic and diastolic phase. A previous study correlated the ratio of coronary artery length between end-systolic (ES) and end-diastolic (ED) phases with the location of atherosclerotic lesions, based on dual-source CT [16]. Only information about the length of coronary segments was obtained, rather than specific geometric information. Recent dedicated software packages now enable the extraction of quantifiable three-dimensional parameters of vessel geometry, derived from multiple phases of the cardiac cycle in cCTA. In a recent cross-sectional study, cCTA-derived, a relationship between measures of curvature and tortuosity in a single cardiac phase, and the presence and extent of CAD was

found [17]. Whether dynamic change of coronary curvature and tortuosity through the cardiac cycle affects the relationship with CAD, is unknown.

The current study focuses on the assessment of coronary artery geometry through the cardiac cycle based on cCTA, and the association of dynamic change in coronary artery geometry with CAD. Our hypotheses are 1) coronary artery geometry changes dynamically during the cardiac cycle; 2) the degree of stenosis and plaque types are related to dynamic changes in geometrical parameters. The novelty of this research resides in its uniqueness to quantify characteristics of movement of the coronary arteries during the cardiac cycle in a non-invasive and three-dimensional way, and in the derivation of new quantitative imaging biomarkers based on cCTA scans.

Methods and Materials

Patients

Data from patients involved in different scientific studies from April 2006 until April 2007 were included in this retrospective analysis [18–20]. Patients had either a high probability of CAD,(18) were planned for elective conventional invasive coronary angiography (ICA),[19] or were assessed at the emergency department because of acute chest pain [20]. Patients were excluded if they had previous heart surgery or percutaneous coronary intervention (PCI), or if they had a coronary anomaly on cCTA. cCTA was performed at a single tertiary center. Approval from the Medical Ethical committee was originally obtained for each scientific study, and informed consent was obtained from all patients at the time of inclusion. For the current analysis, the Medical Ethical committee waived informed consent requirement because of the retrospective nature of this study without additional burden to the patients involved.

Coronary CT Angiography Scan Protocol

cCTA was performed on a first-generation dual-source CT system (SOMATOM Definition, Siemens, Erlangen, Germany) using a standardized protocol. The standard scanning protocol involved spiral scanning at 120 kV with retrospective ECG gating. Patients were administered intravenous beta-blockers (metoprolol, 5-20 mg) if the heart rate was above 65 beats per minute, unless in case of contraindications to beta-blockers. All patients were given sublingual nitroglycerin (0.4 mg) prior to the scan protocol. Table pitch was dependent on the heart rate, with a cranio-caudal scan direction starting above the coronary ostia and ending below all cardiac structures at the diaphragm. Contrast-enhanced

scan acquisitions were made with a non-ionic contrast agent (Iomeprol 400 mg I/ml, Iomeron® 400, Bracco, Italy) with contrast volume and infusion rate individually determined for each patient. Piers et al. [19] described the scan protocol in more detail. The mean dose length product (DLP) was 1323 ± 288 mGy.cm (22.5 ± 4.9 mSv). To be included for the current analysis, reconstructions needed to have been made at every 10% of the RR-interval, with a reconstructed slice thickness of 2.0 mm based on 64 x 0.6 mm slice collimation (originally reconstructed for functional analysis).

Coronary Artery Assessment

Radiologists with experience in cardiac CT ranging from 5 to over 10 years evaluated the cCTA data for presence and severity of CAD as part of the research projects. Coronary evaluations were performed using dedicated advanced visualization software (Syngo, Siemens, Erlangen, Germany). Presence of plaque, plaque type (calcified, non-calcified, and partly calcified) and degree of stenosis were assessed per segment, according to the 15-segment modified American Heart Association (AHA) classification [21].

Coronary Artery Geometry Assessment

Reconstructed cCTA data were loaded onto a dedicated workstation (Aquarius iNtuition, Ver.4.4.11, TeraRecon, San Mateo, USA). A built-in threshold-based left ventricular ejection fraction (LVEF) analysis function automatically determined the ES and ED phase of the cardiac cycle based on respectively the minimum and maximum filling of the left ventricle. For the current study, in case the reconstruction quality of the coronary arteries in the automatically determined ES or ED phase was too low, another phase with diagnostic depiction of the coronary arteries was selected up to two phases shifted from the minimum or maximum filling. If optimal quality could not be obtained based on these restrictions, the coronary artery was excluded from further analysis.

The resulting ES and ED phases were used for detailed inspection of the coronary arteries and its individual segments, according to the 15-segment modified AHA-classification [21]. For the right coronary artery (RCA) we assessed the proximal, mid, and distal segment. For the left coronary artery we assessed the left main artery, proximal, mid, and distal segment of the left anterior descending (LAD) artery, and the proximal and distal segment of the left circumflex (LCx) artery. On artery level, the RCA, LAD, and LCx were assessed separately. In cases where no side branches where present to identify the end of the segment, we maintained equal pre-set lengths in both ES and ED phase to make

sure comparable parts of the vessel were considered. Segments were terminated or excluded when they were smaller than 1.5 mm in average diameter, had a bad reconstruction quality due to the presence of artefacts or incorrect centerline extraction, or were not visible at all. Arteries were excluded if one or more segments could not be assessed.

The coronary arteries were selected on the three-dimensional volume-rendered reconstruction (see Figure 1) or transverse slices in the relevant phase in order to initiate automatic centerline extraction of an artery. The curved planar reformation (CPR) view was reconstructed based on this centerline, after which it was manually adapted to ensure the most appropriate implementation of this centerline. Markers were applied at the beginning and endpoint of a segment. Measurements were performed for each segment and each entire artery.

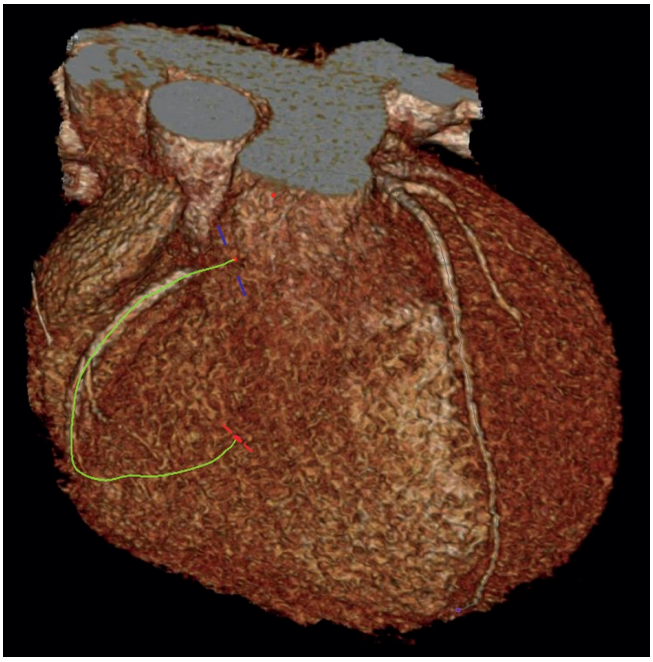

Figure 1: Example of a volume rendered 3D image with centerline extractions of the RCA (selected) and LAD at 70% of the RR-interval (ED phase).

Local curvature was calculated using Menger's formula, at every 5 mm. The average of the local curvature for the selected path is given in mm-1 as the final result for curvature. The ratio of the total path length to the straight distance between begin and endpoint of the indicated range was calculated to determine the tortuosity. The number of inflection points is determined by the maximum number of

intersections (inflection points) that the straight connection between beginning and endpoint has with the centerline when rotating the CPR view.

Statistics

Normality of the data was assessed using Shapiro-Wilk analysis. Based on the available sample size of arteries and segments, data were considered to have a normal distribution when the test statistic was greater than 0.9. Curvature, tortuosity and number of inflection points were assessed in the ES and ED phase. For curvature and tortuosity, differences were calculated as the value in ES phase minus the value in ED phase. For number of inflection points, absolute differences were assessed. The differences between ES and ED phase curvature and tortuosity measurements were tested with linear mixed model. The results were corrected for segment and artery information. On the other hand, the differences between number inflection points were tested with the non-parametric Wilcoxon signed-rank test.

Linear mixed models were applied to investigate associations between change in geometrical parameters and the severity of CAD. Severity of CAD was categorized into a number of dichotomous variables: no plaques and plaques with no lumen narrowing (LN negative group) versus plaques with lumen narrowing (LN positive, this group includes all degrees of narrowing), plaques with <50% stenosis versus plaques with >50% stenosis, and plaques with <70% stenosis versus plaques with >70% stenosis.

Associations of change in geometrical parameters with plaque types (calcified, non-calcified, and partly calcified) were investigated using linear mixed models. Estimated marginal means were used between groups in the linear mixed model depicting lumen narrowing, stenosis or plaque type.

All statistical analyses were performed in IBM SPSS Statistics version 22.0.0.1 (SPSS Inc, Chicago, USA). Significance for difference was expressed with p-values, where a two-tailed p-value of <0.05 was considered significant.

Results

Seventy-one patients in whom at least one artery could be assessed were included in this study. Mean age was 62.2 ± 9.9 years, and 87.3% were men. In total 213 arteries and 639 segments were assessed, of which 137 arteries (64.3%) and 456 segments (71.4%) could be included. Arteries and segments that could not be assessed either did not have sufficient quality in both phases, or were too small. The group of arteries consisted of 53 RCA (38.7%), 45 LAD (32.8%), and 39 LCx arteries (28.5%). 114 arteries

(83.2%) and 270 segments (59.2%) contained plaque. 0%, <50%, 50-70% , and >70% stenosis were observed in 5 (3.6%), 42(30.7%), 18(13.1%), and 49 (35.8%) of the arteries respectively. On segment level 0%, <50%, 50-70%, and >70% stenosis were observed in 51 (11.2%), 101(22.1%), 43(9.4%), and 75(16.4%) of the segments respectively.

In systole, the segments were most frequently best assessable at 40% of the R-R interval (n=227, 49.8%, range 5-60%). In 11.6% of the segments, deviation was needed from the original, software-indicated ES phase due to low reconstruction quality or motion artefacts. In diastole, the segments were most frequently best assessable at 90% of the R-R interval (n=172, 37.7%, range 70-110%). In 66.9% of the cases we deviated from the original ED phase. Although the assessed cases at 110% (i.e. 10%) of the RR-interval (n=41, 9.0%) are strictly part of the subsequent cardiac cycle, they were found to have a sufficient filling of the left ventricle to be assessed as diastolic phase.

Table 1 shows overall values for curvature, and tortuosity in ES and ED phase on (individual) artery and segment level. Figure 2 depicts a patient example of geometric parameters in the ES and ED phase.

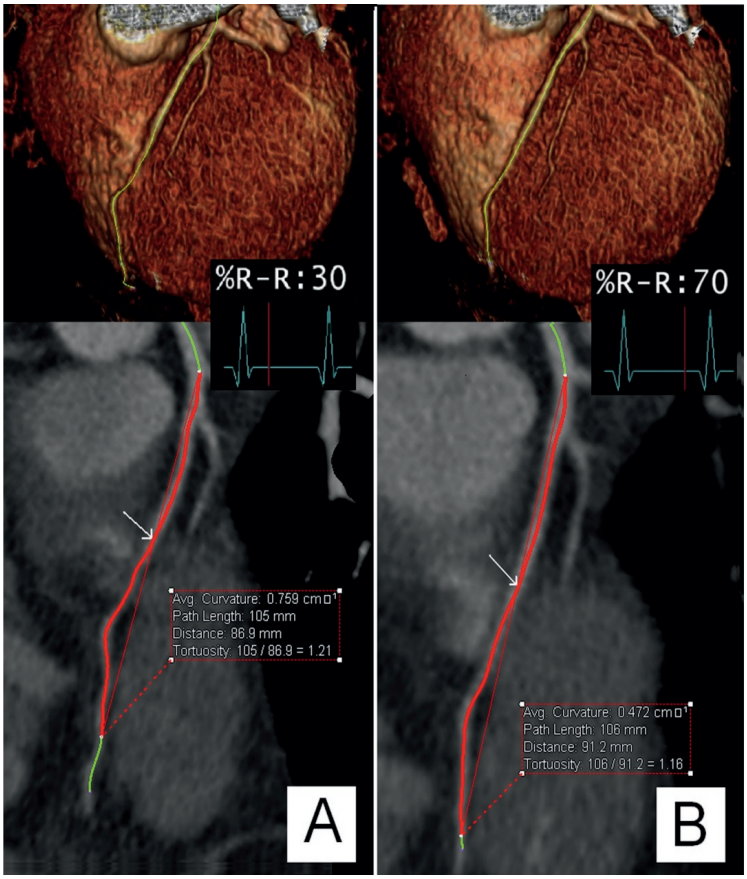

Figure 2: Geometrical measurements of the LAD at 30% in ES phase (A) and at 70% in ED phase (B). According to these measurements, the LAD has 26% higher curvature, and 3% higher tortuosity in ES phase. The white arrows indicate one inflection point in both phases.

Curvature

Curvature in ES and ED phase, and differences in curvature were normally distributed. Compared to the ED phase, the mean curvature was 11.1% higher in the ES phase on artery level ($p=0.002$), and 8.9% higher on segment level ($p<0.001$) (Table 1).

Tortuosity

Tortuosity differences were normally distributed. The mean tortuosity was 2.3% higher in end-systole than in end-diastole on artery level ($p=0.09$), and 1.8% higher on segment level ($p=0.005$) (Table 1).

Inflection Points

The difference in number of inflection points was not normally distributed on artery and on segment level (Shapiro-Wilk statistic value 0.755 and 0.564, respectively (both $p<0.001$)). The mean number of inflection points was significantly higher at ES phase than at ED phase for both artery ($Z=3.793$, $p<0.001$) and segment level ($Z=5.415$, $p<0.001$) (Table 1).

Table 1: Outcomes of the measured parameters in end-systolic (ES) and end-diastolic (ED) phase on artery and segment level, depicted as mean (mean standard error). Significant differences are indicated with an asterisk.

		Arteries (n=137)		**Segment (n=456)**	
Parameter	**Phase**	**Outcome**	**p-value**	**Outcome**	**p-value**
Curvature (mm^{-1})	**ES**	0.090(0.002)	0.002	0.085(0.002)	<0.001*
	ED	0.081(0.002)		0.078(0.001)	
Tortuosity	**ES**	1.36(0.026)	0.09	1.12(0.005)	0.005*
	ED	1.33(0.026		1.10(0.005)	
Inflection points	**ES**	2.20(0.095)	<0.001*	0.63(0.038)	<0.001*
	ED	1.96(0.091)		0.51(0.034)	

Associations between Geometrical Parameters and Stenosis

There was no significant association between the change in geometric parameters through the cardiac cycle, and stenosis (Table 2 and Table 3).

Table 2: Linear mixed model associations between geometrical parameters and stenosis on artery level. Dependent variables (differences between ES and ED values) are depicted in the rows, factors in columns. LN- means group with no lumen narrowing, LN+ the group segments with lumen narrowing. EMM are estimated marginal means, with in parenthesis the standard errors.

Change in Geometrical Parameters (Δ)	LN-	LN+	p-value	Stenois <50%	Stenosis >50%	p-value	Stenonis <70%	Stenosis >70%	p-value
Curvature (mm^{-1}) EMM	0.006 (0.003)	0.008 (0.001)	0.428	0.006 (0.002)	0.009 (0.002)	0.142	0.006 (0.001)	0.009 (0.002)	0.241
Tortuosity EMM	0.057 (0.012)	0.036 (0.006)	0.098	0.035 (0.007)	0.046 (0.008)	0.299	0.039 (0.007)	0.042 (0.009)	0.785
Inflection points EMM	0.11 (0.13)	0.27 (0.07)	0.281	0.16 (0.08)	.031 (0.08)	0.185	0.24 (0.07)	0.23 (0.10)	0.913

Table 3: Linear mixed model associations between geometrical parameters and stenosis on segment level. Dependent variables (differences between ES and ED values) are depicted in the rows, factors in columns. LN- means group with no lumen narrowing, LN+ the group segments with lumen narrowing. EMM are estimated marginal means, with in parenthesis the standard errors.

Change in Geometrical Parameters (Δ)	LN-	LN+	p-value	<50%	>50%	p-value
Curvature (mm^{-1}) EMM	0.006 (0.001)	0.008 (0.001)	0.279	0.007 (0.001)	0.008 (0.002)	0.607
Tortuosity EMM	0.019 (0.003)	0.016 (0.003)	0.440	0.018 (0.002)	0.017 (0.004)	0.798
Inflation points EMM	0.14 (.003)	0.10 (0.03)	0.339	0.13 (.003)	0.10 (0.04)	0.624

Associations between Geometrical Parameters and Plaque Types

Association results for plaque type are given in Table 4. None of the dynamic geometrical parameters were significantly associated with type of plaque.

Table 4: Linear mixed model associations between geometrical parameters and plaque type at segment level. EMM are estimated marginal means, with in parenthesis the standard errors.

Change in Geometrical Parameters (Δ)	Calcified	Non-calcified	Partly calcified	P-value
Curvature (mm^{-1}) EMM	0.007 (0.002)	0.005 (0.003)	0.010 (0.002)	0.427
Tortuosity EMM	0.018 (0.004)	0.015 (0.006)	0.020 (0.004)	0.796
Inflation points EMM	0.17 (0.05)	0.11 (0.07)	0.06 (0.05)	0.317

Discussion

This study shows that the geometric parameters of coronary arteries change significantly between the ES and ED phase except for the tortuosity at the artery level. However, we found no significant relationship between geometric changes through the cardiac cycle and extent of CAD. To our knowledge, this is the first patient study quantifying coronary geometry during the cardiac cycle based on straightforward post-processing of four-dimensional non-invasive imaging data.

Previous studies focusing on the relation between vessel geometry, corresponding hemodynamics, [7–9,11] and plaque development [6,22–24] were often based on computational fluid dynamics, and were thus accompanied by modeling assumptions requiring a considerable amount of time and computational capacity [6,25]. These studies found that hemodynamic and geometric parameters can be linked to (early) plaque development, but conclusions were drawn based on modeling or static approaches of the coronary arteries. Moreover, there have been studies quantifying and cataloguing the geometric parameters of coronary arteries with invasive imaging techniques. Zhu et al. used ICA to measure geometry of the proximal, mid, and distal segments separately of the RCA and LAD in one phase, and found, for instance, a two-fold difference in maximum curvature in LAD segments between individuals. They state that a particular geometric feature must exhibit large variability between vascular regions or individuals, if it should be considered as an atherosclerotic risk factor. They also suggested to add a dynamic dimension in addition to their work, which can create even more variability [13]. In the study of Johnson et al, biplane cine angiography was used for the quantifications, which is an invasive method in contrast to CT, and so only applicable in selected patients at high suspicion of CAD. Furthermore, this involves two projection directions, requiring additional reconstruction algorithms to obtain three-dimensional information [26]. In a recent study, Tuncay et al. assessed the relationship between curvature and tortuosity of coronary arteries and the presence of significant stenosis and plaque [17]. They reported that static coronary artery geometry is related with the presence of plaque and significant stenosis. However, in this study all the analyses were done in diastolic phase. The effect of dynamic change of coronary artery geometry was not investigated. The only patient study slightly resembling ours was conducted by O'Loughlin et al., [16] but they only investigated the length of segments, and only included a few segments of the coronary tree. Strength of our study resides in the fact that coronary arteries were geometrically quantified based on four-dimensional cCTA data involving multiple phases

of the cardiac cycle. Our method involves more detailed and three-dimensional geometric information in terms of curvature, tortuosity, and inflection of both segments and arteries, through the cardiac cycle.

This study has some limitations. Firstly, we performed measurements based on a semi-automatically extracted centerline in the CT datasets. The centerline creation did not always yield an accurate result. Especially extraction of severely diseased coronary arteries was frequently incorrect, thus requiring manual adaptation of the centerline to achieve a better match with the vessel trajectory. This could have affected our geometric measurements. Secondly, corresponding segments from the same patient were equivalently adapted in both phases to minimize intra- and inter-observer variability, but this is still a possible shortcoming of the study since variability was introduced. Furthermore in case image quality at the automatically determined ES or ED phase was too low, another phase was selected up to two phases from the minimum or maximum filling. This might also compromise the assessment of dynamic geometry change of coronary arteries between ES and ED phase. Furthermore, this is a retrospective non-randomized study. Same quantification technique can be employed in a randomized prospective study with a larger patient group in order to further investigate the relationship between dynamic behavior of coronary arteries and CAD. Finally, this study was performed using older dual-source CT technology, which at the time involved retrospective ECG gating for cCTA, resulting in high, nowadays outdated, radiation dose. We do not suggest to perform four-dimensional CT imaging of the coronary arteries for clinical routine, but merely used the existing data from previous studies to extract additional information which allowed to test our hypothesis on geometrical changes through the cardiac cycle, and its relation to CAD. However, with newer CT technology, it is possible to modulate tube current during the cardiac cycle, which allows evaluation of multiple phases from systolic to diastolic phase (f.e. 30-70%) at acceptable radiation dose.

Conclusion

In conclusion, this study investigated the dynamic behavior of coronary artery geometry during the cardiac cycle and its relationship to CAD using four-dimensional, non-invasive imaging method. Curvature, tortuosity and inflection points measures were significantly higher in ES phase compared to ED phase for coronary arteries as well as individual coronary segments. While absolute measures of curvature and tortuosity were related to presence and extent of CAD, dynamic change of vessel geometry through the cardiac cycle was not related. This study also shows that cardiac CT allows non-

invasive quantification of coronary geometry through the cardiac cycle that helps to study potential biomechanical mechanisms underlying CAD development.

Acknowledgements

The authors would like to thank Mr. Sha He, Senior Medical Software Engineer, TeraRecon Inc, San Francisco for technical support and providing information about the software algorithms embedded in the Aquarius iNtuition software.

References

1. Budoff MJ, Achenbach S, Blumenthal RS, et al. Assessment of coronary artery disease by cardiac computed tomography. Circulation 2006;114(16):1761–91.

2. Wahle A, Lopez JJ, Olszewski ME, et al. Plaque development, vessel curvature, and wall shear stress in coronary arteries assessed by X-ray angiography and intravascular ultrasound. Med Image Anal 2006;10(4):615–31.

3. Iwami T, Fujii T, Miura T, et al. Importance of Left nterior Descending Coronary Artery Curvature in Determining Cross-Sectional Plaque Distribution Assessed by Intravascular Ultrasound. Am J Cardiol 1998;82:381–4.

4. Johnston BM, Johnston PR. The relative effects of arterial curvature and lumen diameter on wall shear stress distributions in human right coronary arteries. Phys Med 2007;52(9):2531–44.

5. Xie X, Wang Y, Zhou H. Impact of coronary tortuosity on the coronary blood flow: A 3D computational study. J Biomech 2013;46(11):1833–41.

6. Malvè M, Gharib AM, Yazdani SK, et al. Tortuosity of Coronary Bifurcation as a Potential Local Risk Factor for Atherosclerosis: CFD Steady State Study Based on In Vivo Dynamic CT Measurements. Ann Biomed Eng 2015;43(1):82–93.

7. Zeng D, Ding Z, Friedman MH, et al. Effects of Cardiac Motion on Right Coronary Artery Hemodynamics. Ann Biomed Eng 2003;31(4):420–9.

8. Prosi M, Perktold K, Ding Z, et al. Influence of curvature dynamics on pulsatile coronary artery flow in a realistic bifurcation model. J Biomech 2004;37(11):1767–75.

9. Pivkin I V, Richardson PD, Laidlaw DH, et al. Combined effects of pulsatile flow and dynamic curvature on wall shear stress in a coronary artery bifurcation model. J Biomech 2005;38(6):1283–90.

10. Theodorakakos A, Gavaises M, Andriotis A, et al. Simulation of cardiac motion on non-Newtonian, pulsating flow development in the human left anterior descending coronary artery. Phys Med Biol 2008;53(18):4875–92.

11. Torii R, Keegan J, Wood NB, et al. The effect of dynamic vessel motion on haemodynamic parameters in the right coronary artery: a combined MR and CFD study. Br J Radiol 2009;82:S24-32.

12. Springer I, Dewey M. Comparison of multislice computed tomography with intravascular ultrasound for detection and characterization of coronary artery plaques: a systematic review. Eur J Radiol 2009;71(2):275–82.

13. Zhu H, Ding Z, Piana RN, et al. Cataloguing the geometry of the human coronary arteries: A potential tool for predicting risk of coronary artery disease. Int J Cardiol 2009;135(1):43–52.

14. O'Loughlin AJ, Kazi S, French JK, et al. Quantitative Coronary Artery Motion Analysis Predicts the Location of Future ST Segment Elevation Myocardial Infarctions. Int J Cardiovasc Cerebrovasc Dis 2014;2(3):35–8.

15. Pelliccia F, Pasceri V, Evangelista A, et al. Diagnostic accuracy of 320-row computed tomography as compared with invasive coronary angiography in unselected, consecutive patients with suspected coronary artery disease. Int J Cardiovasc Imaging 2013;29(2):443–52.

16. O'Loughlin AJ, Tang L, Moses D, et al. A Novel Quantitative Index of Coronary Artery Motion from Multislice Computed Tomography and the Location of Coronary Artery Disease. Int J Cardiovasc Cerebrovasc Dis 2014;2(1):1–5.

17. Tuncay V, Vliegenthart R, den Dekker MAM, et al. Non-invasive assessment of coronary artery geometry using coronary CTA. J Cardiovasc Comput Tomogr 2018[Epub ahead of print]

18. de Vos AM, Rutten A, van de Zaag-Loonen HJ, et al. Non-invasive cardiac assessment in high risk patients (The GROUND study): rationale, objectives and design of a multi-center randomized controlled clinical trial. Trials 2008;9:49.

19. Piers LH, Dikkers R, Willems TP, et al. Computed tomographic angiography or conventional coronary angiography in therapeutic decision-making. Eur Heart J 2008;29(23):2902–7.

20. Willemsen HM, de Jong G, Tio RA, et al. Quick identification of acute chest pain patients study (QICS). BMC Cardiovasc Disord 2009;9:24.

21. Austen WG, Edwards JE, Frye RL, et al. A reporting system on patients evaluated for coronary artery disease. Report of the Ad Hoc Committee for Grading of Coronary Artery Disease, Council on Cardiovascular Surgery, American Heart Association. Circ 1975;51(4):5–40.

22. Zhang C, Xie S, Li S, et al. Flow patterns and wall shear stress distribution in human internal carotid arteries: the geometric effect on the risk for stenoses. J Biomech 2012;45(1):83–9.

23. Katranas SA, Antoniadis AP, Kelekis AL, et al. Insights on atherosclerosis by non-invasive assessment of wall stress and arterial morphology along the length of human coronary plaques. Int J Cardiovasc Imaging 2015;31(8):1627–33.

24. El Tahlawi M, Sakrana A, Elmurr A, et al. The relation between coronary tortuosity and calcium score in patients with chronic stable angina and normal coronaries by CT angiography. Atherosclerosis 2016;246:334–7.

25. Kim HJ, Vignon-Clementel IE, Coogan JS, et al. Patient-specific modeling of blood flow and pressure in human coronary arteries. Ann Biomed Eng 2010;38(10):3195–209.

26. Johnson MJ, Dougherty G. Robust measures of three-dimensional vascular tortuosity based on the minimum curvature of approximating polynomial spline fits to the vessel mid-line. Med Eng Phys 2007;29(6):677–90.

Chapter 4 Towards Quantification of Non-Calcified coronary Atherosclerotic Plaque on CT: Correction of Lumen Contrast-Enhancement Influence.

Publication: Correction of lumen contrast-enhancement influence on non-calcified coronary atherosclerotic plaque quantification on CT

Kristanto W, Tuncay V, Vliegenthart R, Oudkerk M, van Ooijen PMA.

Int J Cardiovascular Imaging 2015;31:429-436.

Introduction

In coronary artery disease (CAD), atherosclerotic plaque develops in the wall of the coronary artery, potentially leading to significant narrowing of the lumen and/or occlusion of the artery, hindering the blood supply of the heart muscle. An acute coronary syndrome (ACS) as a result of CAD is currently the leading cause of death in the western world [1]. Early detection of CAD is essential in order to start treatment timely and prevent or delay the progress of disease.

Previous publications demonstrated that coronary stenosis [2, 3] and calcified plaque burden [4-6], two main parameters for estimating CAD event risk, can be quantified reliably by multi detector-row computed tomography (MDCT).

Quantification of non-calcified plaques is of increasing interest in diagnosis and clinical workup as plaques with large lipid-rich components are considered to be more rupture prone and subsequently are more likely to cause an ACS [7]. One of the most common and most validated methods to identify and quantify lipid-rich plaque is intravascular ultrasound [8, 9]. However, identification of lipid-rich plaque using MDCT is highly preferable because of its non-invasive nature. MDCT can reportedly characterize non-calcified plaques by virtue of their specific CT density in Hounsfield Units (HU) [10-13]. However, to use a generalized HU-criterion is not yet possible as the reported HU-values vary considerably. Many factors have been reported to influence non-calcified coronary plaque HU values, one of the most prominent being the lumen contrast-enhancement [14-18]. In a preliminary software phantom simulation study, the lumen contrast-enhancement was shown to influence the surrounding coronary wall with a specific pattern [19]. This vessel phantom study aimed to construct and validate an algorithm to correct for the lumen contrast-enhancement influence in order to obtain the correct HU values for the characterization and quantification of non-calcified plaques.

Material and Methods

Several specifically designed coronary vessel phantoms (QRM GmbH, Moehrendorf, Germany) were used in this study. Using these phantoms, the previously found lumen contrast-enhancement influence pattern was reproduced. Based on the reproduced patterns, a generalized correction algorithm was constructed and validated.

Phantom Experiment

Three coronary vessel phantoms with 1, 2, and 4 mm diameter circular hollow lumina were used in the experiment. The vessel wall was designed to be 35 HU in CT density and 3 mm in thickness, and part of each vessel phantom was infested with an artificial plaque of -10 HU in CT density, 2 mm in thickness, and 5 mm in length (Figure 1A, these 2 different segments of the wall will be referred to as normal and plaque-infested wall, respectively, for the remainder of the article).

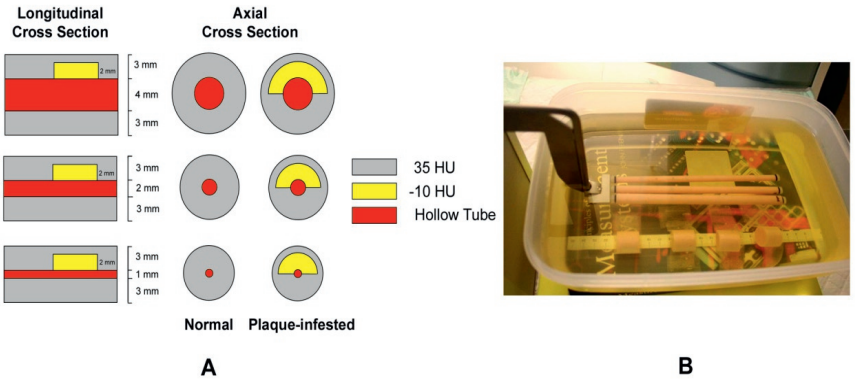

Figure 1: The phantom diagram (A) and experimental setup (B).

The phantoms were scanned simultaneously while submerged in sun flower oil with a dual-source computed tomography scanner (Siemens Definition, Siemens Medical Solution, Forchheim, Germany) at 120kV, 300mAs/rot, and 64x0.6mm (Figure 1B). Scanning was performed five times with the lumen alternately filled with water and 4 contrast solutions of approximately 100, 200, 300, and 400 HU. Images were reconstructed at 0.6 mm slice thickness with 0.4 mm increment.

In total, 30 datasets were obtained with the following properties: 3 lumen sizes (1, 2, and 4 mm diameter) x 2 wall types (normal and plaque-infested wall) x 5 lumen contents (water or 1 of the 4 different contrast solutions).

Analysis

The images were analyzed using a custom-made software tool written in Matlab® (Mathworks Inc, USA). The following analysis steps were performed.

Analysis Sets Construction

Two types of analysis sets are constructed from each datasets, a training set and a validation set. A training set was constructed by averaging the 10 selected slices for every dataset, in order to minimize noise. This training set was then used to study the correlation between HU values of wall and lumen; and to extract the lumen contrast-enhancement influence pattern.

A validation set was constructed by arbitrarily selecting one slice of each dataset. The validation set was used to apply and test the formulated lumen contrast-enhancement influence correction algorithm (see section Validation).

Wall and Lumen ROI Segmentation

Lumen and wall (normal and plaque-infested) HU-values were measured inside ROIs that matched the designed morphology. The lumen was semi-automatically detected using an algorithm used in a previous publication [20]. A circle of the designed lumen size is fitted to the detected lumen boundary to yield the lumen ROI. The wall ROI was defined as the area between the lumen circular ROI and a larger circle with the same axis and a diameter conforming to the designed plaque thickness. The wall ROI left out the outer part of the wall which is blurred by the partial volume averaging with the surrounding.

Lumen Contrast –Enhancement Influence Pattern Extraction

Pixel by pixel comparisons were performed between contrast-enhanced images (of lumen CT density: 100, 200, 300, and 400 HU) and non-contrast-enhanced images (of lumen CT density: 0 HU) to extract the lumen contrast-enhancement. It is done by first aligning both images based on their outer vessel contour (obtained by 0 HU threshold [21]) and then subtracting the latter from the former (Figure 2). The comparisons resulted in difference images containing only the contribution of the contrast to the image (Figure 2C). The wall ROI from the previous step was used to delineate the wall area of the difference image (Figure 2D) and extract the contribution of the contrast to the wall area (Figure 2E). The value of every pixel inside this ROI was plotted against its distance from the lumen border. An exponential line ($y = Ae^{-\lambda x} + c$) was fitted through the data points, with A, λ, x, and c indicating the amplitude, coefficient, distance from lumen border, and constant, respectively, using a custom made Matlab® program which minimizes the squared error between the data points and the approximation line.

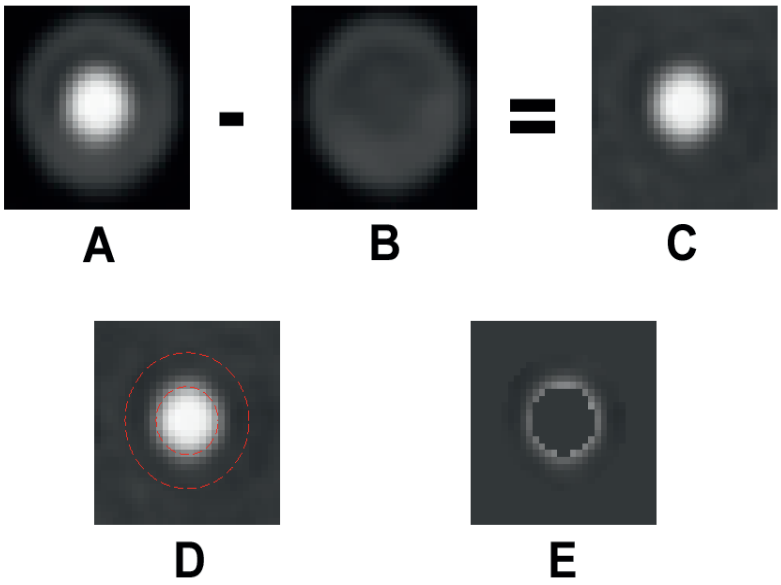

Figure 2: Pixel by pixel comparison between contrast-enhanced image (A) and non-contrast-enhanced image (B) by subtracting the latter from the former, resulting in a difference image (C). The wall ROI (striped red line) was overlaid onto the difference image (D), from which the lumen contrast-enhancement influence on the wall was extracted (E).

Validation

In a previous study using software phantoms, it was demonstrated that the lumen contrast-enhancement influences the surrounding wall HU values up to a 2-pixel radius from the lumen border [19]. Therefore, the obtained lumen contrast-enhancement influence lines were applied to the contrast-enhanced image to correct for the lumen contrast-enhancement influence on the surrounding wall up to a 2-pixel radius from the lumen border.

Non-contrast enhanced images of each vessel and wall type were defined as the reference images. The wall HU-values outside the 2-pixel radius were compared between contrast-enhanced images and the reference to check the validity of selecting only inside the 2-pixel radius for applying the correction algorithm. Subsequently, the wall HU-values for the inside 2-pixel radius and for the whole plaque, were compared to the reference, before and after correction.

Results

Lumen contrast-enhancement influence pattern

An exponential line ($y = Ae^{-\lambda x} + c$) approximated the lumen contrast-enhancement influence on the surrounding wall (Figure 3). The lumen contrast-enhancement influence patterns for the two types of wall were similar for each vessel type, except for the smallest vessel (Figure 4).

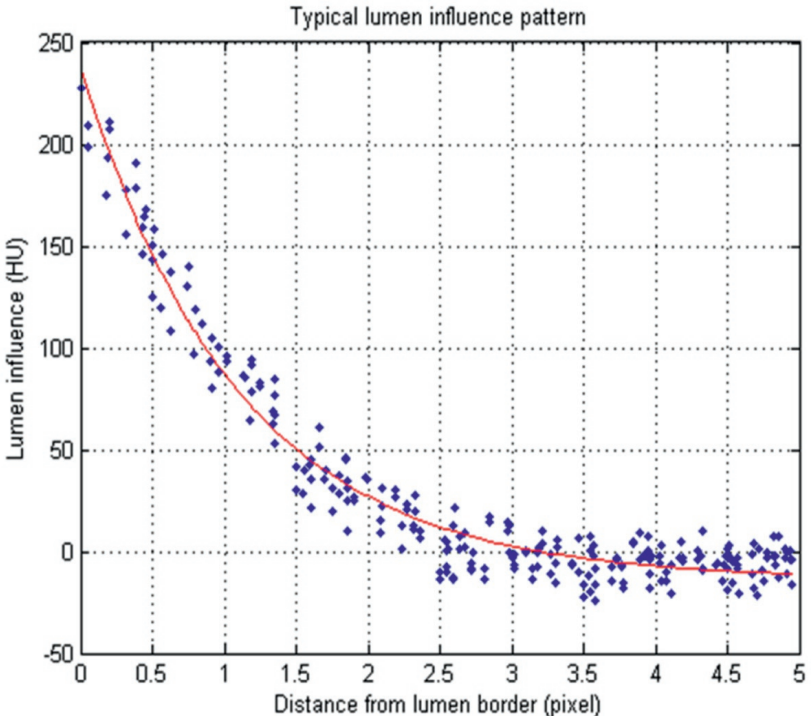

Figure 3: Typical lumen contrast-enhancement influence on the surrounding wall, plotted against the distance to the lumen border (blue dots), which was approximated by an exponential line (red line).

The obtained influence patterns (Figure 4) were applied to the training set to correct for the lumen contrast-enhancement influence. The difference between the mean HU-values of the wall to the reference, before and after correction, can be seen at Table 1 (training set).

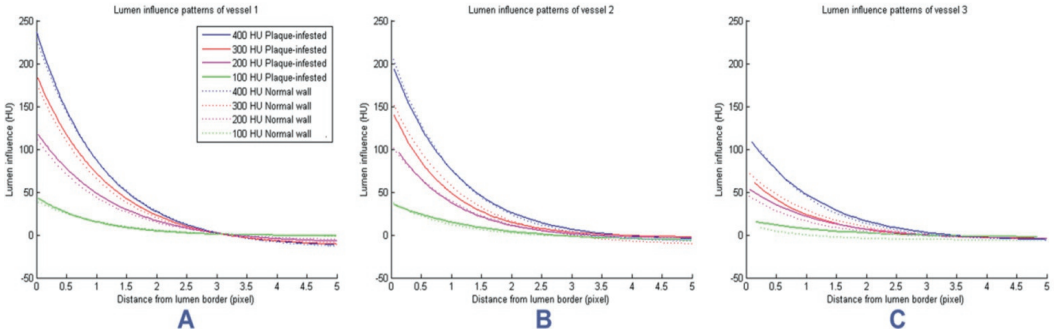

Figure 4: The lumen contrast-enhancement influence patterns for large (A), medium (B), and small (C) vessels.

Generalized Lumen Contrast-Enhancement Influence Pattern

To enhance the applicability of the lumen contrast-enhancement influence pattern, a generalized version of the correction algorithm was formulated. Combining all the parameters of the exponential lines from all vessels and all types of wall, the amplitudes (A) were found to be linearly correlated to the mean lumen HU-values (r2 = 0.96), following a linear equation: $A = 0.66 * Lumen\_HU + 4$ (Figure 5A). Meanwhile, the coefficients (λ) were similar: 0.9+0.1, and the constants (c) were linearly correlated to the mean lumen HU values (r2 = 0.64), following a linear equation: $c = -0.03 * Lumen\_HU - 2$ (Figure 5B).

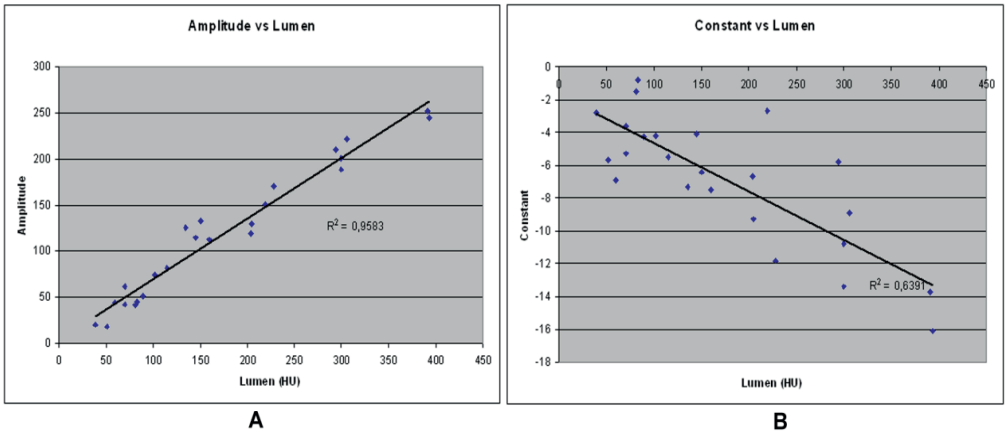

Figure 5: The correlation between the amplitudes (A) and the lumen mean HU values and between the constants (B) and the lumen mean HU values

The generalized correction algorithms were applied to the validation set to correct for the lumen contrast-enhancement influence (Figure 6 and 7). The differences of the walls mean HU-values to the reference, before and after correction, can be seen at Table 1 (validation set).

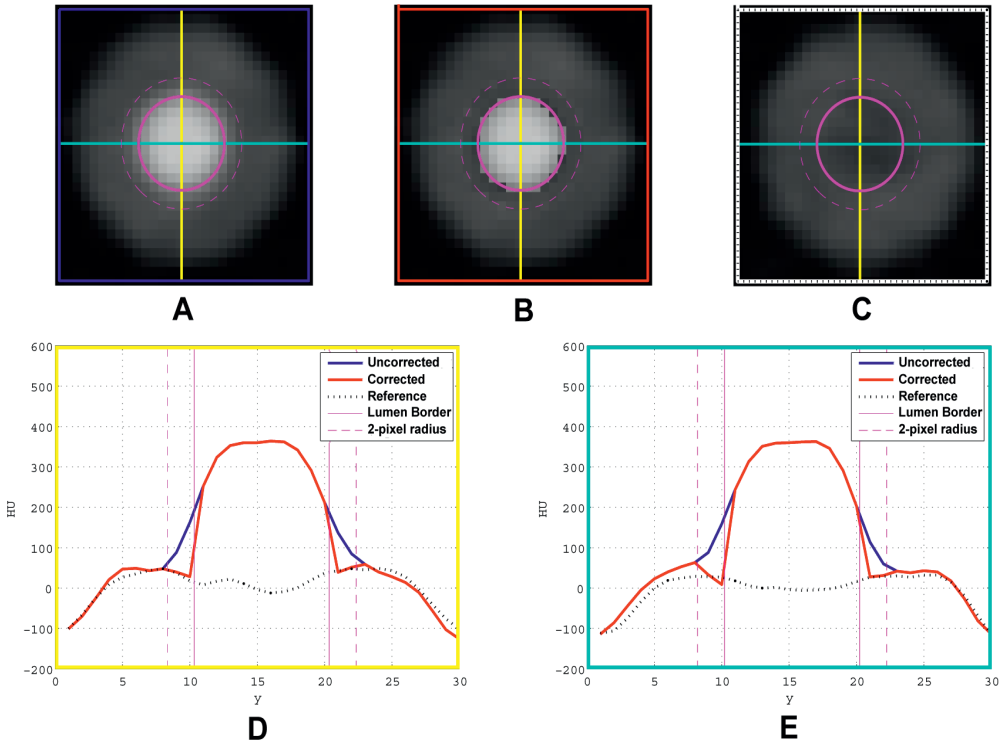

Figure 6: The effect of the formulated correction algorithm on the normal wall. This figure shows the uncorrected contrast-enhanced image (A), the corrected contrast-enhanced image (B), and the non-contrast-enhanced reference image (C). The lumen border is shown by the solid magenta circle, and the 2-pixel radius by the striped magenta circle. The HU profiles along the vertical (yellow lines) and horizontal (cyan lines) directions of the three images are plotted on top of each other in image D and E, respectively.

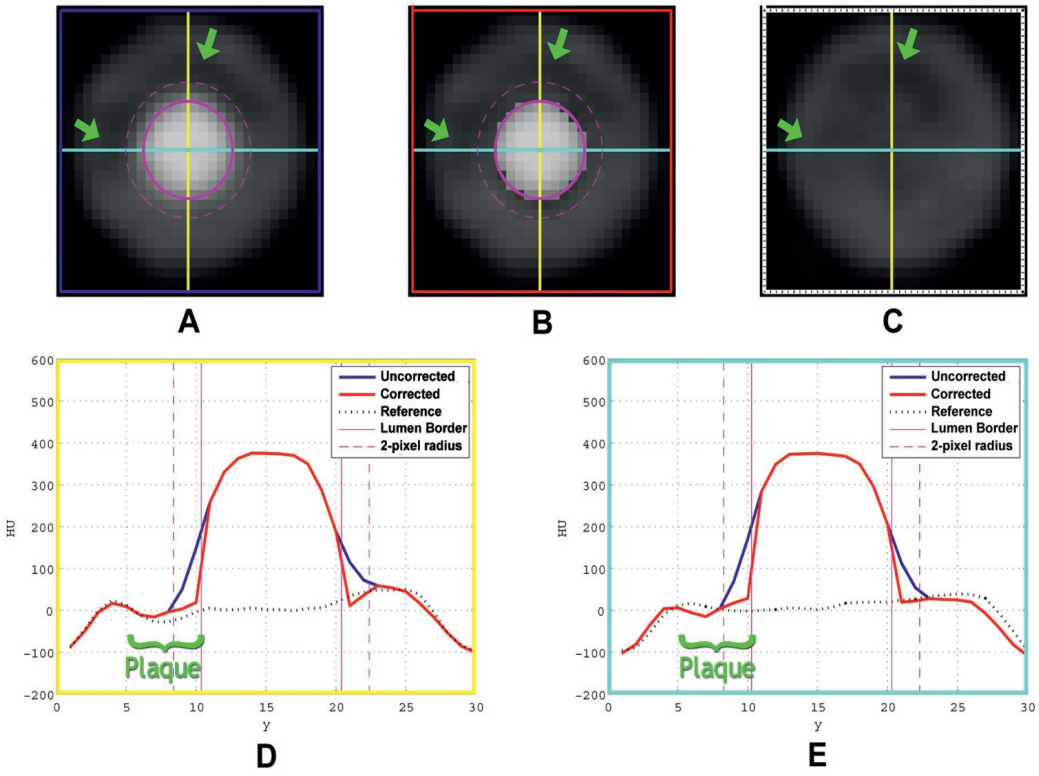

Figure 7: The effect of the formulated correction algorithm on the plaque-infested wall. This figure shows the uncorrected contrast-enhanced image (A), the corrected contrast-enhanced image (B), and the non-contrast-enhanced reference image (C). The lumen border is shown by the solid magenta circle, and the 2-pixel radius by the striped magenta circle. The HU profiles along the vertical (yellow lines) and horizontal (cyan lines) directions of the three images are plotted on top of each other in image D and E, respectively. The range of the plaque infestation is marked by the green arrows on image A, B, and C; and by the green text in image D and E.

Table 1: The difference of walls mean HU-values to the reference

Set	Part of the wall Measured	Difference to Reference	
		No Correction	**Correction**
Training	Outside 2-pixel radius	0-7 HU (2 HU)	NC
	Inside 2-pixel radius	0-95 HU (44 HU)	0-6 HU (1 HU)
	Whole wall	1-30 HU (11 HU)	0-4 HU (1 HU)
Validation	Outside 2-pixel radius	0-8 (2 HU)	NC
	Inside 2-pixel radius	4-98 HU (45 HU)	0-15 HU (4 HU)
	Whole wall	1-30 HU (10 HU)	0-8 HU (2 HU)

Note:

1. The values on Difference to Reference columns indicate the range with the median in the bracket
2. NC: no correction performed

Discussion

Many factors have been reported to influence the HU values of plaques [14, 22, 23], with lumen contrast-enhancement being the most prominent one. The lumen contrast-enhancement influence to the surrounding tissue is mainly attributed to partial volume effect [24]. This effect is inevitable because of the limited spatial resolution of current human CT hardware, relative to the coronary size. A review study on published HU-criteria to distinguish non-calcified coronary plaques [25] has investigated the possible role of the study characteristics to the variability of the HU-criteria. As shown in this review, the connection between the reported lumen-contrast enhancements and the HU-criteria failed to be established. Several studies managed to further investigate the lumen contrast-enhancement and showed that the influence was dependent on the location of plaque relative to lumen [17, 18], with stronger

influence on CT attenuation of non-calcified plaque close to the lumen. New development involving dual energy CT managed to virtually remove of contrast-enhancement [26] but is not yet applicable in contrast-enhancement removal at coronaries.

A previous study, [19] using a software simulation has identified the exact pattern of lumen contrast-enhancement. The same pattern, which resembles one-half of an exponential sigmoid curve, has been previously used as an image edge model [27]. By using CT experiment on vessel phantoms, this current study managed to reproduce and validate this lumen influence pattern ($y = Ae^{-\lambda x} + c$) in data obtained using clinical CT protocols on a clinical CT scanner. The amplitudes (A), which determine the magnitude of the exponential pattern, showed strong positive linear correlation to the lumen HU values which can be explained by the fact that CT is a linear system. The lambda (λ) coefficients express the range of the exponential pattern. The fact that they are relatively stable confirms that the influence range is mostly dependent on the spatial resolution of the CT system. The negative linear correlation between the constants (c) and the lumen HU-values may first seem counter intuitive as this will decrease the influence as the lumen HU values increase. This finding may be due to the Gibbs phenomenon, commonly associated with discontinuities in images [28]. However, the relatively weak correlation and small values indicate that this effect is not prominent. The close similarity of the influence patterns between all types of wall indicates the independency of wall types. The slight dissimilarity in the influence patterns between the two wall types of the small vessels (Figure 6C – influence from 100 and 200 HU lumen value) was caused by the difficulty to correctly segment the boundary of the small (approximately 2 pixels diameter) and low attenuation lumina.

The proposed correction algorithm managed to correct for the lumen contrast-enhancement influence on the most affected wall region, which is within a 2-pixel radius from the lumen border, reducing the median difference of 45 HU to a median difference of 4 HU, with reference to non contrast-enhanced vessel. When the whole wall region was measured, the median difference decreased from 10 HU to 2 HU.

A limitation of the study is that the HU values of the vessel wall (either the normal or the plaque-infested wall) do not specifically refer to any of the published plaque-specific HU values. However, the pattern of the lumen contrast-enhancement influence is independent to the wall types. The only variables that determined the pattern are the mean lumen HU-values and the spatial resolution of the CT system.

Another shortcoming is the fact that the coronary phantoms were scanned stationary and thus, the effect of coronary motion was not taken into account in this study. Future studies should be conducted to validate our correction algorithm using moving phantoms. However, the current correction algorithm could already be applied to other types of vessels where cardiac motion plays no role such as the carotids or peripheral vessels. The data used in this study was reconstructed using the most commonly used reconstruction kernel in our institution for cardiac CT examination. However, the use of other reconstruction kernels may produce different the lumen contrast-enhancement smearing pattern. Future validation studies should also cover other variations in experimental settings.

Conclusion

Lumen contrast-enhancement influence on the vessel wall can be defined by an exponential approximation, allowing correction of the CT density of the vessel wall closest to the lumen. After this correction, a more accurate determination of the composition of the vessel wall plaques can be made.

Acknowledgements

The authors would like to acknowledge the contribution of Estelle Noach in providing extensive remarks on the manuscript.

References

1 Heron MP, Smith BL. (2007) Deaths: leading causes for 2003. Natl Vital Stat Rep 55:1-92

2 Korosoglou G, Mueller D, Lehrke S, et al. (2010) Quantitative assessment of stenosis severity and atherosclerotic plaque

composition using 256-slice computed tomography. Eur Radiol 20:1841-1850

3 Leber AW, Johnson T, Becker A, et al. (2007) Diagnostic accuracy of dual-source multi-slice CT-coronary angiography in patients with an intermediate pretest likelihood for coronary artery disease. Eur Heart J 28:2354-2360

4 Agatston AS, Janowitz WR, Hildner FJ, et al. (1990) Quantification of coronary artery calcium using ultrafast computed tomography. J Am Coll Cardiol 15:827-832

5 Oudkerk M, Stillman AE, Halliburton SS, et al. (2008) Coronary artery calcium screening: current status and recommendations from the European Society of Cardiac Radiology and North American Society for Cardiovascular Imaging. Int J Cardiovasc Imaging 24:645-671

6 Oudkerk M, Stillman AE, Halliburton SS, et al. (2008) Coronary artery calcium screening: current status and recommendations from the European Society of Cardiac Radiology and North American Society for Cardiovascular Imaging. Eur Radiol 18:2785-2807

7 Virmani R, Burke AP, Farb A, Kolodgie FD. (2006) Pathology of the vulnerable plaque. J Am Coll Cardiol 47:13-18

8 Nasu K, Tsuchikane E, Katoh O, et al. (2006) Accuracy of in vivo coronary plaque morphology assessment: a validation study of in vivo virtual histology compared with in vitro histopathology. J Am Coll Cardiol 47:2405-2412

9 Nishimura RA, Edwards WD, Warnes CA, et al. (1990) Intravascular ultrasound imaging: in vitro validation and pathologic correlation. J Am Coll Cardiol 16:145-154

10 Brodoefel H, Reimann A, Heuschmid M, et al. (2008) Characterization of coronary atherosclerosis by dual-source computed tomography and HU-based color mapping: a pilot study. Eur Radiol 18:2466-2474

11 Leber AW, Knez A, Becker A, et al. (2004) Accuracy of multidetector spiral computed tomography in identifying and differentiating the composition of coronary atherosclerotic plaques A comparative study with intracoronary ultrasound. J Am Coll Cardiol 43:1241-1247

12 Motoyama S, Kondo T, Anno H, et al. (2007) Atherosclerotic Plaque Characterization by 0.5-mm-Slice Multislice Computed Tomographic Imaging: Comparison With Intravascular Ultrasound. Circ J 71:363-366

13 Schroeder S, Kopp AF, Baumbach A, et al. (2001) Noninvasive detection and evaluation of atherosclerotic coronary plaques with multislice computed tomography. J Am Coll Cardiol 37:1430-1435

14 Cademartiri F, Mollet NR, Runza G, et al. (2005) Influence of intracoronary attenuation on coronary plaque measurements using multislice computed tomography: observations in an ex vivo model of coronary computed tomography angiography. Eur Radiol 15:1426-1431

15 Ferencik M, Chan RC, Achenbach S, et al. (2006) Arterial wall imaging: evaluation with 16-section multidetector CT in blood vessel phantoms and ex vivo coronary arteries. Radiology 240:708-716

16 Halliburton SS, Schoenhagen P, Nair A, et al. (2006) Contrast enhancement of coronary atherosclerotic plaque: a high-resolution, multidetector-row computed tomography study of pressure-perfused, human ex-vivo coronary arteries. Coron Artery Dis 17:553-560

17 Horiguchi J, Fujioka C, Kiguchi M, et al. (2007) Soft and intermediate plaques in coronary arteries: how accurately can we measure CT attenuation using 64-MDCT? Am J Roentgenol 189:981-988

18 Suzuki S, Furui S, Kuwahara S, et al. (2006) Accuracy of attenuation measurement of vascular wall in vitro on computed tomography angiography: Effect of wall thickness, density of contrast medium, and measurement point. Invest Radiol 41:510-515

19 Kristanto W, van Ooijen P, Greuter MJ, et al. (2013) Non-calcified coronary atherosclerotic plaque visualization on CT: effects of contrast-enhancement and lipid-content fractions. Int J Cardiovasc Imaging 29:1137-1148

20 Kristanto W, van Ooijen PM, Dikkers R, et al. (2010) Quantitative image analysis for the detection of motion artefacts in coronary artery computed tomography. Int J Cardiovasc Imaging 26:77-87

21 Brodoefel H, Burgstahler C, Sabir A, et al. (2009) Coronary Plaque Quantification by Voxel Analysis: Dual-Source MDCT Angiography Versus Intravascular Sonography. Am J Roentgenol 192:84-89

22 Achenbach S, Boehmer K, Pflederer T, et al. (2010) Influence of Slice Thickness and Reconstruction Kernel on the CT Attenuation of Coronary Atherosclerotic Plaque. J Cardiovasc Comput Tomogr 4:110-115

23 Cademartiri F, La Grutta L, Runza G, et al. (2007) Influence of convolution filtering on coronary plaque attenuation values: observations in an ex vivo model of multislice computed tomography coronary angiography. Eur Radiol 17:1842-1849

24 Schroeder S, Kopp AF, Ohnesorge B, et al. (2001) Accuracy and Reliability of Quantitative Measurements in Coronary Arteries by Multi-slice Computed Tomography: Experimental and Initial Clinical Results. Clin Radiol 56:466-474

25 Kristanto W, van Ooijen PMA, Jansen-van der Weide MC, Vliegenthart R, Oudkerk M. (2013) A Meta Analysis and Hierarchical Classification of HU-Based Atherosclerotic Plaque Characterization Criteria. Plos One 8:e73460

26 Johnson TR, Krauss B, Sedlmar M, et al. (2007) Material differentiation by dual energy CT: initial experience. Eur Radiol 17:1510-1517

27 Olsen, S. and Gooch, B. (2011) Image Simplifications and Vectorization.In: NPAR' 11 Proceedings of the ACM SIGGRAPH/Eurographics Symposium on Non-Photorealistic Animation and Rendering. Spencer, S. N. (ed).New York:ACM, 201165-74

28 Zeng GL, Allred RJ. (2009) Partitioned Image Filtering for Reduction of the Gibbs Phenomenon. Journal of nuclear medicine technology 37:96-100

Part 2

Aortic Valve Measurement

Chapter 5 3D Printing and its role in cardiac valve replacement procedures

Publication: 3D printing for heart valve disease: a systematic review

Tuncay V, van Ooijen MA. European Radiology Experimental. 2019 Feb 15;3(1):9

Introduction

Although patient specific three-dimensional (3D) visualization already provides good insight in the complex anatomy of a patient, in some cases this is not sufficient and more advanced techniques are required. Novel techniques for 3D visualization of medical datasets are the use of Virtual and Augmented Reality (VR and AR) but also 3D printing could play a major role in this area [1,2]. On the one side, 3D printing allows the surgeon to hold and examine the structures printed in a tactile way, sometimes providing a better insight in the 3D anatomy. On the other side a real life-size 3D printed anatomy allows to test procedures by introducing the actual implants, wires and instruments into the printed anatomy.

The basis of 3D printing was laid in the 1980's. Medical applications arose from this new technology early on in the development mainly in maxillofacial surgery. Although one paper already reported on the use of stereolithographic printing of mitral valves based on Ultrasound imaging in patients as early as 2000 [3], the real interest for 3D printing in cardiovascular applications started some years after that.

Building on the experience of the early adopters, the past few years have seen an enormous increase of the use of 3D printing in a wide variety of medical applications. The field has demonstrated itself as an example of multidisciplinary cooperation where radiologists, surgeons, and mechanical/biomedical engineers all provide their specific expertise in the different application areas [4]. These application areas vary from the printing of anatomical models for teaching and training [5] to models to inform the patient about treatment and from pre-operative evaluation of devices to the printing of guides and implants used during surgery. In recent years, cardiac anatomy and especially congenital heart disease has become one of the focus areas of 3D printing to easily visualize and explore complex cardiovascular anatomy. However, other applications that could have major impact on the field of cardiothoracic surgery such as planning of transcatheter aortic valve replacement (TAVR) and transcatheter mitral valve replacement (TMVR) are also arising. 3D Printing could be used to tackle some of the challenges in these interventions such as patient selection, prosthesis choice and sizing, and innovation in valve design. In this narrative review, we discuss current state of the art in this area from a technical point of view by considering the constraints and possibilities of the 3D printing technique based on published work that specifically focuses on 3D printing in cardiac valve disease treatment. We will look at general

topics such as data preparation, time requirements, printer possibilities, and material properties relating to this specific application area. Possible clinical applications from literature will also be introduced.

Literature Search

A PubMed search for English publications with the terms “3D printing” AND “cardiac valve” shows that interest in this topic is certainly gaining. Although our initial search resulted in 64 items, after analysis of abstracts and text 27 remained valid and related to the review topic. From the references of these 27 papers another 7 papers were added resulting in a total of 34 papers. Of these, 5 were earlier review papers, of which most only mentioned the specific case of 3D printing in cardiac valve diseases as a small sub-section of their review. The selected papers clearly show that about a decade ago the interest in 3D printing for this application area was emerging, but only the past 2 to 3 years it really gained interest resulting in a steep increase in the number of publications (Figure 1).

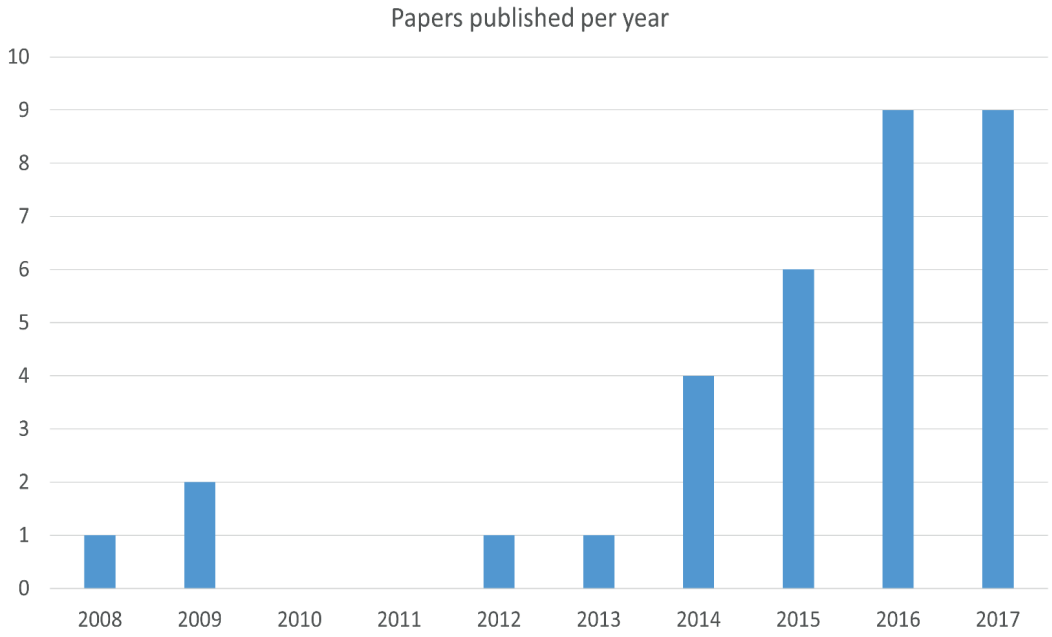

Figure 1: Number of publications on 3D printing in the application of cardiac valve assessment or replacement. Although around for about a decade, it really gained interest the past 2-3 years

Source Data and Pre-processing

To allow 3D printing a high-quality volume dataset with high resolution and no artefacts is required. Common modern radiological imaging techniques are able to acquire such data and therefore suitable for 3D printing provided that the proper reconstructions and protocols are applied. CT is the most common imaging modality providing image data for 3D printing in cardiac valve diseases (18 papers, 62%) [6-23]. It is followed by Ultrasound (8 papers, 28%) [9, 24-30], computer generated models (Computer Aided Design) (2 papers, 7%) [31,32], and MR (1 paper, 3%) [34] (Figure 2).

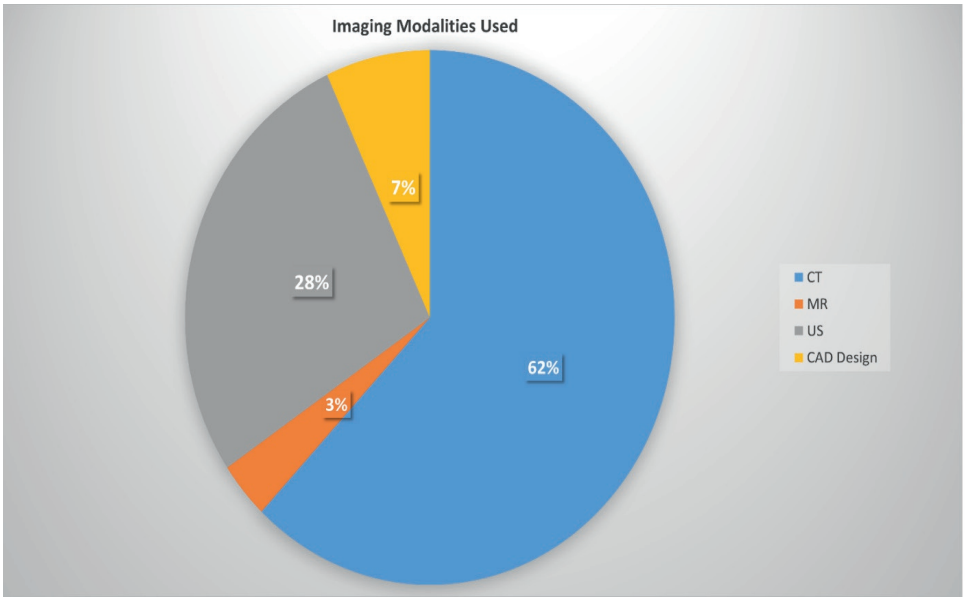

Figure 2: Frequency of use of source data.

The quality of printed models is highly depending on the quality of the imaging dataset used. Cardiac motion and breathing artefacts have a negative impact on the segmentation and thus the printed volume. Typically, high resolution scans are used in combination with electrocardiography gating, breath-hold and/or MRI respiratory gating [35]. In order to allow 3D printing of structures, they must have distinct tissue contrast in the imaging data [4].

In CT commonly 0.75 to 1mm slice thickness with a smoother kernel are used [4,6,35]. Higher resolution scans are less favorable since they introduce higher noise levels and require a more cumbersome segmentation process [35]. Some studies report the use of multiphase acquisition during

the cardiac cycle to ensure that the right phase can be reconstructed [22]. In MRI, standard cardiac imaging sequences can be used. However, the lower resolution of MR in comparison to CT can make it difficult to obtain good quality 3D prints [35]. In ultrasound the use of 3D Ultrasound is required in order to obtain a proper 3D volume for segmentation of the anatomical structures [24].

Regardless of the modality used to acquire the 3D datasets, structures of interest have to be segmented and translated into a surface model to enable 3D printing. Of this, segmentation is the key process [33]. In some cases, vessel wall is too thin to segment. In these cases, extra thickness should be added to the model since 3D printers have minimum thickness requirements [20].

The most commonly described tool for segmentation and creation of the STL file required for 3D printing is the Mimics/3-Matic software combination (Materialise, Belgium). Secondly, Solidworks is also used frequently. Less common are 3D Slicer, AutoDesk Meshmixer and the Vascular Modeling Toolkit (VMTK).

All packages used have in common that they allow to import the (DICOM) imaging data of modalities like Computed Tomography (CT), Magnetic Resonance Imaging (MRI) and Ultrasound (US) and transfer them into a 3D model. This model is realized by segmentation of the structures of interest, after which a surface representation is constructed. This surface reconstruction is commonly exported in STL format from the modelling software and loaded into the software of the 3D printer. This software allows to create and correct the model in order to ensure that it is printable and enables inclusion of required structures such as additional support material. After the model is completed, the data is resliced into print levels after which it can be sent to the printer to be manufactured.

Printing Materials

Although 3D printing has been around for quite some time already, one of the major areas of concern when printing cardiovascular structures such as the aorta, heart, and valves was the limited availability of usable printing materials to obtain objects with vessel like properties. Traditional phantoms would be constructed with rigid models of resins or glass, but these are not useful when a more life-like representation of the vessel wall is required. Therefore, the property requirements of printing materials for 3D printing of cardiovascular structures are often concerning the flexibility of the material to mimic the vessel wall [11,34] (Figure 3) and the transparent nature of the materials [11] to allow observation of instruments when inserted and to allow visual inspection of internal structures.

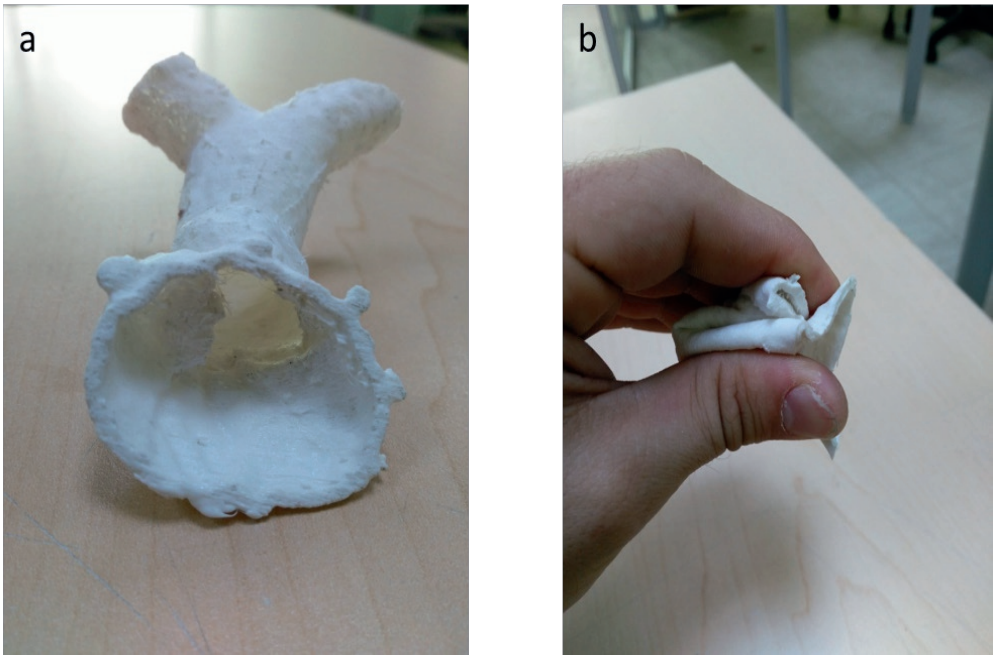

Figure 3: Example of RVOT-Main Pulmonary Artery print in flexible, non-transparent material in its normal (a) and squeezed (b) form.

Literature shows that Acrylonitrile Butadiene Styrene (ABS) and TangoPlus FullCure 930 are the most commonly used materials (Table 1). TangoPlus FullCure 930 is a commercially available translucent rubber-like polyjet photopolymer material. It can simulate different levels of hardness, elongation, and tear resistance. Because of the difficulty of direct printing in flexible materials, many papers describe a process where they print casts and molds in other materials that are then dipped in or coated with silicone to obtain flexible vessels and valves with more accurate tissue properties (e.g. [12,27]. A challenge with this method is that it must either be possible to remove the silicone from the cast or mold after hardening or the cast or mold should be printed in a dissolvable material. Few examples also exist of customized printers that directly print with (sanitary) silicone [11,31].

Table 1: 3D Printing materials for intended uses and the application areas.

Author	Intended Use	Application Area	Printing Material	Post-treatment Material
Abdel-Sayed [11]	Training	Trans-apical Aortic Valve Replacement	Silicone	Silicone Coating
Biglino [34]	Device testing	Material testing for cardiovascular application	TangoPlus FullCure 930	None
Fujita [12]	Pre-operative planning	Transcatheter Aortic Valve Implantation (TAVI)	ABS	Silicone Coating
Fujita [13]	Retrospective procedure evaluation	Transcatheter Aortic Valve Implantation (TAVI)	TangoPlus FullCure 930	Silicone Coating
Fujita [14]	Pre-operative planning	Transcatheter Aortic Valve Implantation (TAVI)	Photopolymer Resin	None
Izzo [7]	Pre-operative planning	Transcatheter Native Mitral Valve Replacement	TangoPlus FullCure 930	None
Kalejs [31]	Device testing	Aortic Valve replacement	Silicone	Silicone Coating
Maragiannis [17]	Training	Aortic Valve stenosis	TangoPlus FullCure 930	Silicone Coating
Mashari [26]	Device testing	Mitral valve models	Moldstar 15 + Ecoflex 0030	Silicone Coating
Ripley [20]	Pre-operative planning	Transcatheter Aortic Valve Implantation (TAVI)	Clear flexible resin	None
Sardari Nia [27]	Pre-operative planning	Mitral valve intervention	ABS	Silicone Coating
Vukicevic [9]	Training	Mitral valve intervention	TangoPlus FullCure 930	None
Witschey [28]	Pre-operative planning	Mitral valve intervention	ABS	None
Owais [29]	Pre-operative planning	Mitral annuli	ABS	None

An additional requirement of specific interest in the case of the cardiac valves is the ability to print with multiple types of material to obtain flexible vessel walls and valves in combination with rigid calcified plaque deposits. Successful reports have been published using a transparent and flexible material for the vessel wall and valves combined with an opaque, rigid material for the calcified plaques [4,7,9,17,19,20] (Figure 4).

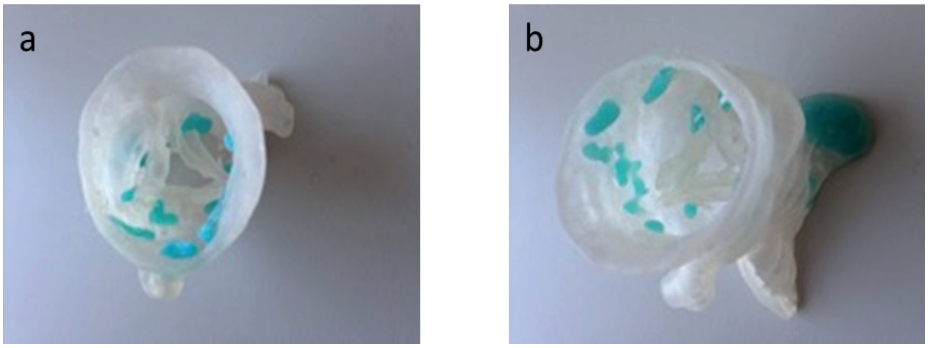

Figure 4: Example of a print of the aortic valve (a) in flexible transparent material with calcifications in blue non-flexible material (b).

For example, Vukicevic et al. [9] 3D printed patient specific mitral valves of 3 patients with multiple materials to evaluate trans-catheter mitral valve repair procedures. They did biomechanical tests on different TangoPlus materials and compared them with the mechanical properties of the porcine mitral valve tissue to select the most appropriate TangoPlus material for specific region of the 3D model. They used different TangoPlus materials on different parts of the model in order to have most realistic mechanical properties.

Printing Techniques

Several printing techniques exist of which most frequently used and well known are Fused Deposition Modeling (FDM), StereoLithography (STL), Polyjet and Laser Sintering. Details on these techniques have been described extensively in literature [4, 5, 35, 36]. Based on the review performed it is clear that STL is the preferred method for cardiac valve printing (40%), followed by FDM (30%). The preference for STL can be mainly explained by its ability to print more easily with flexible and transparent materials than other techniques.

In some cases, a dedicated setup was built to allow less conventional printing materials or printing hardware. One example setup in literature was built with a syringe filled with (sanitary) silicone that was used to print a semi-transparent, flexible aortic root [31]. Although this was a very cheap solution and printing and post processing time of the print were quite long (3h20min to 3 days) a high accuracy could be achieved (3.0% error along X and Y axis / 4.1% error along Z axis).

Time Constraints

The current printing process involves the following steps:

1) Acquisition of the data

2) Segmentation of the anatomical structures

3) Export of the segments to STL

4) Repair and improvement of the STL file

5) Reslicing and preparing for printing (e.g. definition of support materials)

6) Printing process

7) Post-printing (e.g. removal of support materials, silicone dipping, etc).

The time required to go through these steps is not mentioned in all papers and those that do mostly only provide a total processing time for steps 2-7 [11,20,24–26,30,34] (Table 2). The reported time span ranges from 30 minutes for an FDM print of the mitral annulus [24] to 3 days for a dedicated FDM printer with a syringe filled with silicone followed by silicone dip-coating for a simplified heart model [11]. Although the printing time is heavily depending on the size and complexity of the structure that is printed, experience shows that the most time-consuming steps are 6 and 7. This especially holds in the case of molds and casts where extensive post-printing treatment is required with – for example – application of the silicone (often with multiple coat dipping) and, hardening of the material. Steps 2-5 are increasingly supported by dedicated software tools allowing more automation in the process and guided workflows to ensure a proper printing model.

Table 2: Required time for different printed objects with various printing techniques.

Author	Printer	Print method	Post-treatment	Printed object	Time
Abdel-Sayed [11]	FDM Syringe with silicone	Fused Deposition Modeling	Dip-coating with silicone	Simplified heart model	3 days
Biglino [34]	PolyJet	PolyJet	None	Descending Aorta	12 hours
Kalejs [31]	Fab@Home printer	Fused Deposition Modeling	Dip-coating with silicone	Aortic Root model	3.3 hours
Mahmood [25]	Objet260 Connex	PolyJet	NA	Mitral valve	90 min
Mahmood [24]	Makerbot Replicator 2X	Fused Deposition Modeling	None	Mitral annulus	30 min
Mashari [26]	Makerbot Replicator 2X	Fused Deposition Modeling	Silicone casting	Mitral valve	2-5 hours
Muraru [30]	Formiga P110	Laser Sintering	NA	Tricuspid Valve	90-120 min
Ripley [20]	Form 1 Plus	Stereolithography	NA	Aortic Root	5 hours
Owais [29]	Makerbot Replicator 2X	Fused Deposition Modeling	None	Aortic annulus	15 min

FDM: fused deposition modeling, SLT: stereolithography, NA: not applicable

In general, required time for the whole process of segmentation, data cleaning and preparation and the printing itself varies a lot depending on the size of the printed object, the printing technique used and the requirement for post-printing treatment.

Possible Printing Issues

One of the issues with 3D printing is the accuracy of the 3D printed object in size and shape. The difference between the 3D printed object and imaging modality measurements should be minimal. Using current printers and software the print accuracy is high with reported accuracies of a mean difference between measurement in CT and of the print of -0.34mm +/- 1.3mm [20] and 0.7mm +/- 0.3mm [30]. No significant differences between CT measurement and actual print measurement were found [30]. Therefore, with careful design of the printing process it is possible to print models that resemble real anatomy and can be used for pre-operative planning.

Another issue is the removal of the support materials. Different from most other 3D printed models, the vascular models are complex in structure and must be hollow in order to gain access to the lumen with wires and devices. This can be achieved by either choosing a printing strategy not requiring support

material (such as binder jetting) or by removing the support material after printing. A soluble support material can be used in a multiple material printer. In that case the object usually has to be submerged into, for example, water to dissolve the support material [7]. When printing using a method where the same printing material is used for both object and support, the challenge is to fully remove all of the support material from the printed object manually. In vascular models this can be quite challenging and complete removal of internal supports inside the artery structure can be difficult to obtain. Printing with supports also requires careful placement of the structure on the printing bed to minimize the negative effect of the support structures since support required will be different with orientation of the object (Figure 5).

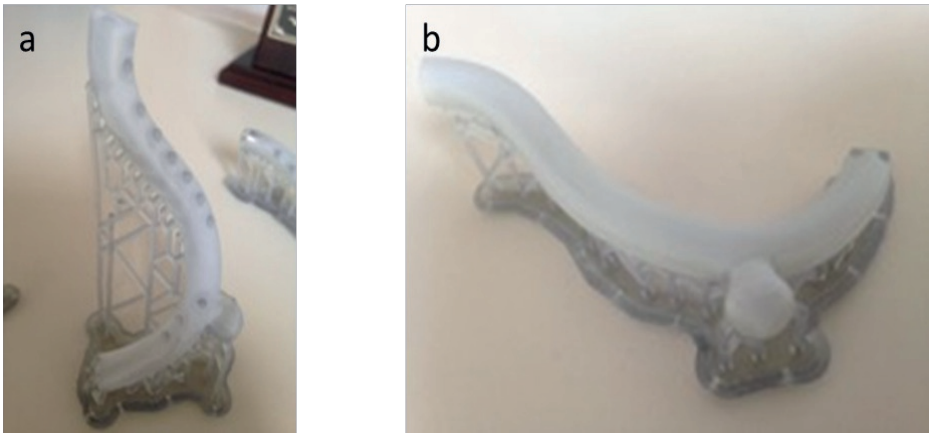

Figure 5: Example of a vessel print with support structures. When the vessel is printed in the anatomically correct orientation (a) it is running perpendicular to the printing surface and thus a lot of support material is required. When re-oriented and printed parallel to the printing surface (b) less support is required.

Clinical Application - Training models

TAVR is a relatively new and fast growing therapeutic approach. Skills required to perform this kind of procedures are difficult to obtain and a steep learning curve is perceived. Traditional training methods would require using animal models. This is costly and is gaining resistance by animal well-being

organizations because of ethical considerations. Moreover, the logistics surrounding the use of animals or animal materials is rather cumbersome and complicated. A viable alternative can be found in an artificial heart model. However, this has a downside that the variation in anatomy is limited and it often involves high manufacturing costs. 3D printing could solve this by providing an easy and relatively inexpensive method to obtain a wide variation of training samples that can be easily produced and replaced.

The training models vary from simplified heart models [11] or geometrically designed aortic roots [31] to advanced flow models using pulsatile pumps allowing a more real-life simulation [5, 17] where devices can be introduced and deployed under lifelike conditions (Figure 6). One study described the printing of a MR compatible setup to allow scanning of mitral valves of pigs in the natural state [32]. They achieved this by designing and 3D printing valve specific mounting materials based on pre-mortem Ultrasound intra-valve measurements.

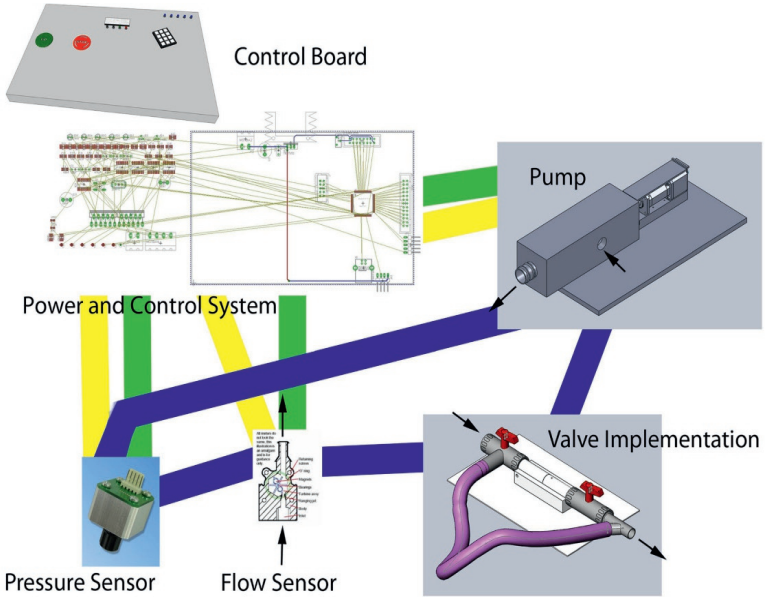

Figure 6: Sample schematic setup of an experimental environment to test valves. The 3D printed valve would be included in the Valve Implementation part inside the flow loop (blue lines).

Clinical Application - Pre-operative Planning

As stated before, recent years have shown an increase in minimal invasive cardiac surgery with the advent of procedures like TAVR. One clear advantage of 3D printing is its utilization in pre-operative

planning of such complex (minimally invasive) cardiac surgery. Subsequently, the largest subgroup of the non-review papers (63%) concerns the use of 3D printing for pre-operative planning. Of these, the division between mitral and aortic valve replacement is about 50/50.

When performing pre-operative planning of TAVR, the printed anatomy ranges from only the Aortic annulus [19,20] or aortic arch/aorta [15,21,22] to more complex anatomical configurations with different anatomical structures in one print including outflow tracts and heart chambers [12-14]. One study even not only used 3D printed anatomy of the aorta but also 3D printed stent models [16].

The most crucial information for TAVR planning is the prediction of paravalvular aortic regurgitation (PAR). In one of the reported studies the authors demonstrate the use of elastic 3D printed model in the prediction of PAR. PAR prediction was done by using a light transmission test. The prosthesis was inserted into the 3D printed model and the PAR was predicted based on projection of light through the left ventricular outflow tract onto a thin film and captured with a digital camera. This correctly predicted PAR in 6 out of 9 patients and absence of PAR in 5 out of 7 patients [20].

Clinical Application - Device testing

Device testing and development is also an important application of 3D printing. Biglino et al. 3D printed models of the descending aorta with same lumen dimension but different wall thicknesses and did compliance tests [34]. They used the distensibility knowledge to build a right ventricular outflow tract model, which was used to simulate the pulmonary valve replacement procedure for device testing [34]. Kalejs et al. manufactured real life size artic root model for testing valved stents [31]. Mashari et al. created a 3D model of the mitral valve from 3D US images of a patient who underwent percutaneous MitraClip operation. MitraClip operation is a minimally invasive procedure to reduce the mitral regurgitation. The model was then deployed in the pulse-duplicator chamber filled with a blood-mimicking fluid for hemodynamic testing [26].

Discussion

Novel techniques like 3D printing are investigated by different research groups for specific clinical questions and they all explore the technical requirements and shortcomings of the technique. While the topic is current, the actual clinical benefit of 3D printing yet remains to be proven. However, technical developments are ongoing and the implementation of 3D printing for cardiac valve treatment is one of the more promising clinical application areas. However, the application of 3D printing in cardiac valve

replacement introduces additional requirements when printing concerning the material used and the nature of the printed structure. This review shows that with the advent of new – flexible and transparent – materials and higher accuracy of 3D printers, an accurate representation of the cardiac anatomy can be obtained. This 3D printed representation of the anatomy can already be used in a variety of applications and especially for training purposes.

It has been shown that for accurate 3D Printing of anatomy or pathology, correct segmentation is of vital importance and although some of the segmentation work is currently automated, the input of experts is still needed for validation and correction. Any small mistake in the segmentation process could lead to erroneous prints. This could lead to failure of the printing process itself, but also in a 3D printed structure that is not accurate and therefore could be harmful to the patient when used for pre-operative planning. The segmentation step should therefore be conducted and/or supervised by an expert in the anatomy being segmented and quality control of the source data should be in place. Also, the segmentation tools should be validated and approved for clinical use. Although the majority of the reviewed papers show the use of a validated commercial software tool, may still rely on freeware and open-source software which could hamper reliability of the segmentation, 3D model construction and thus the printing result. In this review, we aimed to explore the options, challenges, and possibilities of the 3D printing in the field of cardiac valve replacement in order to give an insight in the current state of the art and development in this specific area of 3D printing. The low number of papers found on this topic demonstrates its experimental nature. However, the papers published do show the progress made in the past years allowing clinical application. This clinical application is currently mainly in training and education but the literature also shows promise for actual patient specific clinical applications of 3D printed models.

Conclusion

Current technology allows accurate printing of cardiac anatomy in materials that resemble the properties of the actual heart and vessels. The application of 3D printing in valve replacement planning could therefore provide new insights in many different ways for the different ‘stakeholders’ [33]. It can provide better insight in the anatomy and allow pre-operative training for the treating physician [5]. For the patient, it can provide more insight in the disease and treatment options [4,35]. For the manufacturer, it allows easier pre-clinical testing of new devices or instruments. Finally, for the educator it can provide a wide variety of anatomical and pathological examples that would normally be unavailable.

References

1. Sutherland J, Belec J, Sheikh A et al (2018) Applying Modern Virtual and Augmented Reality Technologies to Medical Images and Models. J Digit Imaging [Epub ahead of print]

2. Mitsouras D, Liacouras P, Imanzadeh A et al (2015) Medical 3D Printing for the Radiologist. Radiographics 35(5):1965-1988.

3. Binder TM, Moertl D, Mundigler G et al (2000) Stereolithographic Biomodeling to create tangible hard copies of cardiac structures from echocardiographic data. JACC 35(1):230-237.

4. Giannopoulos AA, Steigner ML, George E et al (2016) Cardiothoracic Applications of 3-dimensional Printing. J Thorac Imaging Sep;31(5):253-72.

5. Vukicevic M, Mosadegh B, Min JK et al (2017) Cardiac 3D Printing and its Future Directions. JACC Cardiovasc Imaging Feb;10(2):171-184.

6. Dankowski R, Baszko A, Sutherland M et al (2014) 3D heart model printing for preparation of percutaneous structural interventions: description of the technology and case report. Kardiologia Polska 72(6):546-551.

7. Izzo RL, O'Hara RP, Iyer V et al (2016) 3D Printed Cardiac Phantom for Procedural Planning of a Transcatheter Native Mitral Valve Replacement. Proc SPIE Int Soc Opt Eng, Feb 27;9789.

8. Little SH, Vukicevic M, Avenatti E et al (2016) 3D Printed Modeling for Patient-Specific Mitral Valve Intervention: Repair With a Clip and a Plug. JACC Cardiovasc Interv 9(9):973-5.

9. Vukicevic M, Puperi DS, Jane Grande-Allen K et al (2017) 3D Printed Modeling of the Mitral Valve for Catheter-Based Structural Interventions. Ann Biomed Eng 45(2):508-519.

10. Wang DD, Eng M, Greenbaum A et al (2016) Predicting LVOT Obstruction After TMVR. JACC Cardiovasc Imaging 9(11):1349-1352.

11. Abdel-Sayed P, Kalejs M, von Segesser LK (2009) A new training set-up for trans-apical aortic valve replacement. Interact Cardiovasc Thorac Surg 8(6):599-601.

12. Fujita B, Kütting M, Scholtz S et al (2015) Development of an algorithm to plan and simulate a new interventional procedure. Interact Cardiovasc Thorac Surg 21(1):87-95.

13. Fujita B, Kütting M, Seiffert M et al (2016) Calcium distribution patterns of the aortic valve as a risk factor for the need of permanent pacemaker implantation after transcatheter aortic valve implantation. Eur Heart J Cardiovasc Imaging 17(12):1385-1393.

14. Fujita T, Saito N, Minakata K et al (2017) Transfemoral transcatheter aortic valve implantation in the presence of a mechanical mitral valve prosthesis using a dedicated TAVI guidewire: utility of a patient-specific three-dimensional heart model. Cardiovasc Interv Ther 32(3):308-311.

15. Gallo M, D'Onofrio A, Tarantini G et al (2016) 3D-printing model for complex aortic transcatheter valve treatment.Int J Cardiol 210:139-40.

16. Hernández-Enríquez M, Brugaletta S, Andreu D et al (2017) Three-dimensional printing of an aortic model for transcatheter aortic valve implantation: possible clinical applications. Int J Cardiovasc Imaging 33(2):283-285.

17. Maragiannis D, Jackson MS, Igo SR et al (2015) Replicating Patient-Specific Severe Aortic Valve Stenosis With Functional 3D Modeling. Circ Cardiovasc Imaging 8(10):e003626.

18. O'Neill B, Wang DD, Pantelic M et al (2015) Transcatheter caval valve implantation using multimodality imaging: roles of TEE, CT, and 3D printing. JACC Cardiovasc Imaging 8(2):221-5.

19. Qian Z, Wang K, Liu S et al (2017) Quantitative Prediction of Paravalvular Leak in Transcatheter Aortic Valve Replacement Based on Tissue-Mimicking 3D Printing. JACC Cardiovasc Imaging 10(7):719-731.

20. Ripley B, Kelil T, Cheezum MK et al (2016) 3D printing based on cardiac CT assists anatomic visualization prior to transcatheter aortic valve replacement. J Cardiovasc Comput Tomogr 10(1):28-36.

21. Schmauss D, Schmitz C, Bigdeli AK et al (2012) Three-dimensional printing of models for preoperative planning and simulation of transcatheter valve replacement. Ann Thorac Surg 93(2):e31-3.

22. Schmauss D, Haeberle S, Hagl C et al (2015) Three-dimensional printing in cardiac surgery and interventional cardiology: a single-centre experience. European Journal of Cardio-Thoracic Surgery 47:1044-1052.

23. Sodian R, Schmauss D, Markert M et al (2008) Three-dimensional printing creates models for surgical planning of aortic valve replacement after previous coronary bypass grafting. Ann Thorac Surg 85(6):2105-8.

24. Mahmood F, Owais K, Montealegre-Gallegos M et al (2014) Echocardiography derived three-dimensional printing of normal and abnormal mitral annuli. Ann Card Anaesth 17(4):279-83.

25. Mahmood F, Owais K, Taylor C et al (2015) Three-dimensional printing of mitral valve using Echocardiographic data. JACC: Cardiovascular Imaging 8(2):227-229.

26. Mashari A, Knio Z, Jeganathan J et al (2016) Hemodynamic Testing of Patient-Specific Mitral Valves Using a Pulse Duplicator: A Clinical Application of Three-Dimensional Printing. J Cardiothorac Vasc Anesth. 30(5):1278-85.

27. Sardari Nia P, Heuts S, Daemen J et al (2017) Preoperative planning with three-dimensional reconstruction of patient's anatomy, rapid prototyping and simulation for endoscopic mitral valve repair. Interact Cardiovasc Thorac Surg 24(2):163-168.

28. Witschey WR, Pouch AM, McGarvey JR et al (2014) Three-dimensional ultrasound-derived physical mitral valve modeling. Ann Thorac Surg 98(2):691-4

29. Owais K, Pal A, Matyal R et al (2014) Three-Dimensional printing of the mitral annulus using echocardiographic data: science fiction or in the operating room next door? Journal of Cardiothoracic and Vascular Anesthesia 28(5):1393-1396.

30. Muraru D, Veronesi F, Maddalozzo A et al (2017) 3D printing of normal and pathologic tricuspid valves from transthoracic 3D echocardiography data sets. Eur Heart J Cardiovasc Imaging 18(7):802-808.

31. Kalejs M, von Segesser LK (2009) Rapid prototyping of compliant human aortic roots for assessment of valved stents. Interactive Cardiovascular and Thoracic Surgery 8:182-186.

32. Stephens SE, Liachenko S, Ingels NB et al (2017) High resolution imaging of the mitral valve in the natural state with 7 Tesla MRI. PLoS One Aug 30;12(8):e0184042.

33. Vaquerizo B, Theriault-Lauzier P, Piazza N (2015) Percutaneous Transcatheter Mitral Valve Replacement: Patient-specific Three-dimensional Computer-based Heart Model and Prototyping. Rev Esp Cardiol (Engl Ed) 68(12):1165-73.

34. Biglino G, Verschueren P, Zegels R et al (2013) Rapid prototyping compliant arterial phantoms for in-vitro studies and device testing. J Cardiovasc Magn Reson 15:2.

35. Giannopoulos AA, Mitsouras D, Yoo S-J et al (2016) Applications of 3D printing in cardiovascular diseases. Nature Reviews Cardiology 13:701-718

36. Meier LM, Meineri M, Qua Hiansen J et al (2017) Structural and congenital heart disease interventions: the role of three-dimensional printing. Neth Heart J. 25(2):65-75.

Chapter 6 Design, Implementation and Validation of a Pulsatile Heart Phantom Pump.

Publication: Design, Implementation and Validation of a Pulsatile Heart Phantom Pump.

Tuncay V, Zijlstra J, van Ooijen PMA

Journal of Digital Imaging (Accepted for publication)

Conference paper: Heart phantom for the flow measurement through heart valves

Tuncay V ECR 2013, http://dx.doi.org/10.1594/ecr2013/C-2196

Introduction

The advent of new and improved scanning algorithms for both Computed Tomography (CT) and Magnetic Resonance Imaging (MRI) combined with their increased temporal resolution have facilitated the ability to measure and visualize blood flow and perfusion in vivo using these techniques[1,2]. However, accurate validation is needed to determine the gold standard. Phantoms are commonly used for the validation purposes [3,4]. For proper validation and calibration, a controllable system is required which mimics the dynamic pumping function of the heart.

Phantoms are developed using different kinds of pumps to mimic the blood flow[5-7]. However, the type of pump used has major impact on its applicability. Laminar flow pumps do not generate a pulsatile flow, which is needed to mimic the blood flow through the cardiovascular system [8,9]. When pulsatile flow is needed, most of the time commercial pulsatile pumps are used [7,10,11].

In this study, we aimed to develop an affordable pulsatile pump and a mock circulatory system in order to simulate the blood flow for validation tests and other development purposes such as image processing and medical device testing. The prerequisites for an ideal phantom are identified as:

1) controllable pulsating flow output equal to the human pulse pattern,

2) The flow pattern of the mimicked cardiac output should be equal to that of a human,

3) Stroke volume variable between 40 and 120ml/beat,

4)Heart rate variable between 60 and 170 BPM.

The developed phantom was tested with a CT scanner.

The Setup

The main components of the phantom setup are the measurement box, the pump, the control box, pressure and flow sensors. These components are connected together using tubing (Figure 1). The phantom pump should create a pulsatile flow through the measurement box. The measurement box has an in- and outflow and can contain different vessel/valve configurations or other phantoms. The measurement box is the part of the phantom setup that will be placed inside the bore of the CT or MRI

and thus should not contain any ferro-magnetic parts. Pump and measurement system should allow use of blood as liquid as well.

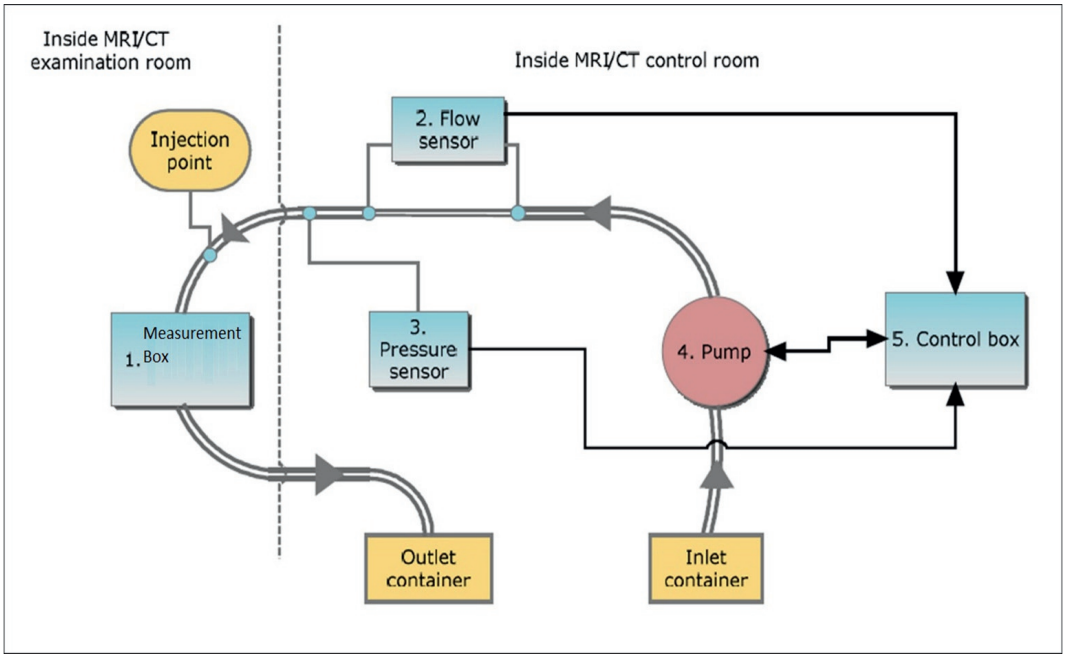

Figure 1: Flowchart for the pulsatile heart phantom.

The pump

The pump is a piston pump using a linear actuator (L4118L1804-T5X5A50, Nano-tec) to drive the piston inside a cylindrical chamber. The linear actuator has a fixed step size of 0.025mm. The movement of the actuator will result in a pulsatile, one-directional flow, by placing one-way valves at the inlet and outlet (Figure 2).

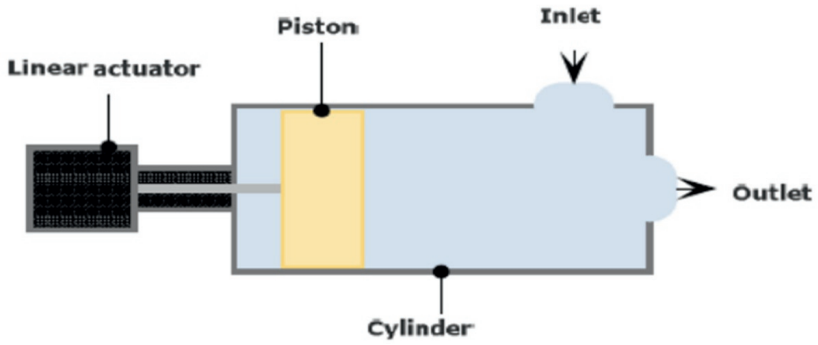

Figure 2: The pulsatile pump.

The cylinder is from one block of aluminum with a cavity diameter of 59.9mm and a length of 101.0 mm resulting in a maximum volume of the cylinder of 284.6 ml. Because of the size of the piston, the limitations of the length of the axis of the actuator and the general construction of the pump, the actual working maximum stroke volume of the pump is 110ml.

The speed of the piston is dependent on the heart rate, stroke volume and flow pattern set using the control panel. The volume/step is constant at 0,0704ml, which defines the amount of volume displaced with one-step movement of the linear actuator. Using the settings and this constant, the speed of the linear actuator (V) is determined using the following formula:

V[mm/sec]=((Stroke Volume[ml])/(Volume/step[ml])*0.025)/(60/(Heart Rate[bpm])*1/2)

The Control Box

The control box houses all the electronic parts, such as the microcontroller for controlling the system and an interface for operating the system. The micro controller (Atmel, AVR 32 Bits AT32UC3C1512) connects all the parts of the hardware and ensures the proper operation of the setup.

A rotary encoder is used to navigate through the menu of the control box. This rotary encoder allows selection by rotation and acknowledgement of a choice by pushing on the rotary encoder. The pump is activated by a start button. The stop button is a locking button, so once pressed it needs to be released by pressing on it again to activate the pump again. This prevents the rapid start and stop of the pump, which might lead to damaging the pump. Unauthorized usage is prevented by integration of a key switch. Feedback to the user is provided by a four line, twenty characters, Liquid Crystal Display (LCD). This display always provides the state of the system on the first line (e.g. start the pump or change heart rate

setting). The second and third line shows additional information, such as selected heart rate or values acquired from the sensors. The fourth line shows the possible action (e.g. menu scroll by '<' and '>'). When a variable is surrounded with '<' and '>' the value of the variable can be adjusted by turning the rotary encoder.

The correct operation of the stepper motor is checked using position feedback with a 10-turn potentiometer on the axis of the stepper motor. This suffices since the motor axis rotates a maximum of 9.5 turns to fully expand. By measuring the voltage of the potentiometer, the exact position of the piston can be derived. This feedback will not be used to create a feedback loop to adjust the cardiac output. But it can be used to monitor if the piston is stuck or that the piston is not attached to the axle any more. It is also convenient to use during development of controlling the pump.

The trigger pulse used for synchronizing the pump action with the acquisition of the CT or MR scanner is a logic signal between 0.0 and 5.0 VDC. The frequency of the pulse should be equal to the set heart rate. When the pulse is logic low the pump is filled with liquid, which represents the diastolic phase. When the logic level of the pulse is high the liquid is pumped out, which represents the systolic phase. The transition from a low level to a high level, rising edge indicates the beginning of the QRS complex.

The hardware of the trigger consist of an op-amp configured as differentiator and comparator. The trigger circuit uses the signal from the position sensor. When this signal rises the liquid is pumped out and while the signal falls liquid sucked in to the pump. The signal from the position feedback is connected to the differentiator is used to create a pulse. Since the amplitude of the block signal is not between 0.0 and 5.0VDC, a comparator is used.

Software Design

The program is designed with a main loop or a menu structure. In this loop it is possible to switch between states by rotating the rotary encoder and select the desired state through pushing on the rotary encoder. Each of the states in the menu allows the user to control the functions of the system. For error handling every state refers to the error state in case of error. The error state disables the pump and let the user know what kind of error took place such as turned off key switch voltage drop below the required value.

When the system starts up, the program starts with state zero. In this state all the settings are configured and the condition of the system is tested. If there are no problems the program advances to state one. In

state one it is possible to start the pump with the start button. The state is changed in to state five and the pump is initialized for correct functioning before the pumping sequence starts. During the pumping action, the sensors sample and send the acquired data to a computer. This communication is done via a USB connection. User needs to press on the stop button in order to leave the state and to stop the pumping action. Then the system goes back to the first state.

When the program is back in the main loop, it is possible to change the heart rate and stroke volume. The desired state needs to be selected by turning the rotary encoder. When the display shows the desired state it can be selected by pushing on the rotary encoder. Then the set value can be adjusted again by rotating the rotary encoder and it can be saved by pushing on the rotary encoder. The options state allows the user to read the values of the sensor without the pumping action.

Validation Test

The phantom setup was tested with a CT scanner in order to validate the pulsatile heart phantom (PHP) (Figure 3). During the test, water was continuously pumped through the tubes with a heart rate of 70bpm and a stroke volume of 68ml. Approximately 20cm before the measurement box, contrast liquid was pumped in the tubing. A section of the tubing is scanned with the CT to create the intensity profile of the washout. The 3D image and the washout profile are given in Figure 4. The test was successful for the given heart rate and stroke volume. It showed that designed pump can create pulsatile flow and the PHP can be used to simulate the blood circulation in the circulatory system. However, the goal of adjusting the heart rate and the stroke volume could not be achieved. It was caused by the software of the microcontroller.

Figure 3: The testing with Computed Tomography

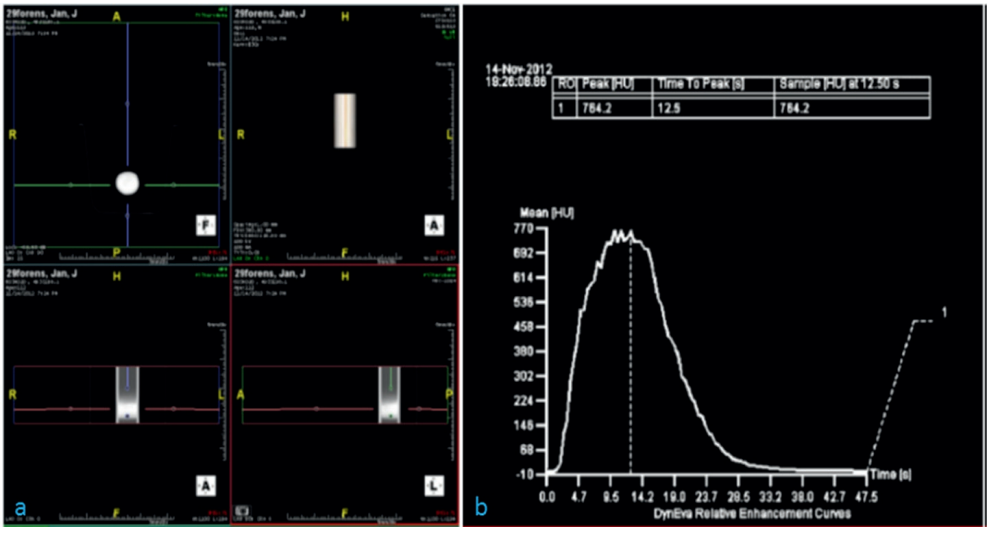

Figure 4: Result of the test with Computed Tomography. The 3D image of the scanned section of tubing (a) and the washout profile (b).

Discussion

The developed pump for the PHP can create pulsatile flow and the PHP can be used to mimic the blood circulation. The pump was connected via tubes to the measurement box, which is placed in the gantry of the scanner. In the measurement box, various types of medical devices such as heart valves or stents can be placed to conduct quality or development tests.

A preliminary test was done to test the principle of the PHP system. It was possible to validate the measured flow in the CT to the manually measured flow rate in the PHP. Quite some improvements of the PHP came up during the test. The two most important modifications were the setup of the flow sensor and the driver, which controls the pump.

The issue with the setup of the flow sensor was that it was located in a shunt tube. The shunt tube had a high resistance therefore; hardly any liquid flowed through the shunt tube. To solve this issue, a differential pressure sensor can be used to measure the pressure over a shunt tube with fixed hydraulic resistance. The flow can be derived from the measured pressure drop. A pressure sensor is used because the response time of the flow sensor was too slow to measure the flow pattern accurately as function of time

The issue with the driver was that the signal required for the driver was created by the microcontroller. In the same time, the microcontroller had to drive the pump simultaneously. This resulted in wrong values and incorrect driver signals. To solve this issue a separate microcontroller can be used to drive the pump independent from the main microcontroller.

Conclusion

A principle of proof is given for a heart phantom pump to adjust and measure dynamic flow as a validation tool for flow measurement in MRI and CT. This is confirmed with a test in a CT. However, a significant a number of improvements should be incorporated to let the PHP operate as initially specified. With these improvements, the PHP will be a challenging tool for validation of flow in imaging modalities and might offer opportunities in other disciplines as well (i.e. source for artificial circulation systems).

References

1 Krishnan P, Murphy A, Aviv RI (2017) CT-based Techniques for Brain Perfusion. Top Magn Reson Imaging 26:113-119

2 Jahng GH, Li KL, Ostergaard L, Calamante F (2014) Perfusion magnetic resonance imaging: a comprehensive update on principles and techniques. Korean J Radiol 15:554-577

3 Yue Y, Fan Z, Yang W et al (2015) Geometric validation of self-gating k-space-sorted 4D-MRI vs 4D-CT using a respiratory motion phantom. Med Phys 42:5787-5797

4 Markenroth Bloch K, Toger J, Stahlberg F (2017) Investigation of cerebrospinal fluid flow in the cerebral aqueduct using high-resolution phase contrast measurements at 7T MRI. Acta Radiol. 10.1177/0284185117740762:284185117740762

5 Okrasinski SJ, Ramachandran B, Konofagou EE (2012) Assessment of myocardial elastography performance in phantoms under combined physiologic motion configurations with preliminary in vivo feasibility. Phys Med Biol 57:5633-5650

6 Fortune S, Jansen MA, Anderson T et al (2012) Development and characterization of rodent cardiac phantoms: comparison with in vivo cardiac imaging. Magn Reson Imaging 30:1186-1191

7 Knoops PGM, Biglino G, Hughes AD et al (2017) A Mock Circulatory System Incorporating a Compliant 3D-Printed Anatomical Model to Investigate Pulmonary Hemodynamics. Artif Organs 41:637-646

8 Blake JR, Easson WJ, Hoskins PR (2009) A dual-phantom system for validation of velocity measurements in stenosis models under steady flow. Ultrasound Med Biol 35:1510-1524

9 Grice JV, Pickens DR, Price RR (2016) Technical Note: A new phantom design for routine testing of Doppler ultrasound. Med Phys 43:4431

10 Ziemer BP, Hubbard L, Lipinski J, Molloi S (2015) Dynamic CT perfusion measurement in a cardiac phantom. Int J Cardiovasc Imaging 31:1451-1459

11 Caruso D, Eid M, Schoepf UJ et al (2017) Optimizing Contrast Media Injection Protocols in Computed Tomography Angiography at Different Tube Voltages: Evaluation in a Circulation Phantom. J Comput Assist Tomogr 41:804-810

Chapter 7 Semi-Automatic, quantitative, measurement of the calcified and non-calcified Aortic Valve Area using CTA: Validation and Comparison with Transthoracic Echocardiography.

Publication: Semi-Automatic, quantitative, measurement of the calcified and non-calcified Aortic Valve Area using CTA: Validation and Comparison with Transthoracic Echocardiography.

Tuncay V, Prakken N, van Ooijen PM, Budde RP, Leiner T, Oudkerk M.

BioMed Research International 2015:648283.

Conference paper: Semi-Automatic, quantitative, measurement of the calcified and non-calcified Aortic valve area using CTA.

Tuncay V, van Ooijen P, Oudkerk M.

International Journal of Computer Assisted Radiology and Surgery 2013(suppl.1);8:S29-S30.

Introduction

Aortic stenosis (AS) is the most common valvular heart disease in the developed countries, affecting 3 percent of the population older than 65 years. It causes higher morbidity and mortality than any other cardiac valve disease [1]. AS is defined as narrowing of the aortic valve opening, which reduces blood flow from the heart into the aorta. The normal size of the aortic valve area (AVA) at maximum opening of the valve is 3 to 4 cm^2 [2]. When the AVA decreases below 1 cm^2, AS is considered to be severe [3]. For severe AS, valve replacement is the only effective treatment. However, a sizeable fraction of patients are at high risk for postoperative mortality and may refuse surgery or cannot undergo surgery due to comorbidity [4]. Recently, transcatheter aortic valve replacement (TAVR) techniques have been developed to provide less invasive treatment for those patients[5-11]. In management of AS, the timing for surgical treatment is very important. Late treatment may lead to an increase in the trans-aortic pressure gradient, myocardial pressure overload and eventually to left ventricular (LV) hypertrophy and increased LV wall thickness [12]. Visualization of the AVA is used to determine the threshold for invasive treatment and to obtain preoperative information about the aortic dimensions and proximity to other important structures such as the coronary arteries.

Different imaging modalities have been used and compared for measuring the AVA[13-23]. Initially, catheterization was the standard method for evaluating AVA, but in time its usage decreased due to its being an invasive modality and technical limitations. Alternatively, the 2D echocardiographic continuity equation, which currently is the most common tool to derive the AVA, was used to measure the AVA. However, this technique underestimates AVA since it assumes that the left ventricular outflow tract (LVOT) has circular geometry, and that flow through the LVOT is laminar and uniform [24, 25]. Bruder et al. showed a strong correlation between the AVA determined by echocardiography and MRI [20] indicating that MRI can also be used to determine AVA. However, MRI is contra-indicated for patients with metal implants or claustrophobia. Moreover, MRI has lower spatial resolution in comparison to CT [12]. More recently, development of ECG-gated Multi Detector Computed Tomography (MDCT) has led to further improvements in cardiac imaging [21], and CT is now regarded as a reliable method to measure the AVA [26]. The latest developments in dual source and 320-slice CT enable high temporal resolution acquisition and obtain sufficient image quality at high spatial resolution in almost every patient throughout the cardiac cycle. However, streaking and blooming artifacts due to heavy

calcification of the aortic valve leaflets or the aortic root that hamper visualization and analysis of the AVA can still occur.

Delgado et al. suggested that 3D planimetric measurement of the AVA by MDCT images might provide more reliable information on the assessment of AVA in comparison with echocardiography [27]. However, planimetric measurement of AVA is currently performed manually by the radiologist using standard 3D visualization and measurement software, which is time consuming and introduces user dependence and intra- and inter-observer variability [28].

The aim of this study was to develop and validate a (semi) automatic segmentation technique of the AVA and to compare manual and semi-automatic measurements with the Transthoracic Echocardiography (TTE) results. Our goal is to reduce the user dependency, time spent on measurements, and to enable reproducible and accurate measurement of AVA on MDCT datasets.

Materials and Methods

Experimental Design

In this study multiphase CT scans of 25 patients (15 female, mean age 82.84 ±5.16 years) were used. All of the patients had moderate to severe aortic stenosis and underwent TAVI at a tertiary referral center. All subjects underwent CT scanning and TTE.

Informed consent requirement was waived by the local IRB because of the retrospective nature of this study without additional burden to the patients involved.

The maximum aortic valve opening phase was selected visually for all patients. A stack of reformations was obtained after centering the axis of the multiplanar reconstruction (MPR) at the level of aortic valve and then changing the orientation of the plane perpendicular to the LVOT. The pre-selected slices were segmented both manually and semi-automatically by two independent observers 1, a biomedical engineer with more than 5 years experience and 2, a cardiac radiologist with almost 10 years medical imaging experience. Observer 1 repeated the measurement 1 day after in order to determine intra-observer variability. Manual and semi-automatic measurements were compared with the current reference standard Trans Thoracic Echocardiography (TTE) with regard to AVA. Time spent for measurements was recorded for manual and semi-automatic segmentations.

Transthoracic Echocardiography

TTE was performed as part of the routine work-up of the patient. TTE derived AVA measurements were obtained from the clinical patient records. The velocity in the left ventricular outflow tract and at the level of the aortic valve as well as the LVOT diameter were measured. From these measurements, the AVA was calculated using the continuity equation.

Multi Slice Computed Tomography

Image acquisition of the retrospectively ECG-gated CTA of the thoracoabdominal aorta was performed on a multidetector 256-slice CT (Brilliance iCT, Philips Healthcare, Best, The Netherlands). An ECG trace was recorded during the procedure. The region of acquisition ranged from above the aortic arch to the groin. Based on a locator image, a circular region of interest was drawn within the descending aorta. Non-ionic iodinated contrast material (Ultravist, 300 mg iopromide per mL, Schering Nederland BV, Weesp, The Netherlands) was injected intravenously. As soon as the descending aorta reached a density of 125 Hounsfield units (HU) within the region of interest, the patient was instructed to maintain a breath hold. Seven seconds later, image acquisition started in a craniocaudal direction with concurrent ECG trace recording. The following parameters were used: detector collimation 128 × 0.625 mm; pitch 0.30; matrix size 512 × 512. Tube voltage and tube current–time product depended on the patient's weight and were 100 kVp and 300 mAs, respectively for patients <70 kg, and 120 kVp and 250 mAs, respectively for patients ≥70 kg.

AVA Segmentation Algorithm

The segmentation algorithm (Figure 1) starts with the detection of the Sinus of Valsalva (SOV) on the MPR image. Once the SOV is detected, the region covering the SOV is cropped from the whole image (Figure 1a). The cropped image (Figure 1b) is binarized by adaptive thresholding (Figure 1c). The user places seed points (Figure 1d) to create an initial contour (Figure 1e) covering the aortic valve opening. The contour moves towards the edge of the aortic valve opening automatically (Figure 1f). The contour covers the pixels from the edge of the opening area and also the AVA opening area. The pixels of the opening area are selected and the number of pixels is multiplied by the pixel size to determine the AV opening area (Figure 1g).

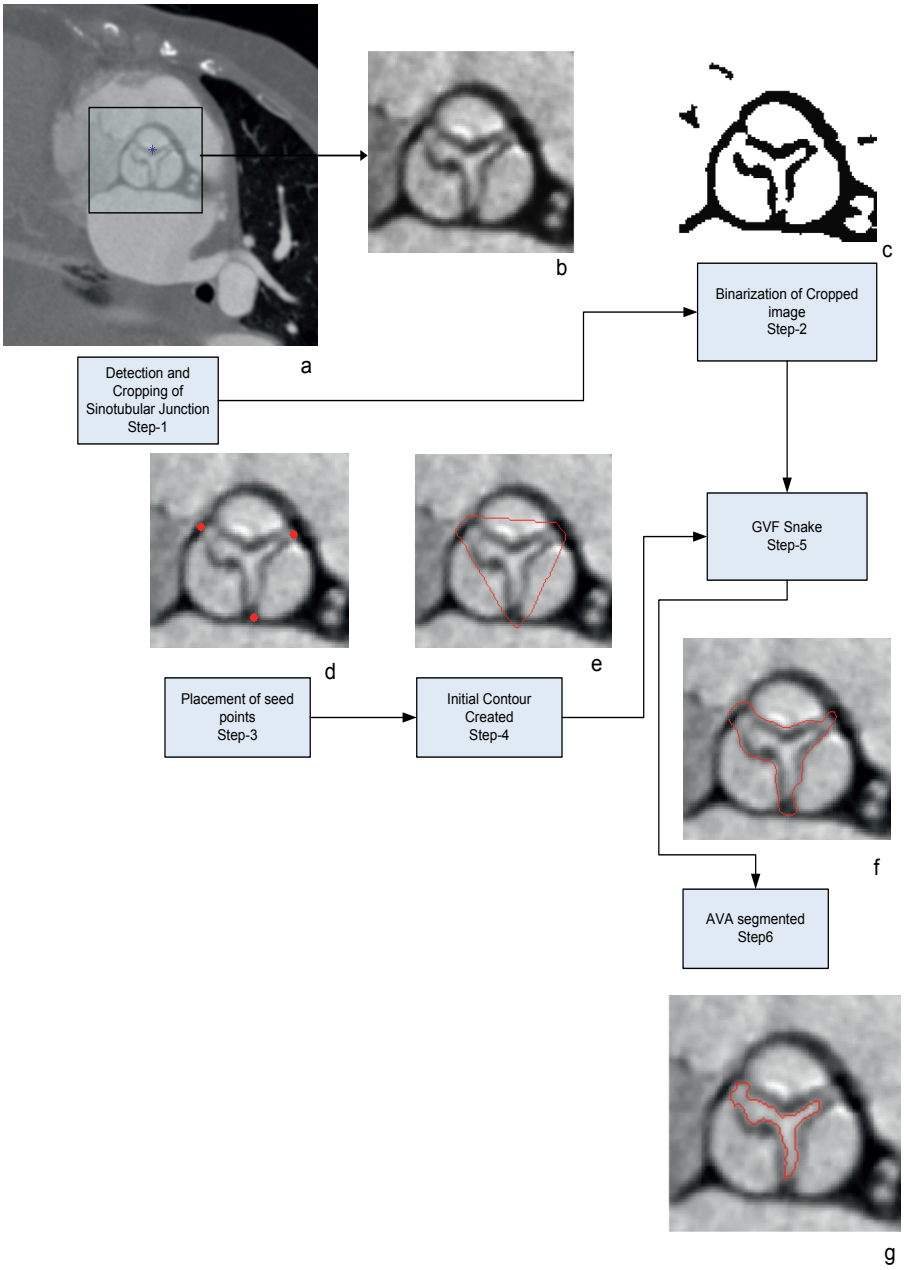

Figure 1: The flowchart of the general algorithm

Detection and Cropping of the Sinus of Valsalva

Image cropping was used to reduce computation time. In the object detection the object size, shape, location and orientation play major roles. Since the SOV is located in the central part of the MPR image, detection and cropping of this region begins with a preliminary cropping operation, which covers the most of the central part of the MPR image. After the initial cropping, the gray scale image is binarized using global thresholding with a threshold level based on the histogram of the image. The binary image contains only white (object) and black (background) pixels, which enables detection of the objects in the image and facilitates the use of morphological operations. Following binarization, objects smaller than 700 pixels were removed. Secondly, the SOV was disconnected and isolated. The SOV is located in the central part of image, such that objects on the border of the image were removed. After detection of the SOV, the region covering it was cropped from the image (Figure 2). All following operations were performed on the cropped image.

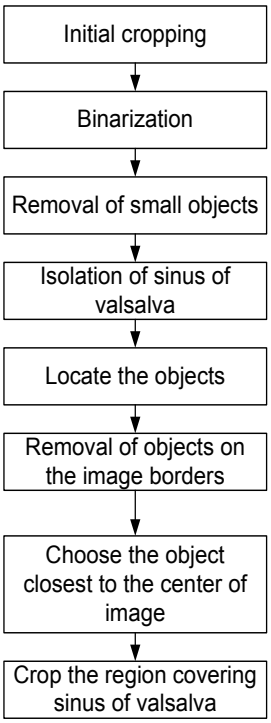

Figure 2: The flowchart of the SOV detection and cropping algorithm

Segmentation of AVA

The flowchart in Figure 3 shows the details of the segmentation of the AVA. The main segmentation tool is the gradient vector flow (GVF) snake (29). The snake algorithm is an active contour, which moves to the edges of the object in order to reach the boundaries of the object. In the binarized images (described above) the edges are clearer and the active contour can move towards the object boundaries easier compared to gray scale images. The user places three seed points on the grayscale image where the cusps are connected to each other to create the initial contour for the GVF snake. This initial contour creates a mask image, which is used on the binarized image. The active contour shrinks to cover the AVA region. However, the GVF snake result overestimates the AVA. Therefore, this GVF snake contour is used to mask the image again. In case the resulting double-masked image contains more than 1 object, the size and location of these objects were determined. Objects smaller than 40 mm2 and the object most distant from the center were removed. The remaining object was identified as the AVA.

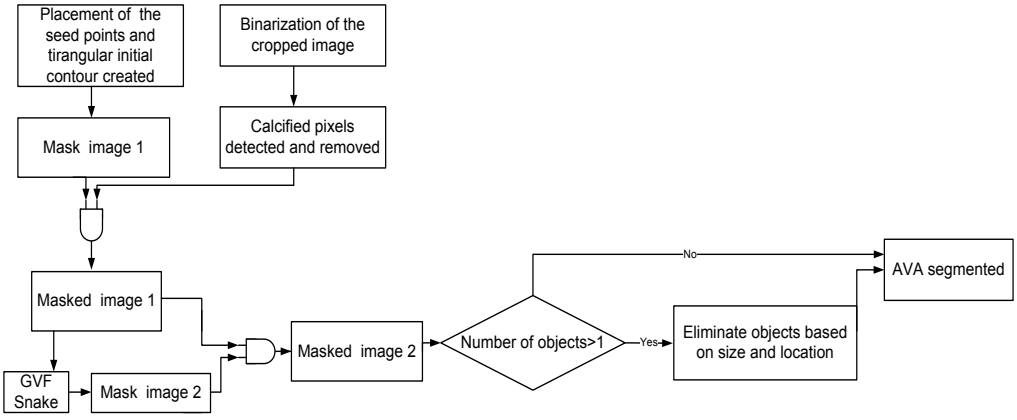

Figure 3: The flowchart of the AVA segmentation algorithm

Detection and Removal of Calcification

Aortic valve calcification is very common in a population with AS. In order to segment the AVA properly one must first detect the calcifications and then exclude the calcified areas from the AVA region. Since a contrast agent was used in the CT scans we cannot use the fixed 130 HU threshold to detect pixels in calcified areas. We therefore developed an algorithm to determine the threshold of calcified pixels, consisting of the following 5 steps:

1. Calculation of the histogram (Figure 4) and determination of the index number (index) of the maximum pixel intensity (imMax).
2. Calculation of the maximum histogram value (MaxH).
3. Decreasing the index until reaching MaxH/3 and setting the corresponding intensity level as the initial estimation (Tcalcest) for calculation of calcium threshold (Tcalc).
4. Determination of the dynamic range of the image:

- Starting from the first bin of the histogram, the amount of pixels in each bin was counted until reaching half of the total number of pixels.
- The index number of the histogram bin where the algorithm stopped corresponds to the dynamic range (DR) of the image.

5. Calculation of the calcium threshold (Tcalc) for DR>0.7* imMax (brighter images) by equation 1 and Tcalc for DR<0.7* imMax was calculated by equation 2

Tcalc=Tcalcest+(imMax-Tcalcest)*0.5 (1)

Tcalc=Tcalcest+(imMax-Tcalcest)*0.2 (2)

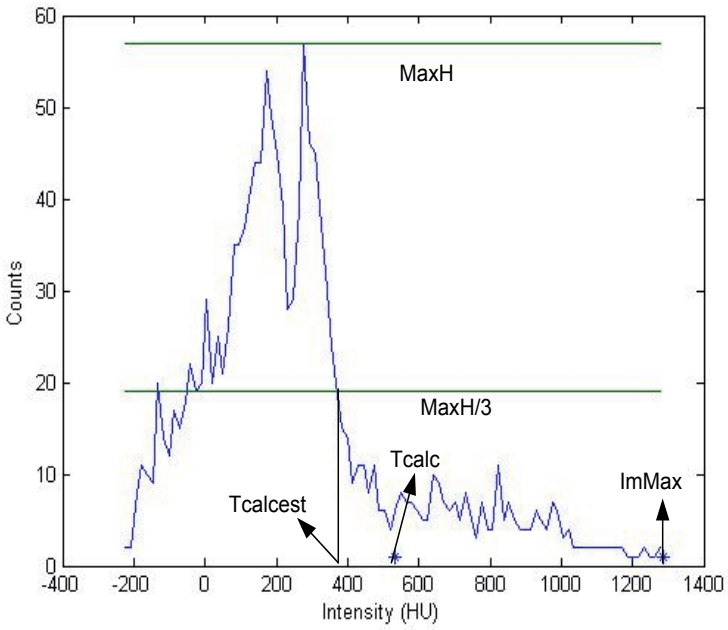

Figure 4: The histogram of the gray-scale image.

An example is given in the Figure 5. The calcified pixels on grayscale image (Figure 5a) are detected and given a blue color (Figure. 5b).

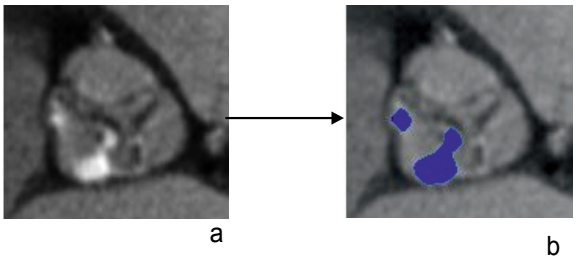

Figure 5: Example of the calcium detection algorithm.

Computation Time

Computation time was defined as the time between the visualization of the final cropped image and the display of the measurement of the AVA size. For manual measurements it included the time required for the user to trace the orifice perimeter and the calculation of the selected area. For the semi-automatic measurements it included the selection of the seed points by the user and the computation of AVA based on the semi-automatic segmentation results. The time was measured internally by the developed software tool and displayed when the AVA size measurement was finished.

Validation and Statistical Analysis

Relative differences between the measurements were calculated to determine 1) the intra-observer variability of the semi-automatic measurements, 2) the intra-observer variability of the manual measurements. Relative difference was calculated as follows:

Relative difference= Absolute difference *100/mean of the measurements

Differences between TTE and MDCT manual and semi-automatic measurements were assessed by Bland-Altman Plots. Statistical analyses were performed using IBM SPSS Statistics version 20.0.0.1 (SPSS Inc, Chicago, USA).

Results

Segmentation Results

Aortic valve areas as measured manually and semi-automatically are listed in Table1. Sample results of the semi-automatic segmentation are given in Figure 6. Semi-automatic segmentation of AVA was

achieved successfully for both calcified (Figure 6. a,b,d) and non-calcified aortic valves (Figure 6c). The output result of a segmentation and computation time for a sample image is given in Figure 6e showing one part of the graphic user interface.

Table 1: Manual and semi-automatic AVA measurements

AVA measurement types	**Mean ± SD**
Observer 1 Manual measurements (cm^2)	0.88±0.23
Observer 1 Semi-automatic measurements (cm^2)	0.85±0.15
Observer 2 Manual measurements (cm^2)	0.98±0.29
Observer 2 Semi-automatic measurements (cm^2)	0.82±0.18

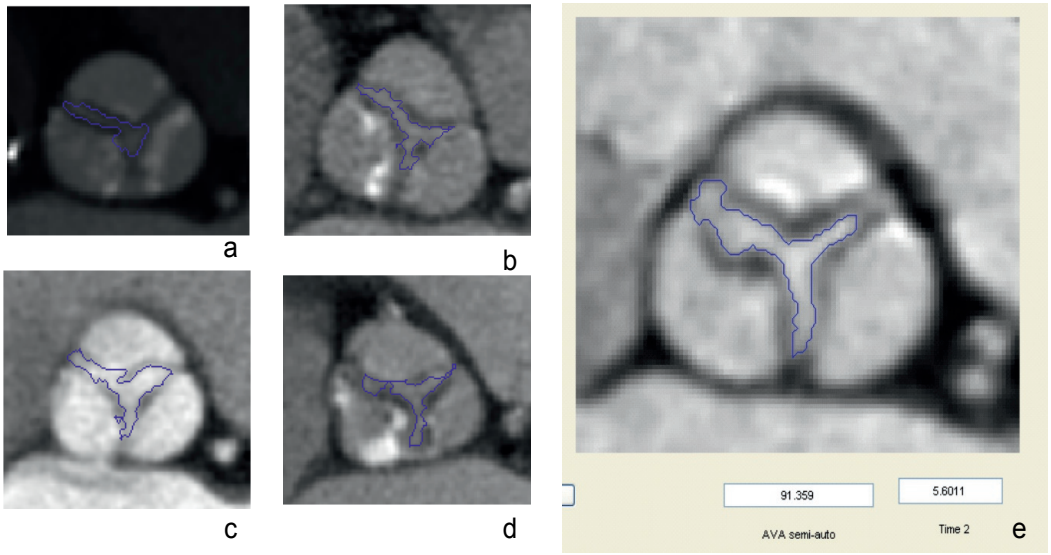

Figure 6: Results of semi-automatic measurements on various images (a-d), Result on graphic user interface (e).

Computation Time

The computation times of both observers were shorter for the semi-automatic measurements. Manual measurements took 18.85±5.66 seconds and 16.69±3.69 seconds for observer 1 and observer 2 respectively. Semi-automatic measurements were 5.06±0.72 (observer 1) and 6.68±1.79 seconds (observer 2).

Observer Variability

Differences in intra-observer variability of manual and semi-automatic measurements are listed in Table 2. Both intra- and inter-observer variability were lower for semi-automatic measurements

Table 2: Observer variability

Observer variability types	**Relative difference (%)**
Intra-observer variability Manual	8.4±7.1
Intra-observer variability Semi-automatic	5.8±4.5
Inter-observer variability Manual	27.6±16.0
Inter-observer variability Semi-automatic	16.8±12.7

Comparing Manual and Semi-automatic measurements with TTE

Comparison of the manual and semi-automatic measurements with TTE results were performed using Bland Altman plots; mean difference between TTE and MDCT results was -0.19(95 % CI:-0.74 to 0.34)cm2 for manual, and -0.10(95 % CI:-0.45 to 0.25)2 for semi-automatic measurements (Figure 7 and 8). The differences were significantly different from 0 ($p=0.001$ for manual and $p=0.007$ for semi-automatic measurements) indicating a bias. Both mean difference and the confidence interval are smaller in the comparison of TTE and semi automatic measurements which indicates that semi-automatic measurements are closer to the TTE measurements than the manual measurements.

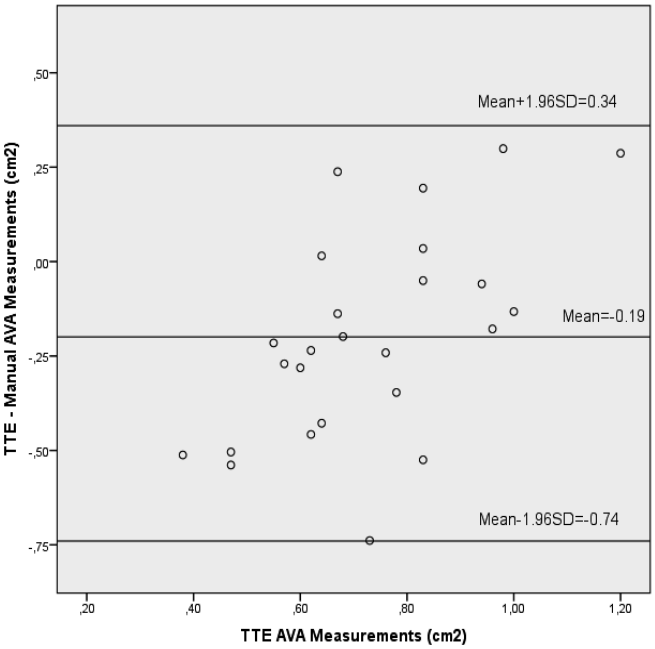

Figure 7: Bland-Altman plot between the TTE and manual AVA measurements

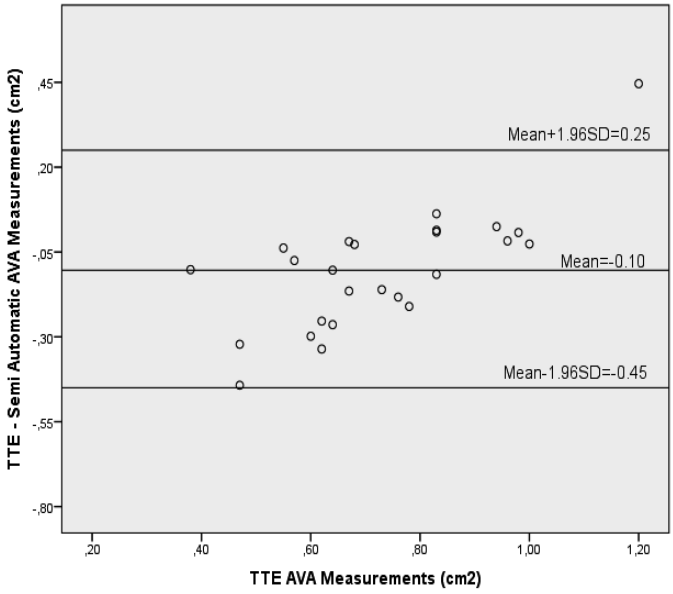

Figure. 8: Bland-Altman plot between the TTE and semi-automatic AVA measurements

Discussion

Research Summary

In this study we propose a semi-automatic segmentation technique to measure the AVA and compared it with the manual segmentation using TTE measurements as the reference standard. The focus of the study was to investigate whether the repeatability and reproducibility of the AVA measurements can be improved with the semi-automatic segmentation along with an improvement in computation time. First of all, our results show that semi-automatic measurements are closer to the reference TTE measurements. Furthermore, the intra- and inter-observer variations are lower for the semi-automatic measurements compared to manual measurements. Finally, semi-automatic measurements are more than 10 seconds faster than the manual measurements.

Previous Studies and Current Study

TTE is currently the most widely used imaging modality to measure the AVA. The continuity equation, which is used to calculate the AVA based on 2D TTE data, assumes that the LVOT has a circular shape. A recent study showed that this assumption might cause underestimation of the AVA [30]. TTE was compared to CT in several studies. Larsen et al. observed 6% and 16% intra- and inter- observer variability for MDCT measurements on patient with broad severity of AS. Meanwhile the intra- and inter- observer variability was 13% and 19 % for the TTE measurements [31]. In our study, the inter-observer variability of semi-automatic measurements was 16 % in the measurements on the patients with severe AS. Lembcke et al. conducted a study with 160 patient using 64- MDCT and TTE. They found 0.17 ± 0.24 cm^2 mean difference between MDCT and TTE measurements [32]. The mean differences in the comparisons of TTE with manual and semi-automatic MDCT measurements were 0.19 ± 0.27 cm^2 and 0.10 ± 0.18 cm^2 respectively.

Even though (semi)automatic quantification of the aortic root dimensions such as aortic annulus, sinus of valsalva and sinotubular junction using CT data has already been available in the literature [33] there is a paucity of data about (semi) automatic quantification of the AVA using CT images. Previous research already showed that echocardiography underestimates the AVA and CT planimetric measurements are closer to the real AVA. Moreover, CT is the modality used for measuring the aortic valve calcium score which associated with AS. All of these reasons make CT the method of choice. However, planimetric CT measurement of the AVA is currently performed manually, which is user

dependent and time consuming. Our results demonstrate the feasibility of developing an algorithm for semi-automatic quantitative measurements of AVA in order to reduce observer variability and the time spent on the measurements. Moreover, this technique is shown to also work on the target population of AS patients with a significant calcium load. The calcified regions should be detected and the opening area should be segmented excluding the calcified area. A calcification threshold is needed in order to detect the pixels belonging to the calcified region. However, in virtually all CT scans made for pre-operative evaluation in patients with aortic stenosis a contrast agent is injected which makes impossible to set a fixed calcification threshold. To overcome this issue, an algorithm was developed to calculate the calcification threshold for each CTA image individually.

The ultimate goal of fully automatic user independent segmentation was not achieved and user selection of three seed points is still required in the semi-automatic segmentation. Main reason for this is that the image quality with the current CT technology does not allow making the AVA segmentation fully automatic due to unclear object (AV) boundaries in some cases. The GVF snake was the method of choice since the snake algorithm works in cases where some parts of the object boundaries are not clear. A possible solution to make the segmentation less user dependent could be to develop an algorithm which can detect parts of the AVA boundaries (semi) automatically and interpolate the rest of the object boundary. Further developments in CT technology with higher spatial resolution and less calcium artifacts might also help to achieve the goal of fully automatic segmentation of the AVA. Our results show that CT based AVA segmentation can be achieved with less user dependence and as a result a higher reproducibility and less time-consuming measurements of AVA segmentation was obtained.

Limitations

A possible limitation of our study was that the users were not asked to re-choose the phase and opening plane on which to measure the AVA. However, this choice was made to eliminate the user interference in the measurement results in order to really test the accuracy of the developed algorithm. Another limitation of this study is the selected patient group. We studied a relatively small sample of patients with varying delay between TTE and CT imaging and all subjects had severe AS (mean AVA smaller than 1.0 cm^2.). Future work will have to be carried out in larger cohorts containing subject with varying degrees of AS. Also, we cannot rule out that differences in AVA can be attributed to differences in area over time as opposed to difference inherent to the imaging techniques used. The time difference between the CT and Ultrasound measurements was more than 100 days for 6 patients. A final limitation is having

2 different measurement techniques using the TTE and MDCT data. In MDCT measurements we had the direct measurements using the planimetric image of the AVA on the other hand AVA was measured indirectly by the flow information gathered by the TTE. This difference between the measurement techniques led to the variation between the TTE and MDCT manual and semi-automatic measurements. Therefore, further work required to determine what the clinical follow up should be based on MDCT measurements.

Implications

Studies comparing the use of CT and echocardiography found that CT can be an alternative to the current gold standard echocardiography in the quantification of AVA (26, 27). Our study has some implications in semi-automatic quantification of AVA on the CT images. First of all the intra- and inter observer variability of semi-automatic measurements are better than the manual measurements. These results imply that the variation caused by the user interaction is decreased by using the semi-automatic software, which is desirable for quantitative assessment of medical images. Moreover, semi-automatic software provides a faster calculation of the AVA in comparison with the manual measurements. Faster measurements decrease the workload. The comparison of manual and semi-automatic CT measurements with the current standard TTE measurements revealed that semi-automatic measurements are closer to the TTE measurements. If the standard modality for measuring the AVA will switch from echocardiography to CT, semi-automatic measurements can serve as a better option in comparison to the manual measurements due to the smaller difference between the TTE and semi-automatic measurements.

Conclusion

In this study, a semi-automatic segmentation technique that can be used in AVA segmentation is proposed. Based on preliminary results the algorithm provides adequate segmentation of representative images also those including severe calcification and provides a faster, more accurate and more reproducible AVA segmentation compared to the currently used manual segmentation.

References

1. Lindroos M, Kupari M, Heikkila J, Tilvis R. Prevalence of aortic valve abnormalities in the elderly: An echocardiographic study of a random population sample. J Am Coll Cardiol. 1993 Apr;21(5):1220-5.

2. Grossman W, Jones D, McLaurin LP. Wall stress and patterns of hypertrophy in the human left ventricle. J Clin Invest. 1975 Jul;56(1):56-64.

3. American College of Cardiology/American Heart Association Task Force on Practice Guidelines, Society of Cardiovascular Anesthesiologists, Society for Cardiovascular Angiography and Interventions, Society of Thoracic Surgeons, Bonow RO, Carabello BA, et al. ACC/AHA 2006 guidelines for the management of patients with valvular heart disease: A report of the american college of Cardiology/American heart association task force on practice guidelines (writing committee to revise the 1998 guidelines for the management of patients with valvular heart disease): Developed in collaboration with the society of cardiovascular anesthesiologists: Endorsed by the society for cardiovascular angiography and interventions and the society of thoracic surgeons. Circulation. 2006 Aug 1;114(5):e84-231.

4. Iung B, Cachier A, Baron G, Messika-Zeitoun D, Delahaye F, Tornos P, et al. Decision-making in elderly patients with severe aortic stenosis: Why are so many denied surgery? Eur Heart J. 2005 Dec;26(24):2714-20.

5. Andersen HR, Knudsen LL, Hasenkam JM. Transluminal implantation of artificial heart valves. description of a new expandable aortic valve and initial results with implantation by catheter technique in closed chest pigs. Eur Heart J. 1992 May;13(5):704-8.

6. Cribier A, Eltchaninoff H, Tron C, Bauer F, Agatiello C, Sebagh L, et al. Early experience with percutaneous transcatheter implantation of heart valve prosthesis for the treatment of end-stage inoperable patients with calcific aortic stenosis. J Am Coll Cardiol. 2004 Feb 18;43(4):698-703.

7. Grube E, Laborde JC, Gerckens U, Felderhoff T, Sauren B, Buellesfeld L, et al. Percutaneous implantation of the CoreValve self-expanding valve prosthesis in high-risk patients with aortic valve disease: The siegburg first-in-man study. Circulation. 2006 Oct 10;114(15):1616-24.

8. Grube E, Schuler G, Buellesfeld L, Gerckens U, Linke A, Wenaweser P, et al. Percutaneous aortic valve replacement for severe aortic stenosis in high-risk patients using the second- and current third-generation self-expanding CoreValve prosthesis: Device success and 30-day clinical outcome. J Am Coll Cardiol. 2007 Jul 3;50(1):69-76.

9. Lichtenstein SV, Cheung A, Ye J, Thompson CR, Carere RG, Pasupati S, et al. Transapical transcatheter aortic valve implantation in humans: Initial clinical experience. Circulation. 2006 Aug 8;114(6):591-6.

10. Webb JG, Chandavimol M, Thompson CR, Ricci DR, Carere RG, Munt BI, et al. Percutaneous aortic valve implantation retrograde from the femoral artery. Circulation. 2006 Feb 14;113(6):842-50.

11. Webb JG, Pasupati S, Humphries K, Thompson C, Altwegg L, Moss R, et al. Percutaneous transarterial aortic valve replacement in selected high-risk patients with aortic stenosis. Circulation. 2007 Aug 14;116(7):755-63.

12. Saikrishnan N, Kumar G, Sawaya FJ, Lerakis S, Yoganathan AP. Accurate assessment of aortic stenosis: A review of diagnostic modalities and hemodynamics. Circulation. 2014 Jan 14;129(2):244-53.

13. Willmann JK, Weishaupt D, Lachat M, Kobza R, Roos JE, Seifert B, et al. Electrocardiographically gated multi-detector row CT for assessment of valvular morphology and calcification in aortic stenosis. Radiology. 2002 Oct;225(1):120-8.

14. Feuchtner GM, Muller S, Bonatti J, Schachner T, Velik-Salchner C, Pachinger O, et al. Sixty-four slice CT evaluation of aortic stenosis using planimetry of the aortic valve area. AJR Am J Roentgenol. 2007 Jul;189(1):197-203.

15. Bouvier E, Logeart D, Sablayrolles JL, Feignoux J, Scheuble C, Touche T, et al. Diagnosis of aortic valvular stenosis by multislice cardiac computed tomography. Eur Heart J. 2006 Dec;27(24):3033-8.

16. Gilkeson RC, Markowitz AH, Balgude A, Sachs PB. MDCT evaluation of aortic valvular disease. AJR Am J Roentgenol. 2006 Feb;186(2):350-60.

17. Cowell SJ, Newby DE, Burton J, White A, Northridge DB, Boon NA, et al. Aortic valve calcification on computed tomography predicts the severity of aortic stenosis. Clin Radiol. 2003 Sep;58(9):712-6.

18. Koos R, Mahnken AH, Sinha AM, Wildberger JE, Hoffmann R, Kuhl HP. Aortic valve calcification as a marker for aortic stenosis severity: Assessment on 16-MDCT. AJR Am J Roentgenol. 2004 Dec;183(6):1813-8.

19. Morgan-Hughes GJ, Owens PE, Roobottom CA, Marshall AJ. Three dimensional volume quantification of aortic valve calcification using multislice computed tomography. Heart. 2003 Oct;89(10):1191-4.

20. Bruder O, Jochims M, Hunold P, Jensen C, Forsting M, Sabin GV, et al. Comparison of aortic valve area measured by magnetic resonance imaging and dual-source computed tomography. Acta Radiol. 2009 Jul;50(6):645-51.

21. Lembcke A, Kivelitz DE, Borges AC, Lachnitt A, Hein PA, Dohmen PM, et al. Quantification of aortic valve stenosis: Head-to-head comparison of 64-slice spiral computed tomography with transesophageal and transthoracic echocardiography and cardiac catheterization. Invest Radiol. 2009 Jan;44(1):7-14.

22. Weinberg EJ, Kaazempur Mofrad MR. A multiscale computational comparison of the bicuspid and tricuspid aortic valves in relation to calcific aortic stenosis. J Biomech. 2008 Dec 5;41(16):3482-7.

23. Chenot F, Montant P, Goffinet C, Pasquet A, Vancraeynest D, Coche E, et al. Evaluation of anatomic valve opening and leaflet morphology in aortic valve bioprosthesis by using multidetector CT: Comparison with transthoracic echocardiography. Radiology. 2010 May;255(2):377-85.

24. Flachskampf FA. Severe aortic stenosis with low gradient and apparently preserved left ventricular systolic function--under-recognized or overdiagnosed? Eur Heart J. 2008 Apr;29(8):966-8.

25. Poh KK, Levine RA, Solis J, Shen L, Flaherty M, Kang YJ, et al. Assessing aortic valve area in aortic stenosis by continuity equation: A novel approach using real-time three-dimensional echocardiography. Eur Heart J. 2008 Oct;29(20):2526-35.

26. Klass O, Walker MJ, Olszewski ME, Bahner J, Feuerlein S, Hoffmann MH, et al. Quantification of aortic valve area at 256-slice computed tomography: Comparison with transesophageal echocardiography and cardiac catheterization in subjects with high-grade aortic valve stenosis prior to percutaneous valve replacement. Eur J Radiol. 2011 Oct;80(1):151-7.

27. Delgado V, Bax JJ. Classical methods to measure aortic valve area in the era of new invasive therapies: Still accurate enough? Int J Cardiovasc Imaging. 2009 Feb;25(2):183-5.

28. Gaspar T, Adawi S, Sachner R, Asmer I, Ganaeem M, Rubinshtein R, et al. Three-dimensional imaging of the left ventricular outflow tract: Impact on aortic valve area estimation by the continuity equation. J Am Soc Echocardiogr. 2012 Jul;25(7):749-57.

29. Xu C, Prince JL. Snakes, shapes, and gradient vector flow. IEEE Trans Image Process. 1998;7(3):359-69.

30. Utsunomiya H, Yamamoto H, Horiguchi J, Kunita E, Okada T, Yamazato R, et al. Underestimation of aortic valve area in calcified aortic valve disease: Effects of left ventricular outflow tract ellipticity. Int J Cardiol. 2012 Jun 14;157(3):347-53.

31. Larsen LH, Kofoed KF, Carstensen HG, Mejdahl MR, Andersen MJ, Kjaergaard J, et al. Aortic valve area assessed with 320-detector computed tomography: Comparison with transthoracic echocardiography. Int J Cardiovasc Imaging. 2014 Jan;30(1):165-73.

32. Lembcke A, Woinke M, Borges AC, Dohmen PM, Lachnitt A, Westermann Y, et al. Grading of aortic valve stenosis at 64-slice spiral computed tomography: Comparison with transthoracic echocardiography and calibration against cardiac catheterization. Invest Radiol. 2009 Jun;44(6):360-8.

33. Delgado V, Ng AC, Schuijf JD, van der Kley F, Shanks M, Tops LF, et al. Automated assessment of the aortic root dimensions with multidetector row computed tomography. Ann Thorac Surg. 2011 Mar;91(3):716-23.

Chapter 8 Does the Aortic Annulus undergo dynamic conformational changes during the cardiac cycle? A systematic Review

Publication: Does the Aortic Annulus undergo dynamic conformational changes during the cardiac cycle? A systematic Review

Sucha D, Tuncay V, Prakken NHJ, Leiner T, van Ooijen PMA, Oudkerk M, Budde RPJ.

European Heart Journal Cardiovascular Imaging 2015;16(12):1307-1217.

Introduction

In the elderly, the prevalence of moderate-to-severe aortic stenosis (AS) is ~3%.[1] About half of all patients with severe AS are referred for surgical aortic valve replacement (AVR).[2] For selected high-risk patients, transcatheter aortic valve implantation (TAVI) has become a successful alternative to conventional valve surgery.[3,4]

In conventional AVR, the appropriate size of the prosthesis is determined by direct measurements of the annulus during surgery. In TAVI, assessment of the annular and prosthetic size relies entirely on preprocedural and/or periprocedural imaging. Precise aortic root measurement is essential for choosing the correct prosthesis size to minimize the risk of complications such as significant (.mild) paravalvular regurgitation, which has been reported in 1–39% of TAVI patients.[5 – 7] Measurements of the aortic annulus were originally performed using transthoracic or transesophageal two dimensional echocardiography (TTE and TEE, respectively). However, studies have found the aortic annulus to often have an ellipsoid shape rather than a circular structure.[8–10] Hence, three-dimensional echocardiography or computed tomography (CT) allows for more accurate assessment of the shape and size of the annulus by providing images in any desired imaging plane.

The ascending aorta is known to undergo conformational changes during the cardiac cycle.[11,12] However, no consensus exists whether such changes are also present in the aortic annulus and in what way. If the annulus does undergo significant dynamic changes, this may affect selection of the most optimal cardiac phase for measurement and improve prosthesis sizing or even prosthesis design. In order to clarify this concern, we conducted a systematic review of all the literature investigating the dynamic behaviour of the aortic annulus using echocardiography, CT, and/or magnetic resonance imaging (MRI).

Methods

Literature search

PubMed and Embase databases were systematically searched on 25 June 2014 using the search syntax presented in the Appendix. In Embase, we included only articles, articles in press, reviews, and short surveys. No other limitations were applied. Two reviewers (D.S., V.T.) screened all titles and abstracts independently. In total, 5637 articles were found and 2173 duplicates excluded manually (Figure 1).

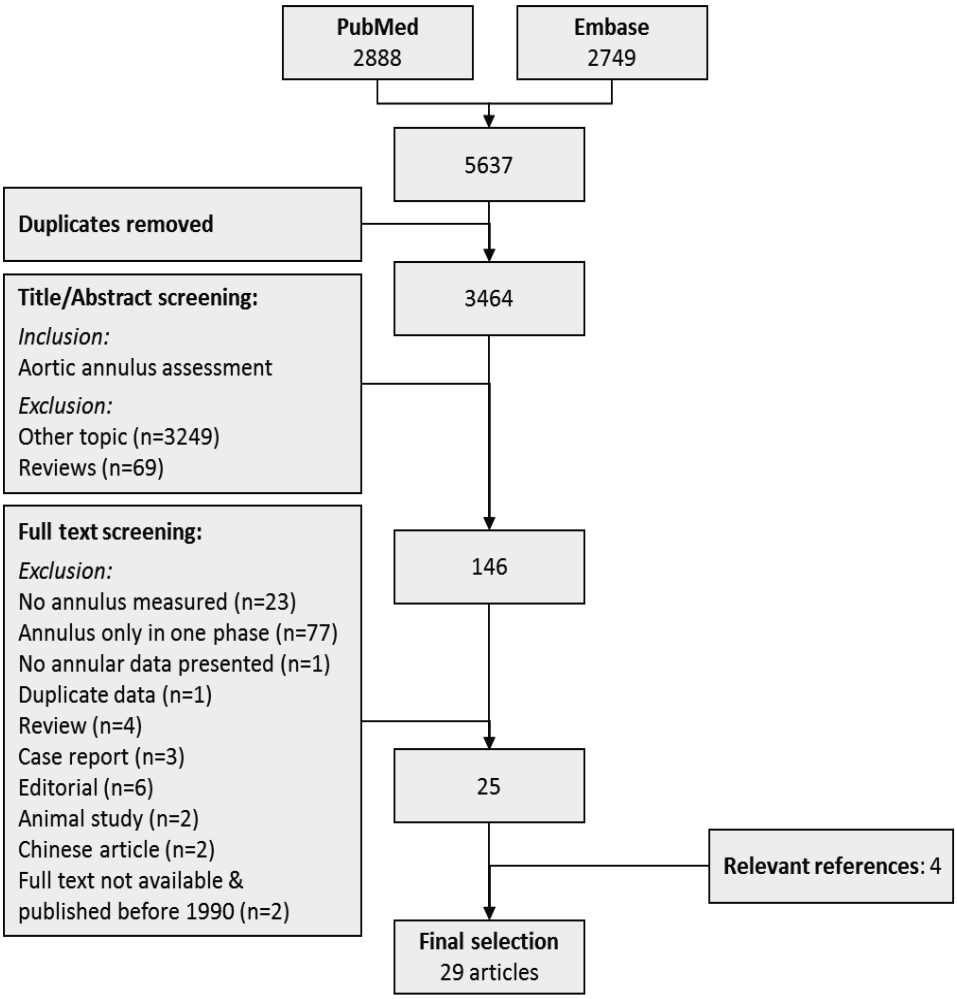

Figure 1: Literature search

Article selection

Only articles aimed at imaging and evaluation of the aortic annulus were included for further screening. In total, 146 articles were selected for full text screening. Both reviewers independently excluded studies evaluating the annulus only in one cardiac phase and articles on other aortic/cardiac dimensions than the annulus. Furthermore, studies on animals, case reports, reviews, editorials, and non-English articles were excluded (Figure 1). A third reviewer (R.B.) settled discordant judgements. Our selection comprised 25 articles on aortic annulus change during the cardiac cycle. References and citations were screened for relevant articles not included in our search. This resulted in four additional articles,[13 – 16] since

annulus as defined in the search syntax was not mentioned in the title/abstract. The final selection included 29 articles.

Data extraction

We extracted the following data from the selected articles: first author, journal, publication year, number of patients, mean age, gender, number of patients with AS, definition of AS and mean aortic valve area, imaging modalities used for measurements including selected plane and imaging phase, definition of annulus, annulus measurement method (manual, semi-automatic), and annular parameters within the cardiac cycle.

Results

Study characteristics

Twenty-nine original articles were included published from 2001 to 2014. Of these, seven evaluated annular dynamic changes in healthy subjects (e.g. no aortic root or valve disease), 10 compared a healthy population with AS patients and 12 studies included only AS patients. In total, 2021 subjects were evaluated with a mean age ranging from 11±3.6 to 84.9±7.2 years. Study and patient characteristics are summarized in Table 1.

Table 1: Study characteristics

			No aortic stenosis		
Author, country (ref)	**Year**	**Patient population**	**N Patients**	**Mean age ± SD**	**N Males (%)**
Burman, UK (18)	2008	Healthy subjects	120	49.3 ± 17.2*	60 (50%)
de Heer, Netherlands (10)	2011	CAD screening	108	56.1 ± 12.5	89 (82%)
Kazui, Japan (20)	2006	Normal aortic root/valve	25	60.1 ± 14.8	17 (68%)
Martin, France (31)	2013	Cardiac murmur/pre chemotherapy	30	11 ± 3.6	NA
de Paulis, Italy (13)	2001	Normal aortic root/valve	7	45.3 ± 19	6 (86%)
Veronesi, Italy (16)	2009	Normal aortic root/valve	24	54 ± 20	7 (29%)
Zhu, China (21)	2011	Healthy subjects	314	37.2 ± 13.5	133 (42%)
de Heer, Netherlands (24)	2012	CAD screening vs TAVI indicated	15	53 ± 12	12 (80%)

Hamdan, Israel (33)	2012	CAD screening vs TAVI indicated	11	56.2 ± 11.8	5 (45%)
Izumi, Japan (22)	2012	Pre AF ablation vs AS	37	68 ± 5	10 (27%)
Otani, Japan (43)	2010	TEE indicated non-AS vs AS	80	70 ± 10	43 (54%)
Shabestari, Iran (32)	2013	CAD screening vs aortic calcification	52	50.5 ± 11.3	27 (26%)
Shiran, Israel (14)	2009	TEE non-AS vs AS	30	62 ± 13	18 (60%)
Tops, Netherlands (8)	2008	CAD screening no/mild AS vs AS	150	54 ± 11‡	111 (66%)‡
Tsang, USA (26)	2013	Stroke work-up vs TAVI indicated	16	80 ± 5	7 (44%)
Tsang, USA (15)	2013	Normal valves vs AS	20	59.2 ± 17	10 (50%)
Yoshikawa, Japan (23)	2013	Stroke work-up vs AS	40	65.1 ± 11.7	24 (60%)
Bertaso, Australia (17)	2012	TAVI indicated	-	-	-
Blanke, USA (35)	2012	TAVI indicated	-	-	-
Bolen, USA (27)	2012	TAVI indicated	-	-	-
Jilaihawi, USA (25)	2012	TAVI indicated	-	-	-
Kempfert, Germany (44)	2012	Pre conventional AVR	-	-	-
Lehmkuhl, Germany (28)	2013	TAVI indicated	-	-	-
Lehmkuhl, Germany (34)	2013	TAVI indicated	-	-	-
Masri, USA (42)	2014	Pre TAVI or conventional AVR	-	-	-
Peng, China (36)	2012	Severe AS	-	-	-
Pontone, Italy (29)	2011	TAVI indicated	-	-	-
Willson, Canada (30)	2012	TAVI indicated	-	-	-
Wood, Canada (19)	2009	TAVI indicated	-	-	-

* Of male subjects

† Of total group (n=52)

‡ Of total group (n=169)

§ 2D speckle tracking echocardiography

‖ Of total group (n=96)

¶ Of total group (n=120)

AVA(i)= aortic valve area (indexed); AS= aortic stenosis; CAD= coronary artery disease; CT= computed tomography; NA= not available;

HU= CT Hounsfield units; MRI= magnetic resonance imaging; PG= pressure gradient; SD= standard deviation;
TAVI= transcatheter aortic valve implantation; TEE= transesophageal echocardiography; TTE= transthoracic echocardiography

Aortic stenosis						
N patients	**Mean age ± SD**	**N Males (%)**	**Definition stenosis**	**AVA (cm^2)**	**Mean gradient**	**Imaging**
-	-	-	-	-	-	MRI
-	-	-	-	-	-	CT
-	-	-	-	-	-	CT
-	-	-	-	-	-	TTE-2D-3D
-	-	-	-	-	-	TEE-2D
-	-	-	-	-	-	TEE-3D
-	-	-	-	-	-	TTE-2D
20	81 ± 6	6 (30%)	not defined	NA	39 ± 14	CT
35	80.1 ± 7.4	16 (46%)	not defined	NA	NA	CT
23	73 ± 5	10 (43%)	not defined	NA	NA	TTE-3D
71	73 ± 8	41 (58%)	not defined	1.1 ± 0.4	38 ± 20	TEE-3D
30	66.58 ± 8.90†	30 (58%)†	aortic valve calcifications >100 HU	NA	NA	CT
20	78 ± 9	5 (25%)	not defined	NA	NA	TTE-2D, TEE-2D
17	54 ± 11‡	111 (66%)‡	moderate to severe AS	0.8 ± 0.2	50 ± 21	CT
27	82 ± 7	16 (59%)	AVA <1.0cm^2, mean PG>40mmHg	0.7 ± 0.1	40 ± 12	TEE-3D
20	72 ± 9	14 (70%)	AVA <1.0cm^2, mean PG >40mmHg	0.9 ± 0.2	47 ± 11	TEE-3D
40	69.3 ± 9.6	25 (63%)	AVA <1.0cm^2 or PG>40mmHg	0.8 ± 0.4	43.2 ± 18.4	TEE-2D§
59	82.4 ± 5	29 (49%)	AVA <1cm^2, AVAi <0.6cm^2/m^2	0.73 ± 0.2	NA	CT
110	82.9 ± 7.9	27 (25%)	severe AS	0.69 ± 0.18	43.6 ± 14.1	CT
47	78 ± 9.5	25 (53%)	not defined	CT: 0.93 ± 0.24	NA	CT
20	84.9 ± 7.2‖	50 (52%)‖	not defined	NA	NA	CT
26	NA	NA	severe AS	NA	NA	TTE-2D,

						TEE-2D
56	81.6 ± 6.8	16 (29%)	severe AS	90.7 ± 14.2(mm^2)	NA	CT
27	82.3 ± 11.2	6 (22%)	severe AS	NA	NA	CT
87	81 ± 10	47 (54%)	symptomatic severe AS	0.6 ± 0.1	46 ± 13	CT
62	68.2 ± 5.9	41 (66%)	not defined	0.83 ± 0.17	61.6 ± 20.9	CT
60	80 ± 8	22 (37%)	not defined	0.7 ± 0.2	51.9 ± 15.2	CT
66	81.4 ± 7.8¶	57 (48%)¶	not defined	0.68 ± 0.16§	42.9 ± 16.6§	CT
19	83.5	NA	symptomatic severe AS	0.59	50.7	CT

Imaging characteristics

Two-dimensional echocardiography (TTE and/or TEE) in systole and diastole was performed in six studies, all using the parasternal long-axis view. Three-dimensional modalities used for assessment of the annulus were echocardiography (6 studies), MRI (1 study), and CT (17 studies). The CT acquisition protocol comprised retrospective ECG-gating in 15 studies, wide-window (20–90%) dose modulated prospective ECG-triggering in one study and one study did not specify the CT protocol. Of all three-dimensional modality studies, the MRI and four CT studies evaluated coronal and/or sagittal plane reconstructions[8,10,17 – 19] and one CT study used an undefined longitudinal view.[20] Reconstructed double oblique images in plane with the aortic annulus were evaluated in 19 studies. Since the annulus is not a true anatomical structure, the exact location of anatomical measurements had to be specified. The aortic annulus was defined in general as a virtual ring at the lowest, most caudal, insertion of the valve leaflets in 22 studies. Two studies measured the ventriculo-arterial junction [20,21] and five studies did not specify aortic annulus.[8,13,18,22,23] Annular measurements were performed semi-automatically in six studies[15,16,23 – 26] and manually in the remaining 23 studies.

Deformation during the cardiac cycle

On parasternal long-axis view, the annulus diameter was larger in systole than in diastole in 9 of 10 studies (Table 2, largest mean difference 2.9±0.7 mm). Only two studies performed paired T-tests[14,20] of which one found a significant change for TEE-derived diameter throughout the cycle (mean difference 0.3±0.7 mm, P = 0.0005).[14] No significant change was shown for TTE-derived diameter measurements.

Table 2: Parasternal long axis annulus diameter measurements

Author	Imaging	Cardiac phase measured	Systole	Diastole	Mean difference	P-value
Patients without aortic valve stenosis						
Kazui (20)	CT*	40%, 80% RR-interval	22.5 ± 2.2	22.1 ± 2.2	-	NS
Martin (31)	TTE-2D	mid-systole, end-diastole	19.4	19.5	-	-
de Paulis (13)	TEE-2D	systole, diastole	22.2 ± 1.6	20.6 ± 1	7% ± 3.2%	-
Shiran† (14)	TTE-2D	mid-systole, end-diastole	21.1 ± 2.1	21.0 ± 1.8	0.2 ± 0.8	P= 0.2
	TEE-2D	mid-systole, end-diastole	21.6 ± 2.2	21.3± 2.1	0.3 ± 0.7	P= 0.0005
Yoshikawa (23)	TEE-2D‡	83 ms, 421 ms from ECG R-wave	22.9 ± 2.7	20.0 ± 2.9	2.9 ± 0.7	-
Zhu (21)	TTE-2D	mid-systole, end-diastole	20.91 ± 2.3	20.35 ± 8.7	-	-
Patients with aortic valve stenosis						
Kempfert (44)	TTE-2D	end-systole, end-diastole	24.2 ± 3.5	22.9 ± 3.1	-	-
	TEE-2D	end-systole, end-diastole	24.5 ± 2.7	23.8 ± 2.7	-	-
Yoshikawa (23)	TEE-2D‡	99 ms, 435 ms from ECG R-wave	21.6 ± 2.6	19.4 ± 2.6	2.2 ± 0.6	-

All annular measurements are presented in millimeters as mean ± standard deviation

* In CT longitudinal view

† Results are the same for non-stenosis and stenosis patients

‡ TEE speckle tracing

CT= computed tomography; NS= non-significant; ms= milliseconds; TEE= transesophageal echocardiography; TTE= transthoracic echocardiography

Results on coronal view measurements were contradictory as the largest annulus diameter was found either in the systolic (n = 3) or diastolic phase (n = 3) (Table 3). One study evaluated the mean diameter difference between these phases (0.23 mm) but no statistical significance was reached. [17] However, all results on sagittal view showed larger systolic than diastolic annulus diameters with significant difference (mean 0.42 mm, P = 0.008), though tested only by one study [17] (Table 3).

Table 3: Coronal and sagittal axis annulus diameter measurements

			Coronal view				Sagittal view			
Author	**Imaging**	**Cardiac phase measured**	**Systole**	**Diastole**	**Mean Δ**	**P-value**	**Systole**	**Diastole**	**Mean Δ**	**P-value**
Patients without aortic valve stenosis										
Burman (18)	MRI	max systolic, end-diastolic	25.7 ± 2.1 (M)	26.2 ± 2.3	-	-	22.4 ± 2.1	22.2 ± 2.4	-	-
			23.0 ± 2.0 (F)	23.0 ± 2.1	-	-	21.0 ± 2.1	19.9 ± 1.9	-	-
de Heer (10)	CT	30-40%, 70-75% RR-interval	26.6 ± 2.8	26.9 ± 2.4	-	-	-	-	-	-
Tops (8)	CT	30%, 75% RR-interval	26.4 ± 2.8	26.3 ± 2.6	-	-	24.0 ± 2.6	23.4 ± 2.7	-	-
Patients with aortic valve stenosis										
Bertaso (17)	CT	30-40%. 70-80% RR-interval	25.3 ± 2.7	25.5 ± 2.7	0.23 (0.9%)	0.115	22 ± 2.4	21.6 ± 2.3	0.42 (1.9%)	0.008
Tops (8)	CT	30%, 75% RR-interval	27.3 ± 3.7	26.7 ± 3.9	-	-	24.7 ± 3.0	24.2 ± 3.0	-	-
Wood (19)	CT	30%, 70% RR-interval	25.7 ± 1.5	25.5 ± 2.5	-	-	22.4 ± 1.3	21.5 ± 2.1	-	-

All annular measurements are presented in millimeters as mean ± standard deviation

(F)= in females; (M)= in males

Mean Δ= mean difference between systolic and diastolic measurement

Table 4 shows all diameter measurements acquired using the double oblique in plane view. No evident pattern was found for change in maximal (long axis) annulus diameter since it was largest either in systole or diastole in seven patient groups each. Statistical analysis was performed by seven studies [10,17,25,27 – 30] but only one found significant differences (mean 0.3±2.4 mm in diastole, $P < 0.001$). [10] In contrast, the minimal (short axis) annulus diameter was largest in systole in the majority of patients (16 study groups) and in diastole in three studies (four patient groups). [22,31,32] The change in diameter (Figure 2) was significant in 11 patient groups[10,17,22,25,27,28,30,33,34] all showing a greater short-axis diameter in systole except for the two groups of Izumi et al.[22] Pontone et al.[29] did not find significant differences.

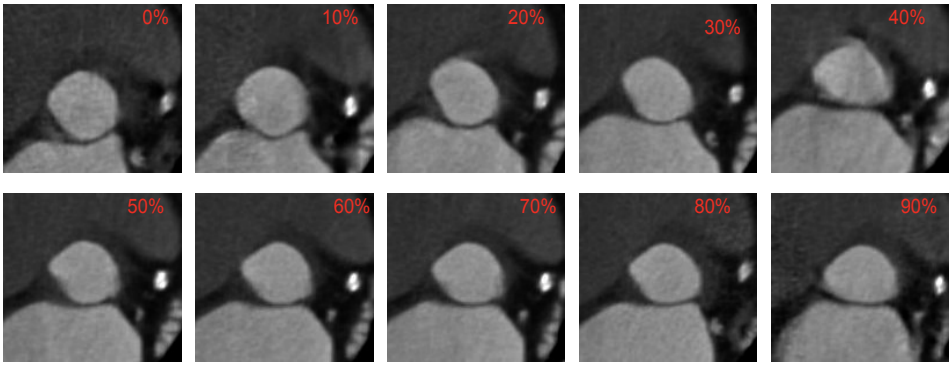

Figure 2: Dynamic deformation of the annulus. Cardiac ECG-gated multidetector-row computed tomography images reconstructed in each 10% phase of the RR-interval. Note the conformational change of the aortic annulus showing a more circular shape during systole and an oval shape during diastole. Whereas the long-axis diameter remains relatively stable, the short-axis diameter undergoes significant change throughout the cycle.

Table 4: Double oblique plane annulus diameter measurements

Author	Imaging	Cardiac phase measured	Maximal diameter (mm)				Minimal diameter			
			Systole	Diastole	Mean Δ	P-value	Systole	Diastole	Mean Δ	P-value
Patients without aortic valve stenosis										
Hamdan (33)	CT	all: max 30%, min 90-0%	-	-	-	-	21.7 ± 1.8	19.0 ± 2.6	12.3 ± 7.3%	<0.001
de Heer (10)	CT	30-40%, 70-75%	29.7 ± 3.4	30.1 ± 3.0	0.3 ± 2.4	<0.001	25.1 ± 3.3	24.0 ± 3.1	1.1 ± 2.0	NS
Izumi (22)	TTE-3D	end-systole, end-diastole	-	-	-	-	20.6 ± 1.4	22.4 ± 1.6	7.8 ± 3.4%	<0.0001
Martin (31)	TTE-3D	mid-systole, end-diastole	20.1	20.1	-	-	18.8	19.3	-	-
Otani (43)	TEE-3D	mid-systole, end-diastole	24.6 ± 2.1	25.0 ± 2.2	-	-	19.6 ± 1.8	19.1 ± 1.8	-	-
Shabestari (32)	CT	30-35%, 70-75%	26.7 ± 2.7	27.9 ± 3.1	0.59	-	20.80 ± 2.47	20.86 ± 1.81	0.05	-
Patients with aortic valve stenosis										
Bertaso (17)	CT	30-40%, 70-80%	28.7 ± 2.7	28.4 ± 2.7	0.24 (0.7%)	0.163	22.4 ± 2.4	21.7 ± 2.4	0.75 (3.4%)	0.004
Blanke (35)	CT	all: max 20%, min 60%	27.8*	26.8*	2%	-	22.0 ± 1.9	19.8*	11%	-
Bolen (27)	CT	20-30%, 90%	28.4 ± 3.5	28.7 ± 3.4	-	0.67	22.9 ± 2.4	21.4 ± 2.5	-	0.006
Hamdan (33)	CT	all: max 30%, min 90-0%	-	-	-	-	22.6 ± 2.9	20.4 ± 2.7	9.8 ± 3.4 %	<0.001

Izumi (22)	TTE-3D	end-systole, end-diastole	-	-	-	-	18.7 ± 1.9	19.1 ± 1.7	2.0 ± 2.2%	<0.0001
Jilaihawi (25)	CT	mean at 16% and 54%	27.1 ± 2.9	26.8 ± 2.8	-	0.43	21.3 ± 2.7	19.7 ± 2.3	-	<0.0001
Lehmkuhl (28)	CT	40-50%, 90-0%	27.1 ± 3†	27.0 ± 3.0†	1.6 ± 1.2	NS	24.8 ± 2.9‡	23.0 ± 3.2‡	2.2 ± 1.6	<0.001
Lehmkuhl (34)	CT	end-systole, end-diastole	24.7 ± 2.2†	24.8 ± 2.0†	-	-	21.4 ± 1.8‡	20.5 ± 2.0‡	1.2 ± 2.0	<0.01
Masri (42)	CT	all: max NA, min NA	26 ± 3	25 ± 3	1.2 ± 0.5	-	21 ± 3	20 ± 3	1.2 ± 0.5	-
Otani (43)	TEE-3D	mid-systole, end-diastole	25.2 ± 2.8	25.2 ± 2.6	-	-	19.5 ± 2.3	19.2 ± 2.3	-	-
Peng (36)	CT	all: max 0-10%, min 50%	28.2 ± 4.0	27.1 ± 3.7	3.2 ± 1.4	-	23.1 ± 2.6	21.1 ± 2.8	3.6 ± 1.4	-
Pontone (29)	CT	systole, diastole	25.1 ± 2.8	25.4 ± 2.7	-	NS	21.2 ± 2.2	20.1 ± 2.7	-	NS
Shabestari (32)	CT	30-35%, 70-75%	27.2 ± 3.1	27.4 ± 2.6	0.33	-	20.6 ± 2.1	20.5. ± 2.4	0	-
Willson (30)	CT	25-35%, 75%	26.6± 2.8	26.2 ± 2.9	-	0.22	20.8 ± 2.2	20.2 ± 1.99	-	0.01

All annular measurements are presented in millimeters as mean ± standard deviation

* derived from graphs

† distance between basal attachment of left coronary cusp and opposite intercommissure

‡ distance between basal attachment of right coronary cusp and opposite intercommissure

The annular area was evaluated in 18 patient groups using double oblique plane reconstructions (Table 5). The majority (n = 15, 83%) showed the largest area during (early) systole, with a maximal mean difference of 122±33 mm^2 throughout the cardiac cycle. [24] Nine groups were statistically evaluated [16,17,24,29,30,33,35] and the area was significantly larger during systole in seven, during diastole in one and not significantly different in one group. [29] The annular perimeter was largest during systole in five and during diastole in three groups (Table 6). This was tested and significant in four and one patient group, respectively. The largest mean difference between systole and diastole was 5.4±1.5 mm. [35]

Table 5: Double oblique plane annulus area measurements

				Area				
Author	**Imaging**	**Cardiac phase measured**	**Area method**	**Systole**	**Diastole**	**P-value**	**Mean difference**	**P-value**
Patients without aortic valve stenosis								
De Heer (24)	CT	all: max 0-30%, min 50-70%	semi-automatic	NA	NA	-	122 ± 33 (28% ± 10%)	<0.001
Veronesi (16)	TEE-3D	all: max 19%, min 57%	semi-automatic	3.7 ± 1.1*	4.6 ± 1.3*	<0.05	-	-
Hamdan (33)	CT	all: max 30%, min 90-0%	manual	448 ± 81.8	398.7 ± 93.7	<0.001	11.2 ± 5.2%	<0.001
Otani (43)	TEE-3D	mid-systole, end-diastole	manual	391 ± 66	390 ± 65	-	-	-
Shabestari (32)	CT	30-35%, 70-75%	manual	458 ± 82.86	460.24 ± 79.70	-	2.53	-
Tsang (26)	TEE-3D	all: max NA, min NA	semi-automatic	5.3 ± 1.1*	4.2 ± 1.1*	-	-	-
Tsang (15)	TEE-3D	all: max NA, min NA	semi-automatic	5.4 ± 1.0*	4.4 ± 1.2*	-	-	-
Patients with aortic valve stenosis								
De Heer (24)	CT	all: max 0-30%, min 50-70%	semi-automatic	NA	NA	-	98 ± 52 (21 ± 10%)	<0.001

Hamdan (33)	CT	all: max 30%, min 90-0%	manual	480.9 ± 108	438.8 ± 103	<0.001	6.2 ± 4.8%	<0.001
Otani (43)	TEE-3D	mid-systole, end-diastole	manual	397 ± 89	396 ± 88	-	-	-
Shabestari (32)	CT	30-35%, 70-75%	manual	437.82 ± 92.44	438.31 ± 79.25	-	6.92	-
Bertaso (17)	CT	30-40%, 70-80%	ellipse equation	509 ± 12	488 ± 12	-	0.04	0.002
Blanke (35)	CT	all: max 20%, min 60%	manual	483.4 ± 75.2	410.5 ± 68.7	<0.001	72.9 ± 22.6 (18.2%)	<0.001
Masri (42)	CT	all: max NA, min NA	manual	482 ± 111	445 ± 102	-	38 ± 17	-
Pontone (29)	CT	systole, diastole	manual	410.5 ± 81.4	409.2 ± 97.1	NS	-	-
Tsang (26)	TEE-3D	all: max NA, min NA	semi-automatic	4.4 ± 1.4 *	3.8 ± 1.2*	-	-	-
Tsang (15)	TEE-3D	all: max NA, min NA	semi-automatic	5.1 ± 1.1*	3.7 ± 1.7*	-	-	-
Willson (30)	CT	25-35%, 75%	manual	4.7 ± 0.8*	4.5 ± 0.9*	<0.001	-	-

Measurements are presented in mm^2 or in cm^2 if indicated with* as mean ± standard deviation
NA= not available; NS= not significant

Table 6: Double oblique plane annulus perimeter measurements

			Perimeter			
Author	**Imaging**	**Cardiac phase measured**	**Systole**	**Diastole**	**Mean difference**	**P-value**
Patients without aortic valve stenosis						
Hamdan (33)	CT	all: max 30%, min 90-0%	76.1 ± 6.7	74.1 ± 7.6	2.2 ± 2.2	0.01
Shabestari (32)	CT	30-35%, 70-75%	86.64 ± 7.40	88.12 ± 8.90	1.48	-
Veronesi (16)	TEE-3D	all: max 19%, min 57%	69.5 ± 10.6	78.1 ± 11.5	-	<0.05
Patients with aortic valve stenosis						
Blanke (35)	CT	all: max 20%, min 60%	79.6 ± 6.0	74.2 ± 5.7	5.4 ± 1.5 (7.3 ± 2.1%)	<0.001
Hamdan (33)	CT	all: max 30%, min 90-0%	78.9 ± 8.7	77.3 ± 8.6	0.56 ± 0.85	0.01
Masri (42)	CT	all: max NA, min NA	80 ± 9	77 ± 9	3 ± 1	-
Shabestari (32)	CT	30-35%, 70-75%	86.67 ± 8.52	87.51 ± 8.21	-	-
Willson (30)	CT	25-35%, 75%	78.5 ± 8.2	77.2 ± 8.0	-	0.01

All measurements are presented in millimeters as mean ± standard deviation

NA= not available

AS vs. non-stenosis

As presented in Tables 3–6, both non-AS patients (e.g. without aortic root disease) and AS patients showed significant annular change throughout the cycle. Five studies directly compared the extent of conformational change between AS and non-AS patients. Based on longitudinal parasternal view measurements, Shiran et al. found similar results for AS and non-AS patients. In contrast, Yoshikawa et al. detected significantly less absolute and relative diameter change in AS patients ($P \leq 0.0027$). [23] Furthermore, the diameter reached its maximal value at a later point in the cardiac cycle than in non-AS patients (99 vs. 83 ms from the R-wave, resp. $P < 0.0004$). Using double oblique plane images, Izumi et al. also found a significantly smaller annulus diameter deformation in AS patients (2 vs. 8% in controls, $P < 0.0001$). [22] In the study of Hamdan et al., AS patients showed higher annular stiffness compared with healthy subjects, based on the perimeter and left ventricular pressure change (23 vs. 14 MPA, resp.

P = 0.029). [33] No significant difference was found for dynamic changes between patients with and without aortic valve calcifications. [32]

Other factors

Aortic root calcifications in general did not show a correlation with annular change [32] or circularity [28] during the cardiac cycle. But the location of the calcifications was related to annulus area change, showing the least change with both annular and commissural calcifications (6 mm^2) and the greatest change with only commissural calcifications (23 mm^2). [32] Only one study evaluated the influence of age on annulus change within the cardiac cycle but found no age effect. [32] In this study, a weak linear correlation was found between diastolic blood pressure and annulus perimeter changes (r = 20.25, P = 0.01), and between ejection fraction and minimal diameter changes (r = 20.22, P = 0.03). Another study found the left ventricular outflow tract diameter and stroke volume to be associated with larger changes throughout the cycle. [36]

Impact on prosthesis sizing

Blanke et al. evaluated the annulus in 5% steps throughout the full cardiac cycle and found the selected cardiac phase to affect prosthesis agreement. [35] Selection of the cardiac phase in which the area or perimeter-derived diameter reached its maximal value showed the highest agreement with the selected Edwards Sapien prosthesis and most relative oversizing (±10%). The area and perimeter were largest between 0 and 30% phases of the RR-interval. Measurements obtained in the clinically used 35%-systolic and 75%-diastolic cardiac phase showed only 76% prosthesis agreement (84/110 patients) and less relative oversizing (±7 and±5%, resp.). [35] In particular, 75%-diastolic phase area and diameter measurements led to (theoretical) undersizing in 15 (14%) and 6 (6%) patients. In this phase, the area and perimeter-derived diameters differed 2.7±1.4 and 2.0±1.1 mm with the prosthesis compared with 1.5±1.2 and 1.1±1.2 mm during maximal phase measurements, respectively. Likewise, Wilsson et al. found diastolic phase measurements to result in smaller Sapien XT prostheses in 13/66 patients and in larger in only 1/66 patients. [30] The patients with downsized prostheses showed significantly larger conformational change in annulus diameter, area and perimeter compared with patients without a switch in prosthesis size. In contrast, the use of the diastolic diameter in another study resulted in a larger prosthesis in 2/34 patients (29 vs. 26 mm Corevalve). [17] Some patients might show the largest area in the diastolic phase, as also found by de Heer et al. [24] in 3/15 patients.

Discussion

This systematic review clearly demonstrates that the aortic annulus does undergo dynamic conformational change during the cardiac cycle. The annulus becomes more circular in systole and has a predominantly oval shape in diastole. Using double oblique reconstructions perpendicular to the centre lumen line of the left ventricular outflow tract the annulus has a significantly larger short-axis diameter, area, and perimeter in systole compared with diastole. A greater diameter is also found in systolic compared with diastolic phase on the parasternal long-axis and sagittal views, though each was statistically confirmed only by one study. In contrast, the double oblique long-axis diameter suggests no significant change throughout the cardiac cycle and the same goes for the coronal diameter.

Results on differences for the magnitude of conformational changes between AS and non-AS patients are contradictory.

The finding that the aortic annulus undergoes conformational changes during the cardiac cycle is important and may add to improved prosthesis design. In clinical setting, this knowledge may add in selecting the optimal imaging phase and approximating the true annular dimensions. Blanke et al. showed better annular agreement with prosthetic sizes selected based on the maximal annular values throughout the cardiac cycle compared with prostheses based on routine predefined systolic (35%) or diastolic (75%) reconstructions. [35] Importantly, de Heer et al. found the cardiac phase for maximal annulus area to vary between patients from 0–60 and 90% of the RR-interval and similar differences exist for the minimal area. [24] Apparently, the systolic phase does not represent the aortic annulus in its maximal dimensions in all patients. This might also be one of the reasons why some studies found larger diastolic diameters and/or no significant differences in the overall patient group. Assessment of the full cardiac cycle hence enables selection of the annulus in its ultimate dimensions, which may improve the annulus to prosthesis agreement.

Likewise, the choice of the measured parameter may affect prosthesis size selection as well since the annulus, in general, is an ellipsoid structure. The results show the minimal short diameter axis to significantly change in dimension, whereas the maximal diameter remains relatively unchanged. In addition, the perimeter changes throughout the cardiac cycle as well. These findings support the belief that the annular structure becomes less oval throughout the cycle. Studies using a so-called effective diameter, the diameter calculated from the measured area or perimeter, may induce an error if solely formulas for circular structures are applied. Evaluation of multiple parameters may be desirable in

specific patients, for instance, in patients whose annular dimensions are in the overlapping/border zone prosthesis size recommendations. Multiphase assessment providing knowledge on the amount of annular distensibility may also be helpful in choosing the most optimal size in these patients.

Furthermore, the change in dimensions of the aortic annulus seems to urge the use of three-dimensional techniques for accurate annulus size assessment. An advantage of CT is that it provides an overview of the cardiac anatomy and calcifications present which may impact prosthesis size selection in border zone patients.[37] TEE might be a helpful three-dimensional modality in patients not eligible for contrast-enhanced CT imaging. [37 – 39] However, compared with CT measurements 3D-TEE consistently displayed smaller dimensions, which may cause significant undersizing. [38,39] Two-dimensional TEE showed even more undersizing compared with CT-based sizing.[39] Hence, the use of three-dimensional imaging modalities and CT in particular seems indispensable to reduce potential sizing error.

Patient post-procedural outcome has often been related to the presence of relevant paravalvular regurgitation, although the direct association with mortality yet needs to be evaluated.[40] One of the key factors in paravalvular regurgitation is the relation with prosthesis oversizing and undersizing. [28,30,41] The purpose of this review was to assess whether the aortic annulus undergoes significant dynamic change and its possible implications for prosthesis size selection. Currently, TAVI prostheses are available in four sizes (23, 26, 29, and 31 mm) for annular sizes of 18–29 mm and the prosthesis size recommendations overlap for annulus dimensions.

Results showed the systolic short-axis diameter to differ significantly by (mean) 0.75 mm minimum [17] to 2.7±1.6 mm maximum [33] from the diastolic diameter. Maximal differences within the cycle ranged to even 8.7 mm in Peng et al. [36] With little annular change, the impact on TAVI sizing may be small as was the case in the study of Bertaso et al.. [17]With greater annular deformations, diastolic sizing can lead to a relevant change in prosthetic size selection, as 20% of patients in the study of Willson et al. received a smaller prosthesis. [30] The conformational change of the annulus showed to impact the annulus to prosthesis agreement, [35] consequently it also may result in (undesired) oversizing or undersizing and thus in paravalvular leakage. Remarkably, one study found significantly less conformational change of the annulus in patients with clinically relevant paravalvular leakage, showing a mean area deformation of 32±10 vs. 46± 21 mm^2 (P = 0.003) in non-leakage patients and perimeter deformation of 2.6±0.8 vs. 3.6±1.3 mm (P = 0.001), respectively. [42] For paravalvular leakage prediction, the same study showed 74% sensitivity and 72% specificity for conformational changes of

<3 mm in annular perimeter. Prosthesis to annular perimeter size ratio and annular calcifications were also independent predictors for paravalvular leakage.

As shown in this review, results vary remarkably between specific studies. The reported mean percentage change ranges from 4 to 28% for area, 2–12% for minimal diameter and 0.56–7.3% perimeter. Evidently, the heterogeneity between studies is substantial and likely accounts for the observed ranges. Significant differences are present for both study methods and patient characteristics. With regard to the first, study sample size and imaging modality may affect study results just like the assessment of two predefined vs. all cardiac phases and manual vs. semi-automatic measurements. Second, patient age, gender, and degree and/or definition of stenosis differ between studies. The impact of gender on the amount of conformational change has not been evaluated and only one study reported on the effect of age without significant differences. No consensus exists on whether the annular conformational changes vary between AS patients and non-AS patients. Furthermore, patients with aortic root calcifications in general did not show significant differences with the control group, whereas significant differences were found for annular area related to the distribution of calcifications. [32] More research and larger study samples are needed to provide basic insight on various potential factors affecting the annular distensibility and conformational changes. As for TAVI sizing and patient outcome, it is essential to take the dynamic deformation into consideration by selecting the optimal imaging modality, cardiac phase, and annular parameter. Based on this review, we can conclude that three-dimensional imaging is required for adequate annulus assessment. Despite its well-known drawbacks, CT provides the most comprehensive overview of cardiac structures and optimal imaging plane reconstructions and hence allows for reliable assessment of all annular dimensions. The use of two-dimensional imaging modalities on the other hand may lead to relevant prosthesis undersizing. Furthermore, selection of the cardiac phase in which the annulus shows the largest dimensions seems to prevent (theoretical) prosthesis undersizing, but the maximal phase is patient specific. Future studies are required to evaluate the effect of the use of different annular parameters on patient outcome and to prospectively assess the clinical impact of sizing based on different cardiac phases.

Limitations

In this study, we did not take the effect of semi-automatic or manual measurements into account. Secondly, variability in the definition of annulus might impact study results, although the majority of included studies (76%) used the same definition. Thirdly, published results lack data on paired intra-

patient analyses to be able to assess differences on patient level. Lumping the mean overall systolic and diastolic diameters reported will not provide the mean difference within patients. Hence, insufficient data were available to perform a meta-analysis to acquire the pooled difference for mean change of the annulus within the cardiac cycle. Finally, evaluation of the accuracy of annulus measurements using different imaging modalities in comparison with true intra-operative measurements was beyond the scope of this review.

References

1. Go AS, Mozaffarian D, Roger VL, Benjamin EJ, Berry JD, Blaha MJ et al. Heart diseaseand stroke statistics – 2014 update: a report from the american heart association. Circulation 2014;129:e28–e292.

2. Bach DS. Prevalence and characteristics of unoperated patients with severe aortic stenosis. J Heart Valve Dis 2011;20:284–91.

3. Kodali SK, Williams MR, Smith CR, Svensson LG,Webb JG, Makkar RR et al. Two year outcomes after transcatheter or surgical aortic-valve replacement. N Engl J Med 2012;366:1686–95.

4. Toggweiler S, Humphries KH, Lee M, Binder RK, Moss RR, Freeman M et al. 5-year outcome after transcatheter aortic valve implantation. J Am Coll Cardiol 2013;61: 413–9.

5. Jerez-Valero M, Urena M, Webb JG, Tamburino C, Munoz-Garcia AJ, Cheema A et al. Clinical impact of aortic regurgitation after transcatheter aortic valve replacement: insights into the degree and acuteness of presentation. JACC Cardiovasc Interv 2014;7:1022–32.

6. Chrysohoou C, Hayek SS, Spilias N, Lerakis S. Echocardiographic and clinical factors related to paravalvular leak incidence in low-gradient severe aortic stenosis patients post-transcatheter aortic valve implantation. Eur Heart J Cardiovasc Imaging 2015;16:558–63.

7. O'Sullivan KE, Gough A, Segurado R, Barry M, Sugrue D, Hurley J. Is valve choice a significant determinant of paravalular leak post-transcatheter aortic valve implantation? A systematic review and meta-analysis. Eur J Cardiothorac Surg 2014;45: 826–33.

8. Tops LF, Wood DA, Delgado V, Schuijf JD, Mayo JR, Pasupati S et al. Noninvasive evaluation of the aortic root with multislice computed tomography implications for transcatheter aortic valve replacement. JACC Cardiovasc Imaging 2008;1:321–30.

9. Messika-Zeitoun D, Serfaty JM, Brochet E, Ducrocq G, Lepage L, Detaint D et al. Multimodal assessment of the aortic annulus diameter: Implications for transcatheter aortic valve implantation. J Am Coll Cardiol 2010;55:186–94.

10. de Heer LM, Budde RP, Mali WP, de Vos AM, van Herwerden LA, Kluin J. Aortic root dimension changes during systole and diastole: Evaluation with ecg-gated multidetector row computed tomography. Int J Cardiovasc Imaging 2011;27:1195–204.

11. Albano AJ, Mitchell E, Pape LA. Standardizing the method of measuring by echocardiogram the diameter of the ascending aorta in patients with a bicuspid aortic valve. Am J Cardiol 2010;105:1000–4.

12. van Prehn J, Vincken KL, Muhs BE, Barwegen GK, Bartels LW, Prokop M et al. Toward endografting of the ascending aorta: insight into dynamics using dynamic cine-cta. J Endovasc Ther 2007;14:551–60.

13. De Paulis R, De Matteis GM, Nardi P, Scaffa R, Buratta MM, Chiariello L. Opening and closing characteristics of the aortic valve after valve-sparing procedures using a new aortic root conduit. Ann Thorac Surg 2001;72:487–94.

14. Shiran A, Adawi S, Ganaeem M, Asmer E. Accuracy and reproducibility of left ventricular outflow tract diameter measurement using transthoracic when compared with transesophageal echocardiography in systole and diastole. Eur J Echocardiogr 2009;10:319–24.

15. Tsang W, Veronesi F, Sugeng L,Weinert L, Takeuchi M, Jeevanandam V et al. Mitral valve dynamics in severe aortic stenosis before and after aortic valve replacement. J Am Soc Echocardiogr 2013;26:606–14.

16. Veronesi F, Corsi C, Sugeng L, Mor-Avi V, Caiani EG, Weinert L et al. A study of functional anatomy of aortic-mitral valve coupling using 3d matrix transesophageal echocardiography. Circ Cardiovasc Imaging 2009;2:24–31.

17. Bertaso AG, Wong DT, Liew GY, Cunnington MS, Richardson JD, Thomson VS et al. Aortic annulus dimension assessment by computed tomography for transcatheter aortic valve implantation: Differences between systole and diastole. Int J Cardiovasc Imaging 2012;28:2091–8.

18. Burman ED, Keegan J, Kilner PJ. Aortic root measurement by cardiovascular magnetic resonance: Specification of planes and lines of measurement and corresponding normal values. Circ Cardiovasc Imaging 2008;1:104–13.

19. Wood DA, Tops LF, Mayo JR, Pasupati S, Schalij MJ, Humphries K et al. Role of multislice computed tomography in transcatheter aortic valve replacement. Am J Cardiol 2009;103:1295–301.

20. Kazui T, Izumoto H, Yoshioka K, Kawazoe K. Dynamic morphologic changes in the normal aortic annulus during systole and diastole. J Heart Valve Dis 2006;15: 617–21.

21. Zhu D, Zhao Q. Dynamic normal aortic root diameters: implications for aortic root reconstruction. Ann Thorac Surg 2011;91:485–9.

22. Izumi C, Miyake M, Takahashi S, Hayashi H, Miyanishi T, Matsutani H et al. Usefulness of real-time three-dimensional echocardiography in evaluating aortic root diameters during a cardiac cycle. J Echocardiogr 2012;10:8–14.

23. Yoshikawa H, Suzuki M, Hashimoto G, Kusunose Y, Otsuka T, Hara H et al. Assessment of cyclic changes in the diameter of the aortic annulus using speckle-tracking trans-esophageal echocardiography. Ultrasound Med Biol 2013;39:2084–90.

24. de Heer LM, Budde RP, van Prehn J, Mali WP, Bartels LW, Stella PR et al. Pulsatile distention of the nondiseased and stenotic aortic valve annulus: analysis with electrocardiogram-gated computed tomography. Ann Thorac Surg 2012;93:516–22.

25. Jilaihawi H, Kashif M, Fontana G, Furugen A, Shiota T, Friede G et al. Cross-sectional computed tomographic assessment improves accuracy of aortic annular sizing for transcatheter aortic valve replacement and reduces the incidence of paravalvular aortic regurgitation. J Am Coll Cardiol 2012;59:1275–86.

26. Tsang W, Meineri M, Hahn RT, Veronesi F, Shah AP, Osten M et al. A threedimensional echocardiographic study on aortic-mitral coupling in transcatheter aortic valve replacement. Eur Heart J Cardiovasc Imaging 2013;14:950–6.

27. Bolen MA, Popovic ZB, Dahiya A, Kapadia SR, Tuzcu EM, Flamm SD et al. Prospective ecg-triggered, axial 4-D imaging of the aortic root, valvular, and left ventricular structures: a lower radiation dose option for preprocedural TAVR imaging. J Cardiovasc Comput Tomogr 2012;6:393–8.

28. Lehmkuhl L, Foldyna B, Von Aspern K, Lucke C, Grothoff M, Nitzsche S et al. Interindividual variance and cardiac cycle dependency of aortic root dimensions and shape as assessed by ecg-gated

multi-slice computed tomography in patients with severe aortic stenosis prior to transcatheter aortic valve implantation: Is it crucial for correct sizing? Int J Cardiovasc Imaging 2013;29:693–703.

29. Pontone G, Andreini D, Bartorelli AL, Annoni A, Mushtaq S, Bertella E et al. Feasibility and accuracy of a comprehensive multidetector computed tomography acquisition for patients referred for balloon-expandable transcatheter aortic valve implantation. Am Heart J 2011;161:1106–13.

30. Willson AB, Webb JG, Freeman M, Wood DA, Gurvitch R, Thompson CR et al. Computed tomography-based sizing recommendations for transcatheter aortic valve replacement with balloon-expandable valves: Comparison with transesophageal echocardiography and rationale for implementation in a prospective trial. J Cardiovasc Comput Tomogr 2012;6:406–14.

31. Martin R, Hascoet S, Dulac Y, Peyre M, Mejean S, Hadeed K et al. Comparison of two- and three-dimensional transthoracic echocardiography for measurement of aortic annulus diameter in children. Arch Cardiovasc Dis 2013;106:492–500.

32. Shabestari A, Pourghorban R, Tehrai M, Pouraliakbar H, Faghihi Langroudi T, Bakhshandeh H et al. Comparison of aortic root dimension changes during cardiac cycle between the patients with and without aortic valve calcification using ecg-gated 64-slice and dual-source 256-slice computed tomography scanners: Results of a multicenter study. Int J Cardiovasc Imaging 2013;29:1391–400.

33. Hamdan A, Guetta V, Konen E, Goitein O, Segev A, Raanani E et al. Deformation dynamics and mechanical properties of the aortic annulus by 4-dimensional computed tomography: insights into the functional anatomy of the aortic valve complex and implications for transcatheter aortic valve therapy. J Am Coll Cardiol 2012;59: 119–27.

34. Lehmkuhl LH, von Aspern K, Foldyna B, Grothoff M, Nitzsche S, Kempfert J et al. Comparison of aortic root measurements in patients undergoing transapical aortic valve implantation (TA-AVI) using

three-dimensional rotational angiography (3D-RA) and multislice computed tomography (MSCT): Differences and variability. Int J Cardiovasc Imaging 2013;29:417–24.

35. Blanke P, Russe M, Leipsic J, Reinohl J, Ebersberger U, Suranyi P et al. Conformational pulsatile changes of the aortic annulus: impact on prosthesis sizing by computed tomography for transcatheter aortic valve replacement. JACC Cardiovasc Interv 2012; 5:984–94.

36. Peng LQ, Yang ZG, Yu JQ, Chu ZG, DengW, Shao H. Dynamic assessment of aortic annulus in patients with aortic stenosis throughout cardiac cycle with dualsource computed tomography. Int J Cardiol 2012;158:304–7. 37. Husser O, Holzamer A, Resch M, Endemann DH, Nunez J, Bodi V et al. Prosthesis sizing for transcatheter aortic valve implantation – comparison of three dimensional transesophageal echocardiography with multislice computed tomography. Int J Cardiol 2013;168:3431–8.

38. Jilaihawi H, Doctor N, Kashif M, Chakravarty T, Rafique A, Makar M et al. Aortic annular sizing for transcatheter aortic valve replacement using cross-sectional 3-dimensional transesophageal echocardiography. J Am Coll Cardiol 2013;61:908–16.

39. Ng AC, Delgado V, van der Kley F, Shanks M, van de Veire NR, Bertini M et al. Comparison of aortic root dimensions and geometries before and after transcatheter aortic valve implantation by 2- and 3-dimensional transesophageal echocardiography and multislice computed tomography. Circ Cardiovasc Imaging 2010;3:94–102.

40. Genereux P, Head SJ, Hahn R, Daneault B, Kodali S, Williams MR et al. Paravalvular leak after transcatheter aortic valve replacement: The new achilles' heel? A comprehensive review of the literature. J Am Coll Cardiol 2013;61:1125–36.

41. Willson AB, Webb JG, Labounty TM, Achenbach S, Moss R, Wheeler M et al. 3-dimensional aortic annular assessment by multidetector computed tomography predicts moderate or severe paravalvular regurgitation after transcatheter aortic valve replacement: a multicenter retrospective analysis. J Am Coll Cardiol 2012;59: 1287–94.

42. Masri A, Schoenhagen P, Svensson L, Kapadia SR, Griffin BP, Tuzcu EM et al. Dynamic characterization of aortic annulus geometry and morphology with multimodality imaging: Predictive value for aortic regurgitation after transcatheter aortic valve replacement. J Thorac Cardiovasc Surg 2014;147:1847–54.

43. Otani K, Takeuchi M, Kaku K, Sugeng L, Yoshitani H, Haruki N et al. Assessment of the aortic root using real-time 3D transesophageal echocardiography. Circ J 2010; 74:2649–57.

44. Kempfert J, Van Linden A, Lehmkuhl L, Rastan AJ, Holzhey D, Blumenstein J et al. Aortic annulus sizing: echocardiographic versus computed tomography derived measurements in comparison with direct surgical sizing. Eur J Cardiothorac Surg 2012;42:627–33.

Appendix

Search strategy performed in PubMed[a] and Embase[b] on 25 June 2014

1 Imaging OR CT OR CTs OR ‘computer tomography’ OR ‘computed tomography’ OR ‘computerized tomography’ OR ‘CAT scan’ OR ‘CAT scans’ OR MDCT OR MSCT OR CTA OR ‘computer-assisted tomography’ OR ‘computed-assisted tomography’ OR ‘magnetic resonance imaging’ OR ‘magnetic resonance’ OR MRI OR MR OR NMR OR NMRI OR CMR OR echocardiographies OR

echocardiography OR TTE OR TEE OR ultrasound OR ultrasonographies OR ultrasonography OR ultrasonic OR echography OR echographies OR echotomography OR echotomographies

2 ‘aortic annulus’ OR ‘aortic annular’ OR ‘aortic root’ OR TAVI OR TAVR OR ‘transcatheter valve’ OR ‘percutaneous valve’ OR ‘transcatheter aortic valve’ OR ‘percutaneous aortic valve’

3 (1 and 2)

a; In title/abstract.

b: In title/abstract: no conference abstract, letter, note, or editorial.

Chapter 9 Samenvatting

Computertomografie (CT) is een van de meest prominente beeldvormingsmodaliteiten in de klinische praktijk en klinisch onderzoek. In dit proefschrift worden verschillende toepassingen van CT, waaronder 3D-modellering, chirurgische planning en diagnose, gepresenteerd met als focus coronaire hartziekte (Coronary Artery Disease = CAD) en de aortastenose. Het proefschrift is verdeeld in twee hoofdonderdelen, namelijk 1) Coronaire morfologie en plaque, 2) Aortaklepmeting.

Deel 1 Coronair Morfologie en Plaque

Deel 1 bevat drie originele studies, waarvan twee onderling verband houden met elkaar. In deze studies is gekeken naar de relatie tussen de geometrie van de kransslagaders en CAD. In de eerste studie (hoofdstuk 2) werden alleen gegevens uit 1 fase van de hartcyclus (eind diastolische fase) gebruikt, terwijl de andere studie (hoofdstuk 3) werd uitgevoerd met gegevens uit zowel de eind-systolische als de eind-diastolische fase. In beide onderzoeken waren kromming en kronkeligheid (turtuositeit) de gebruikte geometrische maten, die werden bepaald met behulp van een semiautomatisch gegenereerde middellijn op de coronaire CT-beelden. De metingen zijn uitgevoerd op vat- en segmentniveau. De kransslagadersegmenten werden bepaald op basis van de 15-segment classificatie van de American Heart Association. De statische studie (Hoofdstuk 2) toonde aan dat kromming kan worden geassocieerd met significante stenose en aanwezigheid zowel op segment- als slagaderniveau, terwijl tortuositeit alleen op segmentniveau geassocieerd kan worden met significante stenose en aanwezigheid van plaque. Deze studie toonde aan dat op CT-gebaseerde metingen van de kransslagadergeometrie verband houden met de aanwezigheid van plaque en significante stenose, waardoor een vroege risicobeoordeling mogelijk is. De relatie tussen dynamische veranderingen van de coronaire arterie-geometrie en CAD eveneens op basis van CT-beelden (n = 71) werd onderzocht in Hoofdstuk 3. In deze studie werd het aantal buigpunten gemeten naast kromming en tortuositeit als een van de geometrische kenmerken. De metingen werden uitgevoerd in de systolische en diastolische fasen van de hartcyclus, die waren gebaseerd op, respectievelijk, de minimale en maximale vulling van de linker hartkamer. Er was geen significant verband tussen de verandering in geometrische parameters door de hartcyclus en de ernst van CAD.

Het laatste onderzoek (Hoofdstuk 4) van dit deel heeft tot doel een algoritme te ontwerpen en valideren om de invloed van lumencontrast op niet-verkalkte atherosclerotische plaque Hounsfield-Unit (HU) - waarden in CT-beelden te corrigeren om zo CT-beelden te verkrijgen met de juiste HU-waarden voor de karakterisering en kwantificering van niet-verkalkte plaques. Voor dit doel zijn speciaal ontworpen coronaire vatfantomen gebruikt met ronde, holle lumina met een diameter van 1, 2 en 4 mm. De fantomen werden in olie gescand met behulp van een dual-source CT-scanner met zowel vaten met als zonder plaque in de vaatwant. De scan werd na een scan zonder contrast middel herhaald met vullingen van verschillende verdunningen van contrastmiddel met water (corresponderend met 100-400HU, met een interval van 100HU). Pixel voor pixel vergelijking van contrastversterkte en niet-contrastversterkte beelden bevestigde het eerder vastgestelde exponentiële vervalpatroon van de HU op de wand veroorzaakt door het contrastmiddel. Op basis van dat patroon is een correctiealgoritme opgesteld dat werd toegepast op de beelden met contrast. Het algoritme corrigeert voor de invloed van het contrastmiddel op het meest aangedane wandgebied, dat zich binnen een straal van 2 pixels vanaf de lumengrens bevindt, waardoor het mediane verschil van 45 HU wordt teruggebracht tot een verschil van 4 HU. Deze correctie maakt een nauwkeurigere bepaling van de vaatwandsamenstelling mogelijk.

Deel 2 Aorta Klepmeting

In dit deel worden vier onderzoeken gepresenteerd. De eerste twee hebben betrekking op het modelleren van hartklepaandoeningen.

In een systematische review werden de toepassingsgebieden van 3D-printen in de hartklepvervangingsprocedures in kaart gebracht (Hoofdstuk 5). Verder zijn parameters als voorbewerking, printmaterialen, printtechnieken, en tijdsdruk onderzocht. Uit het systematisch literatuuronderzoek bleek dat CT de meest gebruikelijke beeldvormende techniek is voor 3D printing toepassingen. Acrylonitrile Butadiene Styrene (ABS) en StereoLithography zijn, respectievelijk, de meest voorkomende 3D-printmaterialen en printtechnieken. Twee belangrijke problemen bij deze techniek zijn het verschil in grootte tussen het 3D-geprinte model en de werkelijke grootte van het gescande object, en het verwijderen van de ondersteunende materialen van de 3D print. Als klinische toepassingen van 3D-printen werden vermeld: 1) het creëren van trainingsmodellen, 2) preoperatieve planning en 3) testen van apparatuur.

De tweede studie in dit deel beschrijft het ontwerp en de validatie van een pulserende pomp en een nep-bloedsomloop, voor gebruik in de validatie van software, en medische apparatuur (Hoofdstuk 6). De

fantoomopstelling is gevalideerd door het tijdens het pompen te scannen met een Siemens Sensation 64 MDCT scanner. De test was succesvol voor een slagvolume van 68 ml bij een frequentie van 70 slagen per minuut. De pomp produceert een realistische pulserend stroomprofiel en het nep-circulatiesysteem geeft een goede representatie van de bloedcirculatie.

De laatste twee onderzoeken hadden meer betrekking op de klinische praktijk. Een van deze studies behelst het ontwerp en de validatie van een snelle en robuuste semi-automatische segmentatietool om het aortaklepgebied (AVA) op CT-beelden te segmenteren (Hoofdstuk 7). Om het algoritme te valideren, is de AVA door twee waarnemers handmatig en semi-automatisch gesegmenteerd op 25 CT-beelden. De metingen werden vervolgens vergeleken met als gouden standaard de op echocardiografie gebaseerde resultaten van dezelfde patiënten. Deze resultaten toonden aan dat het ontwikkelde algoritme een snelle, nauwkeurige en robuuste manier biedt om AVA te kwantificeren.

Hoofdstuk 8 is een systematische review waarin de vraag wordt gesteld: 'Ondergaat de aorta annulus tijdens de hartcyclus relevante vorm veranderingen?'. Dit is een belangrijke vraag, aangezien de grootte van de aorta-annulus de belangrijkste maat is voor het bepalen van grootte van een implantaat dat zal worden gebruikt in de minimaal invasieve transcatheter-aortaklepimplantatie (TAVI) -procedures. Fouten bij de selectie van de prothese kunnen leiden tot aortaklepinsufficiëntie of scheuring van de aortawortel. Uit het systematisch literatuuronderzoek bleek dat de aorta-annulus ronder is in de systole en overwegend ovaal in de diastole. De ringvormige diameter van de lange as vertoonde een niet-significante verandering gedurende de cyclus, terwijl de diameter, het oppervlak en de omtrek van de korte as significant groter waren in systole vergeleken met diastole. Deze resultaten suggereren dat de aorta-annulus tijdens de hartcyclus dynamische veranderingen doormaakt en dat meerfasige aorta-annulusmetingen van groot belang zijn voor TAVI-planning om onder- of overschatting van de maatvoering van de prothese te voorkomen.

Conclusie

Door de niet-invasieve aard en verbeterde temporele resolutie van CT kunnen nieuwe risicofactoren, zoals vaatgeometrie, worden onderzocht om hart- en vaatziekten te voorspellen. Het is tevens de belangrijkste medische beeldbron voor het 3D-printen van fysieke anatomische modellen, die kunnen worden gebruikt bij medische training, preoperatieve planning en het testen van apparatuur. Naast de statische 3D-gegevens bieden de dynamische 4D CT-gegevens uitgebreidere informatie om onder- of

overschatting van de maatvoering van de prothese te voorkomen om de uitkomst van de minimaal invasieve cardiovasculaire procedures te maximaliseren.

Kortom, CT is de dominante 3D-beeldvormingsmodaliteit, die de klinische besluitvorming ondersteunt in de verschillende stadia van therapeutisch beheer van hart- en vaatziekten, van vroege risicobepaling tot diagnose en chirurgische planning.

Chapter 10 Summary

Computed Tomography (CT) is one of the most prominent imaging modalities in clinical practice and clinical research. In this thesis various applications of CT. including 3D modeling, surgical planning, and diagnosis. are presented. The focus was on coronary artery disease (CAD) and the aortic stenosis. It was separated in to two main parts namely 1) Coronary Morphology and Plaque, 2) Aortic Valve Measurement.

Part 1 Coronary Morphology and Plaque

Part 1 includes three original research study two of which are related to each other. In these studies, the relationship between the coronary artery geometry and the CAD were investigated. In the first study (Chapter 2) only data from one phase (end-diastolic phase) were used, while the other study (Chapter 3) was conducted with data from both end-systolic and end-diastolic phases. In both studies, curvature and tortuosity were the common geometric metrics, which were quantified using a semi automatically generated centerline on the coronary CT images. The measurements were done at artery and segment level. The coronary artery segments were determined based on the 15-segment modified American Heart Association classification. The static study (Chapter 2) showed that curvature was associated with significant stenosis and presence both at segment and artery level while tortuosity was associated with significant stenosis and presence of plaque only at segment level. This study showed that CT based coronary artery geometry measurements are related to the presence of plaque and significant stenosis, which may allow early risk assessment. The dynamic study (Chapter 3) investigated the relationship between dynamic changes of coronary artery geometry and CAD using again CT images (n=71). In this study, number of inflection points were measured in addition to curvature and tortuosity as one of geometric metric. The measurements were done at end systolic and end diastolic phases of the cardiac cycle, which were based on the minimum and maximum filling of the left ventricle respectively. In this study (Chapter 3), there was no significant association between the change in geometric parameters through the cardiac cycle, and severity of CAD. The last study (Chapter 4) of this part is an image processing study aimed to construct and validate an algorithm to correct the influence of lumen contrast enhancement on non-calcified atherosclerotic plaque Hounsfield-Unit (HU) values in CT images in order to obtain the correct HU values for the characterization and quantification of non-calcified plaques. For this purpose, firstly specifically designed coronary vessel phantoms (with 1, 2, and 4 mm

diameter circular hollow lumina); with normal and plaque-infested walls were scanned simultaneously in oil using a dual-source CT scanner. The scan was repeated with water and contrast agent (100-400HU, at 100HU interval) fillings. Pixel by pixel comparison of contrast enhanced and non-contrast enhanced images confirmed the previously determined exponential decline pattern of HU on the lumen wall caused by the contrast agent. Based on that pattern a correction algorithm was formulated. The algorithm was applied to the contrast enhanced images. Algorithm corrected the lumen contrast-enhancement influence on the most affected wall region, which is within a 2-pixel radius from the lumen border, reducing the median difference of 45 HU to a median difference of 4 HU. This correction enables a more accurate determination of vessel wall composition.

Part 2 Aortic Valve Measurement

In this part, four studies were presented. First two studies were related to modeling and experimenting in the field of valvular diseases. The first study (Chapter 4) is a systematic review investigating the application areas of 3D printing in the heart valve replacement procedures. This study further investigated the source data and pre-processing, printing materials, printing techniques, the time constraints, and the other 3D printing issues. The systematic literature search revealed that CT is the most common imaging technique to provide medical image data to create the medical image data. Whereas, Acrylonitrile Butadiene Styrene and StereoLithography are the most common 3D printing material and printing techniques respectively. Two major issues reported in these studies are difference in size between the 3D printed model and real-life size of the object 3D printed, and removal of the support materials. The clinical applications of the 3D printing were listed as 1) creating training models, 2) Pre-operative planning and, 3) Device testing.

The second study in this part was describing the design and validation of a pulsatile pump and a mock circulatory system, which was planned to be used in the software, and medical device validation (Chapter 6). The phantom set up was validated with an experiment using a Siemens Sensation 64 MDCT scanner. The test was successful for a stroke volume of 68 ml and 70 beats per minute. The pump produces a realistic pulsatile flow and the mock circulatory system can mimic the blood circulation in the circulatory system.

The last two studies were more related to clinical practice. One of these studies is an original research study on design and validation of a fast and robust semi-automatic segmentation tool to delineate the aortic valve area (AVA) on CT images (Chapter 7). In order to validate the algorithm two observers

manually and semi-automatically segmented AVA on 25 CT images. The measurements were then compared to the gold standard echocardiography-based results of the same patients. These results showed that the developed algorithm provides fast, accurate, and robust way of quantifying AVA. Chapter 8 is a systematic review asking the question "Does the aortic annulus undergo conformational change throughout the cardiac cycle?". This is an important question as the aortic annulus size is the main metric to determine the size of an implant that will be used in the minimally invasive Trascatheter Aortic Valve Implantation (TAVI) procedures. Mistakes made in prosthesis selection may lead to aortic regurgitation or rupture of the aortic root. The systematic literature search revealed that the aortic annulus was more circular in systole and predominantly oval in diastole. The annular long-axis diameter showed insignificant change throughout the cycle, while the short-axis diameter, area, and perimeter were significantly larger in systole compared with diastole. These results suggest that the aortic annulus goes in to dynamic changes throughout the cardiac cycle and multi-phase aortic annulus measurements have utmost importance for TAVI planning in order to prevent under or over sizing of the prosthesis.

Conclusion

The non-invasive nature and improved temporal resolution of CT allows exploring new risk factors such as vessel geometry to predict the cardiovascular diseases. Moreover, it is the main medical image source for 3D printing of physical anatomical models, which can be used in medical training, pre-operative planning, and device testing. In addition to the static 3D data, the dynamic 4D CT data provides more comprehensive information to prevent under or over sizing of the prosthesis to maximize the outcome of the minimally invasive cardiovascular procedures.

In conclusion, CT is the dominant 3D imaging modality that supports the clinical decision-making at the various stages of therapeutic management of cardiovascular diseases from early risk determination to diagnosis and surgical planning.

Acknowledgements

As many of you know that this journey took longer than it was supposed to take. It demanded commitment from both me and my (co-) promoters Prof. Matthijs Oudkerk and Dr. ir. P.M.A. (Peter) van Ooijen. In this regard, I would like to start with expressing my gratitude to them for showing that commitment and encouraging me to see it through. I would also like to show my gratitude to Prof. Rozemarijn Vliegenthart. Her critical thinking and vast knowledge shaped me and helped me to become the clinical professional that I currently am. She was like a third supervisor to me. Of course, none of this would happen without the support of my family. I will always be grateful to my beloved wife Bookie (Pruesamon Gamoltip), my parents, and my second family in Purmerend.

A healthy working environment is very important for finding energy in what you are doing. I would like to thank “mother goose” Dr. E.J.K. (Stella) Noach for creating such an environment. Her efforts brought the whole team together. In my own office that friendship was even closer. I would like to thank my beloved office mates Wisnumurti Kristantanto, Hildebrand Dijkstra, Astri Handayani, Karolien Jaspers, and Jaap Groen for being more than a colleague. The same goes to Gertjan Pelgrim, Kadek Yota Aryanto, Panji Triadyaksa, Marjolein Heuvelmans, and Wiard Jorritsma. Thank you for sharing your knowledge and wonderful ideas. It was such a privilege to work with you. I will never forget our refreshing and energizing special lunch time talks. I would also like to thank Geoffrey Olotu, Rutger van der Schoot, Jalte Norder, Thomas Wilken, and their wonderful supervisor Jan Zijlstra for their efforts in developing the heart pump. Alicja Daszczuk is another brilliant student that I feel privileged to work with. Thank you Alicja for your great ideas and diligent work.

The work life balance is a must especially for long marathons like PhD. Groningen is a wonderful city, but I was feeling like a tourist rather than a resident for quite some time. I knew I need my social circle in Groningen to call it home. I built it slowly but surely starting with Jalmari Saliminen. He was the first person in Groningen that I could call friend. Thanks, Jalle for all unforgettable memories we had together. This circle slowly grew first with Kanat Camlibel and Idil Kokal. I really enjoyed their companionship. Their friendship was beginning of a whole new chapter as it led to meet lifetime best friends that I currently have.

The very first one of them is Devrim Kaba who is one of kindest person I have ever met. Sedat Cengiz joined shortly after. His outgoing and joyful personality added lots of color to my life. Finally, thanks to

Devrim and Sedat I could call Groningen “home”. People who know me also know that I really like to learn new languages and I thought I should at least understand some Dutch. With that purpose I started to take Dutch courses at the Language Center of the University of Groningen. That decision made a far greater impact on my life than I could ever imagine. There, I met Alberto D’Avino and later via Alberto I met Amir Goudarzi. My lifelong friends. Even though he is living in Belgium I am still in touch with Amir thanks to his great thoughtfulness. Meeting Alberto led me to meet Irene Taroni who was at that time mentor of my future wife Bookie. That was certainly a life changing decision. I would like to take this opportunity and thank to my wife Bookie being always there for me in my darkest hours You always give the strength and power to overcome all the obstacles. Everything seems possible with you. Thank you very much “honey”. I should also thank Joe Codamo for making Friday nights so special. That brought us to 2011, the year that I met with one of my best friends Ercan Kokden. It all started with selling a TV. After that moment we found each other more than a friend. Turhan Gul joined us a little bit later. Ercan Kokden, Turhan Gul, and Devrim Kaba are more like a brother to me. They were by my side in all good and bad days and I know they will always be. That circle is completed with Filiz & Cagatay Aygar and Yagiz Unver. Every one of them touched my life in their own ways. Thank you very much to you all to be the family that I have in my second home Groningen and beyond. As speaking life beyond Groningen, I would like to thank Chris van Groeningen and Tom Kokhuis for their support in the final meters of this marathon. Finally, I would like to thank second time Turhan Gul and Hildebrand Dijkstra for being my *paranimfen*.

Sevgili Aileme,

Eger bugun burada bu tezi yaziyorsam bunda en buyuk emegi olan iki insan anennem ve babamdir. Sizlere maddi ve manevi daima arkamda oldugunuz icin ne kadar tesekkur etsem azdir. Sizin desteginiz olmadan su an oldugum konumda bulunmam inanin mumkun degildi. Iyi ki ikiniz de varsiniz. Ardindan tabii ki ikinci ailem geliyor. Ayse, Bahtiyar, Erkan ve Taner Dulkadir. Sizler benim Hollanda‘da ki ailem oldunuz. Zora dustugum her anda yanimda oldunuz. Bana ailemin eksikligini hic hisstermediniz. Sizlerin benim gozumde kendi ailemden hic farkiniz yok. Size de cok cok tesekkur ederim. Kardesim Caner, kuzenlerim Oktay ve Elif e de beni yalniz birakmadiklari ve daima yanimda olduklari icin cok cok tesekkur ediyorum.

Volkan Tuncay

10 July 2020, Best

List of Publications

1. **Introduction to Quantification of Cardiovascular Computed Tomography**
   Based on: *van Ooijen PMA, de Jonge GJ, Kristanto W, Handayani A, Tuncay V, Oudkerk M.* Optimal postprocessing of images following cardiac examination using CT and MRI.
   Imaging in Medicine 2010;2(4):459-474.
2. 3D printing for heart valve disease: a systematic review
   Tuncay V, van Ooijen MA.
   European Radiology Experimental 2019;3:9
3. Design, Implementation and Validation of a Pulsatile Heart Phantom Pump.
   Tuncay V, Zijlstra J, van Ooijen PMA
   Journal of Digital Imaging (Accepted for publication)
   AND
   Heart phantom for the flow measurement through heart valves
   Tuncay V
   ECR 2013, http://dx.doi.org/10.1594/ecr2013/C-2196
4. Non-invasive assessment of coronary artery geometry using coronary CTA
   Tuncay V, Vliegenthart R, den Dekker MAM, de Jonge GJ, van Zandwijk JK,van der Harst P, Oudkerk M, van Ooijen PMA.
   Journal of Cardiovascular Computed Tomography 2018;12(3):257-260.
5. Geometric Differences of the Coronary Arteries during the Cardiac Cycle.
   van Zandwijk JK, Tuncay V, Slump CH, Oudkerk M, Vliegenthart R, van Ooijen PMA.
   Journal of Digital Imaging 2019 (Online ahead of print)
6. Correction of lumen contrast-enhancement influence on non-calcified coronary atherosclerotic plaque quantification on CT
   Kristanto W, Tuncay V, Vliegenthart R, Oudkerk M, van Ooijen PMA.
   Int J Cardiovascular Imaging 2015;31:429-436.
7. Semi-Automatic, quantitative, measurement of the calcified and non-calcified Aortic Valve Area using CTA: Validation and Comparison with Transthoracic Echocardiography.
   Tuncay V,Prakken N, van Ooijen PM, Budde RP, Leiner T, Oudkerk M.
   BioMed Research International 2015:648283.
   AND
   Semi-Automatic, quantitative, measurement of the calcified and non-calcified Aortic valve area using CTA.
   Tuncay V, van Ooijen P, Oudkerk M.
   International Journal of Computer Assisted Radiology and Surgery 2013(suppl.1);8:S29-S30.
8. Does the Aortic Annulus undergo dynamic conformational changes during the cardiac cycle? A systematic Review

Sucha D, Tuncay V, Prakken NHJ, Leiner T, van Ooijen PMA, Oudkerk M, Budde RPJ.
European Heart Journal Cardiovascular Imaging 2015;16(12):1307-1217.